University of Nevada, Reno

Igneous Geochemistry and Geochronology of the Spruce Mountain District, Elko County, Nevada

A thesis submitted in partial fulfillment of the
requirements for the degree of Master of Science in
Geology

by

Tyler C. Baril

Dr. Tommy Thompson/Thesis Advisor

December, 2013

ProQuest LLC.
789 East Eisenhower Parkway
P.O. Box 1346
Ann Arbor, MI 48106 - 1346

University of Nevada, Reno
Statewide • Worldwide

THE GRADUATE SCHOOL

We recommend that the thesis
prepared under our supervision by

TYLER CHAPMAN BARIL

entitled

Igneous Geochemistry And Geochronology Of The Spruce Mountain District, Elko County, Nevada

be accepted in partial fulfillment of the
requirements for the degree of

MASTER OF SCIENCE

Tommy B. Thompson, Ph.D., Advisor

Christopher D. Henry, Ph.D., Committee Member

Thom Seal, Ph.D., Graduate School Representative

Marsha H. Read, Ph. D., Dean, Graduate School

December, 2013

Abstract

Spruce Mountain is a polymetallic mining district located at the southern end of the Pequop mountains in Elko County, Nevada. Historic production of lead, zinc, silver, copper, and gold came from replacement mantos, veins, and skarns. These deposits are spatially associated with porphyry intrusions located throughout the district. Exploration efforts have since revealed the presence of Carlin-type gold and porphyry molybdenum mineralization.

Geologic mapping, petrography, geochemical analysis, and radiometric dating were used to describe each of the igneous intrusions within the district. Subduction-related magmatism occurred in three pulses during the late-Jurassic and mid-Eocene. Jurassic magmatism is represented by two intrusions of medium-grained rhyolite and dacite porphyry emplaced at 155 and 156 Ma, respectively. The more voluminous Eocene magmatism comprises five units of dikes and stocks of porphyritic rhyolite, granite, and aplite. Eocene intrusions were emplaced at 37.5 and 39.1 Ma. Fine to medium-grained andesite, trachyandesite, and lamprophyre dikes are also present although their absolute and relative ages remain unknown.

Magmatism within the district is representative of northern Nevada in terms of age, formation, and composition. Jurassic and Eocene intrusions were emplaced during the most active periods of Jurassic and Eocene magmatism in northern Nevada. Both events were subduction-related and produced high K calc-alkaline melts which may have differentiated in one or more large magma chambers underlying the district. Rhyolite and dacite represent 70% of all Jurassic intrusions in northern Nevada while rhyolite represents 60% of the Eocene intrusions in northern Nevada.

Intrusions within the district closely resemble those associated with Carlin-type gold deposits along the Carlin trend and the porphyry molybdenum deposit at Mt. Hope. Similar age, genesis, composition, and alteration suggest the large scale processes responsible for magmatism were related in each of the three locations. Because of these similarities, the Spruce Mountain district is prospective ground for economic deposits of both styles of mineralization.

Acknowledgments

I would like to thank my advisor, Tommy Thompson, for his guidance in completing this thesis as well as his time and efforts spent teaching me the science of economic geology. Thank you to Chris Henry and Thom Seal for serving on my committee and their many invaluable suggestions on how to improve this manuscript. Thank you to the staff of Renaissance Gold who made this project possible and supported me along the way. Thank you to Julie Hill for all of her assistance over the past few years navigating the treacherous waters of university bureaucracy. Finally I would like to thank each of the many sponsors of the CREG program whose support made my education possible.

Table of Contents

List of Figures

List of Tables

Introduction

The Spruce Mountain district is located at the southern end of the Pequop Mountain range in Elko County, Nevada 63 km south of Wells and 145 km north of Ely (Fig. 1). It covers an area of ~26 km^2 and comprises at least 24 mines and prospects with periodic production between 1869 and 1952. Mining operations began in 1869 when lead and silver ores were discovered at the Kille prospect just north of the North Spruce Mountain peak. Lead, zinc, and silver were mined from limestone-hosted manto and vein deposits. Copper and gold were mined from skarns adjacent to porphyry intrusions. The most productive years were 1924-1927 and 1944-1948, which accounted for just under half of the district's output. From 1869 to 1949 104,519 tons of ore were mined, which produced 23,808,523 lbs. Pb, 3,148,490 lbs. Zn, 1,259,465 oz. Ag, 794,919 lbs. Cu, and 1107 oz. Au, valued at $2,980,605 (Granger, 1957).

Since 1952 there has been no production at Spruce Mountain, but the area has been explored by a number of companies for both precious and base metals. From 1958 through 1982 the district was explored for porphyry Cu-Mo mineralization as well as Pb-Zn-Ag mantos. From 1984 to the present the district has been intermittently explored for sedimentary rock-hosted gold mineralization.

The most recent exploration efforts are a result of the discovery of the 2.2 Moz. Long Canyon deposit located 55 km to the northeast (Smith et al., 2013). Unlike most Carlin-type gold deposits in Nevada, which are hosted in Devonian continental slope and shelf edge sedimentary rocks, Long Canyon is hosted in platform carbonates of Cambrian to Ordovician age (Bedell et al., 2010; Smith et al., 2013). Prior to this discovery the area was considered unprospective due to the idea that massive platform carbonates were too

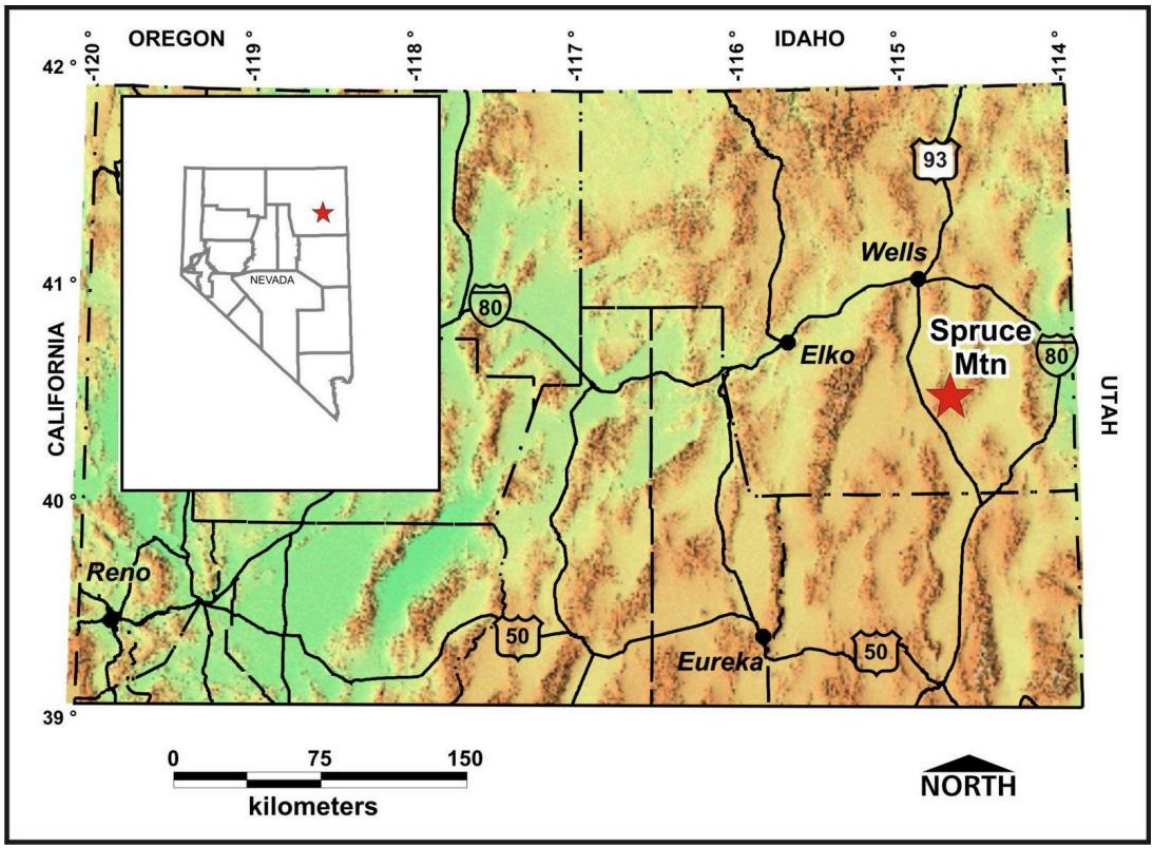

Figure 1. Location of the Spruce Mountain District from Wolverson (2010).

unreactive to host bulk-tonnage deposits, and because it was not located along any of the established trends possibly associated with deeply rooted structures (Smith et al., 2013). Because the Spruce Mountain district contains the same stratigraphy that hosts the Long Canyon deposit, it must also be considered prospective ground for Carlin-type gold mineralization.

Since the period of production at the Spruce Mountain district, new exploration methods have been developed to locate concealed orebodies. Conceptual exploration strategies using favorable geologic settings and indirect detection methods are now critical for successful target generation. Geochemical analysis and radiometric dating of

igneous rocks are two examples of techniques that can be used to help identify prospective ground.

Geochemical analysis of igneous rocks cannot differentiate between those that are associated with mineral deposits and those that are not (Seedorf et al., 2005; duBray, 2007). However, certain deposit types are associated with igneous rocks of a particular geochemical nature. Stockwork molybdenum deposits can be classified based on magma series chemistry ranging from calc-alkaline to alkalic type deposits (Westra and Keith, 1981). Each type of deposit is genetically associated with igneous rocks with a unique set of geochemical features that can be used to identify those that potentially host or are associated with molybdenite mineralization.

Likewise, advances in metallogeny have revealed relationships between mineral deposits, geologic setting, and age. These relationships can be applied in mineral exploration as a guide to locating deposits that are commonly associated with rocks of a particular geologic environment and/or age. For example, the formation of Carlin-type gold deposits along the Carlin trend was contemporaneous with Eocene magmatism (Ressel and Henry, 2006). Given the limited age range of known Carlin-type deposits and their spatial association with Eocene igneous rocks, locating intrusions emplaced between 36 and 42 Ma could lead to the discovery of new Carlin-type gold deposits in the region.

The goal of this study is to determine the nature and timing of the intrusions within the Spruce Mountain district utilizing geologic mapping, petrographic investigation, whole-rock geochemistry, and radiometric dating. Such data for this

district have never been published. These data can also be used to evaluate the potential of the district to host porphyry molybdenum and Carlin-type gold mineralization.

Previous work has largely focused on summarizing mining and exploration activity (Hill, 1916; Schrader, 1931; Granger, 1957; Smith, 1976; LaPointe, 1991). The stratigraphy and structure of the district was described by Harlow (1956), and the Spruce Mountain quadrangle was mapped by Hope (1972).

Methodology

Surface geology was mapped between the months of June and August 2011 at a scale of 1:7874 covering an area of ~8 km^2. Because of the poorly preserved nature of many of the igneous intrusions, igneous rock boundaries were constrained by float concentration. Areas with >50 percent igneous float were considered as part of an intrusion. Rock samples were collected from each of the igneous units for petrographic investigation, whole-rock geochemical analysis, and isotopic dating. Samples were selected from the freshest material to minimize effects of hydrothermal alteration and weathering, although such effects were unavoidable in some locations.

Thin sections from 25 samples were prepared by Spectrum Petrographics for transmitted and reflected light petrography. Mineralogy, texture, and alteration were described to define lithology and discern igneous units. Accompanying billets were stained with sodium cobaltinitrite to identify any potassic alteration.

Eleven intrusive rock samples were analyzed for major and trace element geochemistry at ALS Chemex in Reno, NV. Samples were processed by lithium borate fusion, four acid digestion, and aqua regia digestion before analysis by ICP-MS. Rock geochemistry was used to help identify the igneous units and to determine petrogenesis.

Six intrusions were dated by Dr. Jim Crowley at the Isotope Geology Laboratory at Boise State University using LA-ICP-MS for U-Pb ages of zircons. One sample of molybdenite was sent to the University of Arizona for ^{187}Re-^{187}Os dating to determine the age of mineralization. Techniques and data for U-Pb and Re-Os analyses are listed in Appendix B.

Regional Geology

The Spruce Mountain district is located in southern Elko County, Nevada within the Great Basin physiographic province. This region is characterized by north- to northeast-trending fault-block ranges composed of Paleozoic sedimentary rocks separated by wide, flat valleys. These sedimentary rocks were deposited in a 10-12 km thick package along the passive continental margin of North America (Speed et al., 1988; Camilleri and Chamberlain, 1997). The district is found at the southern end of the Pequop Mountains in the hinterland of the Sevier orogenic belt. This region records nearly continuous sedimentation from Cambrian through Triassic time of predominantly shelf carbonates with local siliciclastic input.

An unconformity between Triassic and Tertiary strata marks crustal deformation related to the Sevier orogeny. At least two episodes of southeast-directed thrust faulting occurred during this period. Between 154 and 84 Ma ~30 km of thickening and at least 69 km of shortening were accomplished either wholly or in part by the Windermere thrust (Camilleri and Chamberlain, 1997). A second pulse of at least 5 km shortening occurred between 84 and 75 Ma along the Independence thrust. Shortening along the Independence thrust was followed, and partially overlapped, by a regional shift to extension from 84 to 19 Ma initially as a response to thickened crust and later due to

basin and range style rifting. Tertiary volcaniclastic and lakebed sedimentary rocks unconformably overlie Paleozoic to Triassic rocks (Camilleri and Chamberlain, 1997).

Igneous intrusions in northern Nevada were emplaced during three periods (1) mid to late Jurassic, (2) early to late Cretaceous, and (3) mid Eocene to mid Miocene (duBray, 2007). Jurassic intrusions account for 26 percent of the intrusions in northern Nevada, and formed in a backarc environment as a result of asthenospheric upwelling after the breakoff and foundering of the subducted Mezcalera plate (Dickinson, 2006). Jurassic magmatism ceased upon the arrival of the leading edge of the Farallon plate beneath Nevada (duBray, 2007). Most intrusions were emplaced between 160 and 155 Ma and are distributed across all of northern Nevada. Compositionally, Jurassic intrusions range from granite to gabbro, but the vast majority are granite and granodiorite and their shallow intrusive equivalents rhyolite and dacite (du Bray, 2007).

The second magmatic pulse occurred during the Cretaceous period and accounts for 42 percent of northern Nevada intrusions. Cretaceous intrusions were emplaced during a period of flat subduction and rapid plate convergence along western North America (Coney and Reynolds, 1977). Most formed between 95 and 90 Ma and are distributed across northern Nevada although magmatism decreased in intensity from west to east. At the end of the Cretaceous plate convergence slowed and slab rollback caused a westward retreat of subduction related magmatism and a cessation of magmatic activity in Nevada (du Bray, 2007). Cretaceous intrusions range in composition from granite to diorite, but are most commonly granite and granodiorite (du Bray, 2007).

The third pulse of magmatic activity in northern Nevada was active between 42 and 14 Ma and was responsible for 32 percent of its intrusions. From 40 to 20 Ma

roughly east-west belts of magmatism swept southward through northern Nevada as a result of asymmetric foundering and tearing of the subducting Farallon slab (Humphreys, 1995). Subduction-related magmatism subsequently waned in northern Nevada ending with a handful of Miocene intrusions as arc magmatism migrated westward. Between 17 and 14 Ma a northwest trending magmatic belt formed in north-central Nevada associated with the initiation of backarc continental rifting (Zoback et al., 1994). Mid-Eocene to mid-Miocene intrusions mimic the compositional distribution of the previous two magmatic pulses with primarily granite and granodiorite and their fine-grained equivalents. This period contains significantly higher percentages of rhyolite and dacite, possibly due to a lack of preservation of shallowly emplaced intrusions of Jurassic and Cretaceous ages (du Bray, 2007).

Geochemically, these three groups of intrusions are nearly identical (du Bray, 2007). The majority are high K calc-alkalic with major oxide and trace element concentrations that completely overlap one another. Such similarity between age groups suggests petrogenetic processes were similar from the Jurassic to the Eocene (duBray, 2007). Lead and strontium isotopic data for northern Nevada intrusions suggest a genesis involving mantle derived magma mixed with varying amounts of continental crust (Tosdal et al., 2000). Only the most evolved intrusions show evidence that fractional crystallization was the primary geochemical control (du Bray, 2007).

District Geology

Stratigraphy

The sedimentary sequence within the Spruce Mountain district consists of mid- to late- Paleozoic carbonates and siliciclastics (Fig. 4). The oldest rocks exposed are a 300

m thick sequence of dolomites composed of light gray, sugary, brecciated dolomite interbedded with light gray, very fine-grained dolomite and dark gray, very fine-grained dolomite with minor shale. The basal 60 m contains 1-5 mm black chert nodules and brachiopod fossils (Hope, 1972). This unit displays characteristics similar to both the Ordovician Fish Haven and Silurian Laketown dolomites and likely includes one or both of these formations (Harlow, 1956). Overlying that is the Devonian Simonson dolomite, a medium to dark gray, fine-grained dolomite ~150 m thick. Beds of arenaceous dolomite are located near the base of the section while the upper 60 m exhibits interbedded light and dark gray limestone. At the top of the Devonian sequence lies the Guilmette Formation, a thick bedded to massive medium gray, fine-grained limestone ~500 m thick with local shaly and silty beds.

The late Paleozoic sequence is composed of siliciclastics underlying platform carbonates beginning with the Mississippian Chainman Shale and Diamond Peak Formation. The Chainman Shale lies conformably beneath the Diamond Peak Formation and is well-exposed in only one location 600 m south of Kille Pass along the road up to the north peak of Spruce Mountain. The outcrop contains 15 m of black, silty shale whose total thickness is unknown. The Chainman Shale is overlain by an ~800 m thick sequence of chert and quartzite pebble conglomerates with interbedded gray, fossiliferous limestones near the top. The conglomerates consist of subrounded to subangular fragments of chert 1-6 cm and very minor quartzite clasts averaging 1 cm in diameter. These conglomerates are cemented with quartz sand and silica.

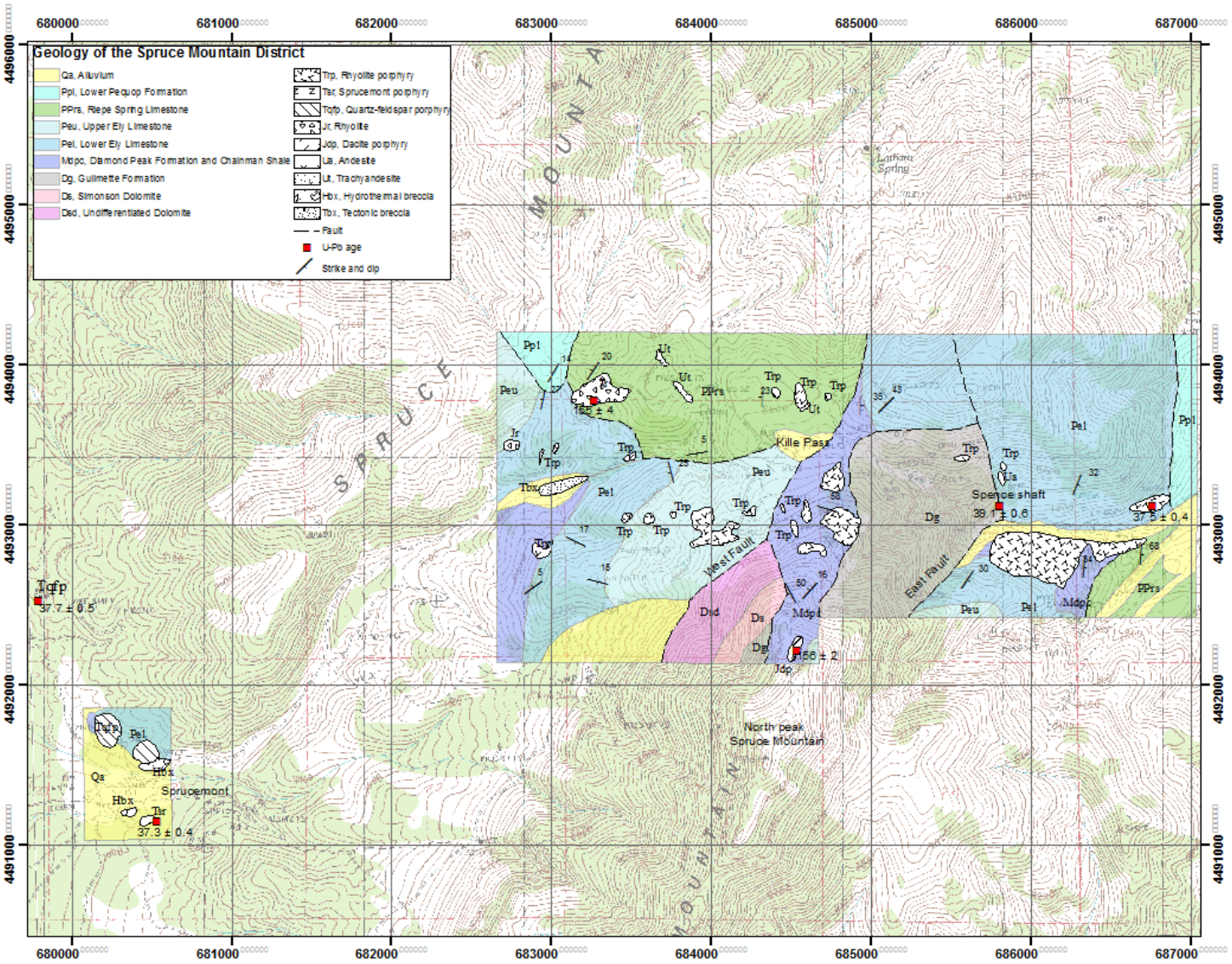

Figure 2. Geologic map of the Spruce Mountain district. Lithology and fault names from Hope (1972).

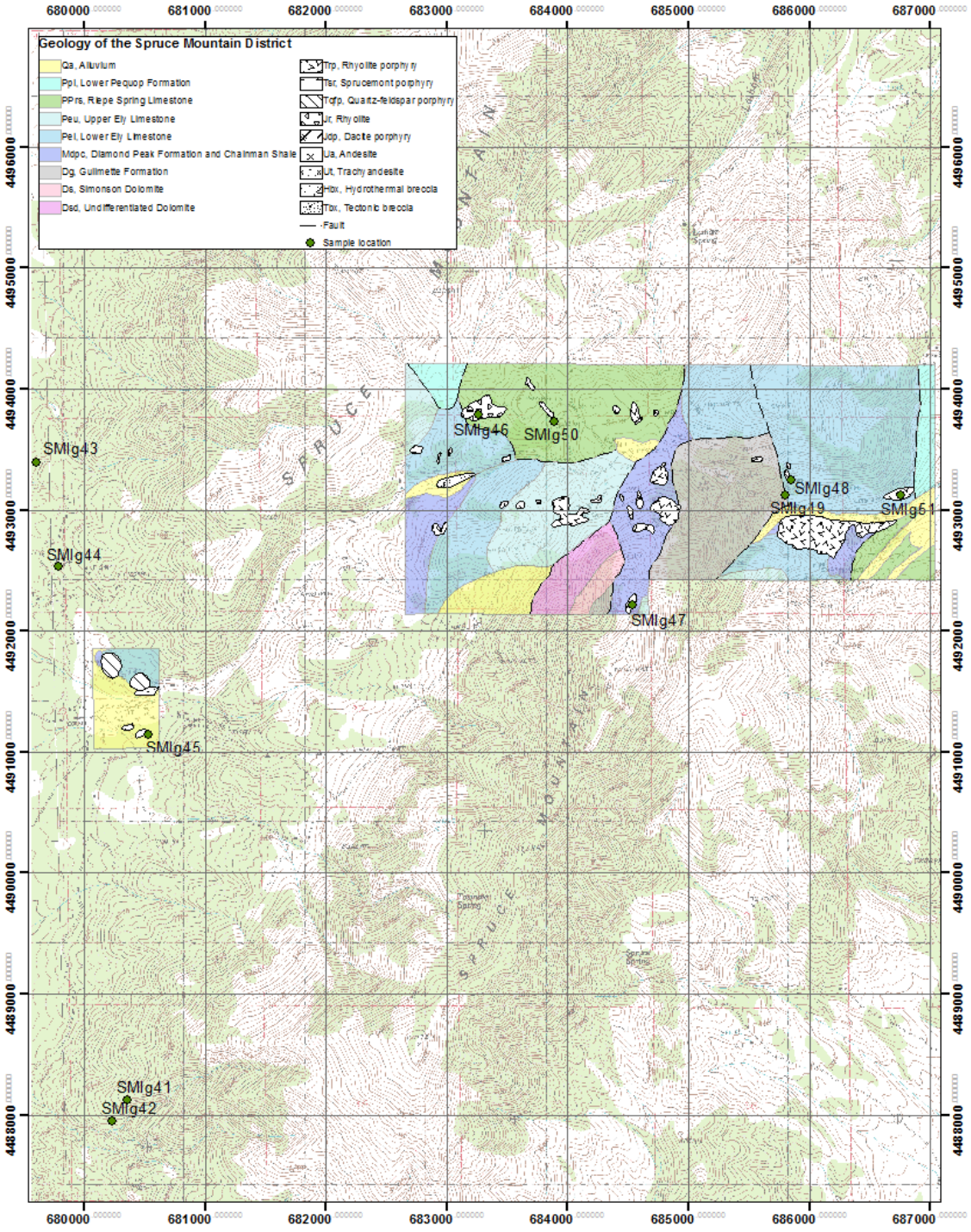

Figure 3. Sample locations for geochemical analysis and radiometric dating.

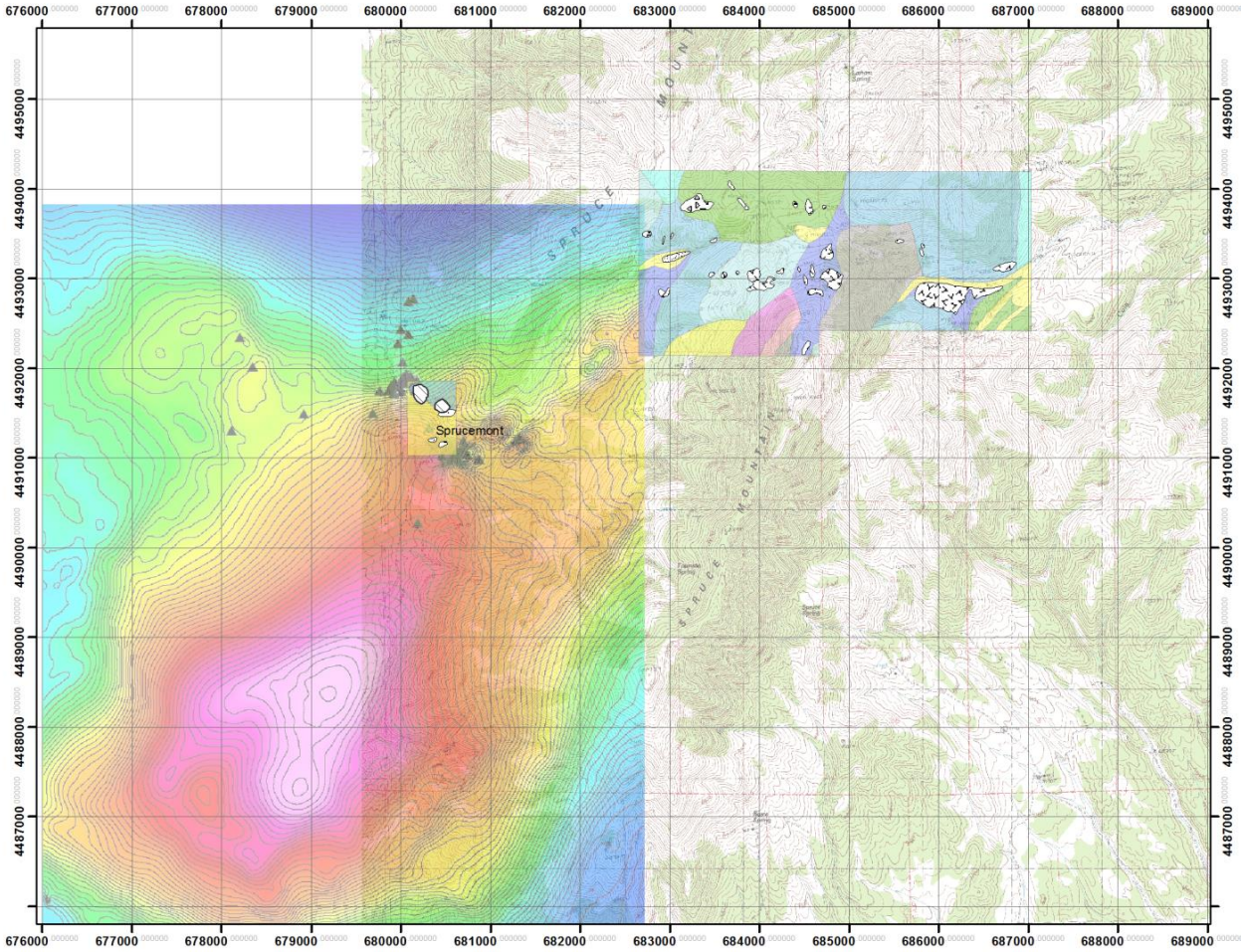

Figure 4. Spruce Mountain geology overlain by aeromagnetic survey data. Results suggest the presence of a northeast trending intrusive body with a maximum depth of 400 to 600 m. A 250 to 300 m deep apophysis located beneath the Sprucemont site could be the source of the porphyry intrusions and silicified breccias. Black triangles represent historic drill collars. White, pink, and red represent areas of high magnetic field strength relative to surrounding rocks (Wolverson, 2010).

Overlying the Mississippian units are a series of thick Pennsylvanian to Permian limestones. The oldest is the Ely Limestone composed of the lower and upper units. The lower Ely is ~300 m thick and characterized by thick bedded to massive fine-grained limestone with minor chert pebble conglomerate and sandy limestone beds at the base. 1-19 cm concentrically laminated chert nodules are common as well as locally abundant 1-3 mm grey chert nodules. Fossils within the limestone beds include brachiopods, crinoids, and coral (Hope, 1972). The upper Ely is an ~600 m thick medium bedded to massive gray limestone with minor interbedded calcareous shale and siltstone. Small chert nodules are common throughout the section as well as brachiopod, crinoid, and coral fossils (Hope, 1972; Harlow, 1956).

Above the Ely lies the Riepe Spring Limestone, a ~450 m thick gray massive to thick-bedded fine-grained limestone with locally abundant bedded chert and minor chert-pebble conglomerate. Arenaceous limestone, calcareous siltstone, and calcareous sandstone are commonly interbedded. Brachiopod and crinoid fossils are abundant (Hope, 1972). The uppermost unit mapped in the district is the lower member of the Permian Pequop Formation, a ~400 m thick medium- to thick-bedded fine-grained limestone with interbedded siltstones. Chert nodules are locally abundant along with crinoids and gastropods (Hope, 1972).

Igneous Rocks

The Paleozoic sedimentary sequence at Spruce Mountain is intruded by a suite of igneous rocks that are generally poorly exposed and highly altered (Table 1). Photomicrographs of each unit are located in Appendix C.

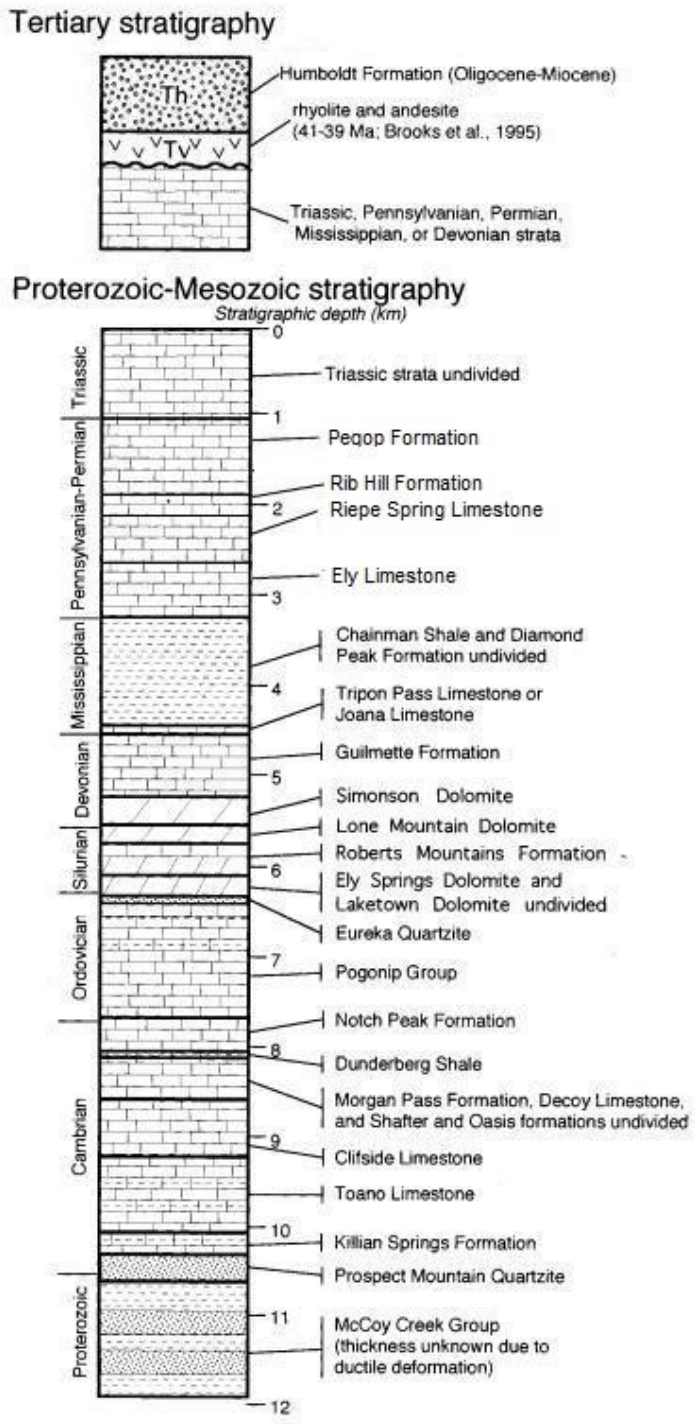

Figure 5. Generalized stratigraphic column of Proterozoic through Tertiary strata in northeast Nevada. Sedimentary rocks exposed in the Spruce Mountain district range from the Ordovician Pogonip Group to the Permian Pequop Formation. Modified from Camilleri and Chamberlain (1997).

Eocene

Sprucemont porphyry (SMIg45) is a rhyolite unit that occurs in a single 100 m by 50 m outcrop on the western edge of the study area. The texture is porphyritic with quartz, potassium feldspar, plagioclase, and biotite phenocrysts set in a fine-grained matrix. This unit is distinguished from quartz-feldspar porphyry by its lighter gray color and significantly larger grain size. Alteration is intense with complete replacement of feldspars to sericite and kaolinite as well as abundant oxidized pyrite.

Rhyolite porphyry (SMIg51) is located on the eastern side of the district as many irregularly shaped outcrops ranging in width from 20 m to 1 km. The east-west band of outcrops stretching from the center to the eastern edge of the district is likely a large dike ~150 m wide with a strike length of ~4 km and has been previously mapped as such (Schrader, 1931). The texture is porphyritic with quartz, plagioclase, and potassium feldspar phenocrysts in a fine-grained matrix. The rock is bright white due to pervasive sericite alteration.

Quartz-feldspar porphyry (SMIg44) is a rhyolite unit located on the western edge of the study area and occurs as two circular outcrops 150 m in diameter and one N-S striking dike 0.5 m wide. The rock is light gray with a porphyritic texture composed of quartz, plagioclase, and potassium feldspar phenocrysts in a fine-grained matrix of the same minerals. The dike displays 1-10 mm wide flow banding oriented parallel to strike. Alteration effects include moderate replacement of feldspars by sericite and minor pyrite. Local parallel quartz veining 2-4 mm wide is present in the two circular outcrops and does not extend to the country rock.

Granite porphyry (SMIg49) is found on the east side of the district in only one location. It does not crop out but is located in a large dump adjacent to an old mine shaft called the Spence shaft. Schrader (1931) reported that the Spence shaft was sunk adjacent to granite porphyry. The rock is light gray with a porphyritic texture composed of potassium feldspar, quartz, plagioclase, and biotite phenocrysts in a fine-grained matrix. Potassic alteration is intense. 1-5 mm parallel and cross-cutting quartz veins are common. White quartz veins are barren while blue-gray quartz veins contain minor molybdenite. Disseminated pyrite and chalcopyrite are also present.

Jurassic

Medium-grained rhyolite (SMIg46) occurs in two outcrops on the north side of the district. The rock is light gray and composed of predominantly plagioclase and potassium feldspar with minor quartz. The texture is equigranular with grain sizes ranging from 1-2 mm. This unit is differentiated based on its equigranular texture and resistance to weathering. Alteration is weak with only minor replacement of feldspars by sericite and calcite.

Dacite porphyry (SMIg47) is found in one location ~600 m north of the Spruce Mountain peak. It occurs as an elongate body of light green resistant rock 200 m long by 100 m wide. The texture is porphyritic with plagioclase and minor quartz phenocrysts set in a fine-grained matrix. Strong propylitic alteration characterizes this rock with near complete alteration of plagioclase and biotite to chlorite and calcite. Plagioclase phenocrysts also display weak sericite and kaolinite alteration.

Table 1. Characteristics of intrusions within the Spruce Mountain district.

Unit	Sample ID	Texture	Mineralogy	Age
Sprucemont porphyry	SMIg45	Porphyritic, 25% phenocrysts	Qtz: 40%, 1-3 mm Kf: 35%, 2-10 mm Pl: 20%, 1-2 mm Bt: 5%, 0.1-0.5 mm	37.3±0.4
Rhyolite porphyry	SMIg51	Porphyritic, 15% phenocrysts	Qtz: 70%, 1-4 mm Kf: 20%, 1-2 mm Pl: 10%, 1-2 mm	37.5±0.4
Quartz-feldspar porphyry	SMIg44	Porphyritic, 7% phenocrysts	Pl: 40%, 1-4 mm Qtz: 30%, 1-3 mm Kf: 20%, 1-2 mm Bt: 10%, 0.1-1 mm	37.7±0.5
Granite porphyry	SMIg49	Porphyritic, 20% phenocrysts	Kf: 50%, 3-9 mm Qtz: 20%, 1-6 mm Pl: 20%, 1-3 mm Bt: 10%, 0.5-2 mm	39.1±0.6
Rhyolite	SMIg46	Medium-grained	Pl: 50%, 1-2 mm Kf: 30%, 1-2 mm Qtz: 20%, 0.5-2 mm	155±4
Dacite porphyry	SMIg47	Porphyritic, 10% phenocrysts	Pl: 60%, 0.5-2 mm Qtz: 20%, 0.5-2 mm Bt: 20%, 0.5-1 mm	156±2
Andesite	SMIg41, SMIg42, SMIg43, SMIg48	Fine to medium-grained	Pl: 35-70%, 0.5-3 mm Hbl: 30-40%, 0.5-2 mm Qtz: 0-20%, 0.5-1 mm Bt: 0-10%, 0.1-0.5 mm	Unknown
Trachyandesite	SMIg50	Medium-grained	Kf: 40%, 1-2 mm Hbl: 40%, 1-3 mm Bt: 10% 0.5-1 mm Qtz: 10%, 0.5-1 mm	Unknown
Aplite (Spadafora, 1979)		Fine-grained to porphyritic	Quartz, feldspar, muscovite	Younger than Rhyolite porphyry
Lamprophyre (Schrader, 1931)		Porphyritic	Abundant biotite and orthoclase, hornblende, olivine, plagioclase	Unknown

Qtz=quartz, Kf=potassium feldspar, Pl=plagioclase, Bt=biotite, Hbl=hornblende.

Undated

Andesite and trachyandesite dikes (SMIg41, 42, 43, 48, 50) are distributed throughout the district. They range in color from light to dark green, are <1 m wide, and are not well exposed at the surface. Textures range from fine to medium-grained. They are composed primarily of plagioclase, potassium feldspar, and hornblende with minor biotite and quartz. Alteration is variable ranging from unaltered (SMIg43, SMIg48) to intensely altered with complete replacement of primary mineralogy (SMIg41, SMIg42). Sericite, calcite, chlorite, and pyrite are the most common alteration products.

Several other intrusions were recognized by previous workers. Schrader (1931) identified a "lamprophyre" dike within the underground workings of the Black Forest mine located 600 m southeast of Kille Pass. The rock is dark green and porphyritic with phenocrysts of biotite, orthoclase, hornblende, olivine, and plagioclase. Biotite is altered to chlorite while much of the hornblende is altered to actinolite. Feldspars are altered to epidote, sericite, and kaolinite. Exploratory drilling by Freeport encountered an aplite intrusion at Kille Pass. This rock is light colored with a texture ranging from sugary (<1 mm) to porphyritic. It is composed of quartz, feldspar, and muscovite (Spadafora, 1979).

Two outcrops of silicified breccia are located on the western margin of the district. Both are reddish brown with 1-2 cm angular clasts of quartz-feldspar porphyry held in a matrix of silica and iron oxides. They are spatially associated with rhyolite intrusions and may represent late stage venting of volatiles (Spadafora, 1979). A recent aeromagnetic survey has revealed a large magnetic anomaly underlying the Sprucemont area (Fig.4). This may be the source pluton for the Eocene intrusions on the west side of the district.

Structure

The predominant structural fabric in the Spruce Mountain district is that of northeast, northwest, and north-south striking normal faults. These low and high angle normal faults reflect the regional shift to extension postdating the Sevier orogeny (Camilleri and Chamberlain, 1997). The most obvious expression of this is the Spruce Mountain ridge, the highest topographic feature in the area. It is a northeast striking horst bounded on the east by the East fault and on the west by the West fault (Hope, 1972). This northeast structural trend localized mineralizing fluids as most historic mines and prospects are spatially associated with high angle northeast-striking faults. 1-2 km west and northwest of Sprucemont west-northwest to northwest striking normal faults dominate, localizing fluids from which jasperoids and disseminated gold mineralization precipitated (Wolverson, 2010).

Also along this northeast trend is a second breccia type located 3 km to the northeast of Sprucemont between the Diamond Peak and Lower Ely contact. Limestone has been fractured into sub-angular clasts with interstitial calcite veining. Hope (1972) indicated a larger extent of this breccia, however upon investigation by the author much of what was mapped as breccia was simply altered limestone. This breccia is likely structural in origin.

Alteration and Mineralization

Most of the igneous rocks in the district have experienced moderate to intense hydrothermal alteration. These effects are strongest in the Eocene rhyolites, which commonly have a bleached appearance due to the replacement of feldspars by sericite

and kaolinite. Quartz-feldspar porphyry has a phyllic alteration assemblage while potassic alteration affected both rhyolite porphyry and granite porphyry.

Jurassic intrusions have not been as highly altered but do show some effects. Dacite porphyry has a greenish appearance due to pervasive alteration of biotite to chlorite and plagioclase to calcite. Jurassic rhyolite shows weak alteration of plagioclase to calcite and sericite. Several of the mafic dikes including SMIg41, SMIg42, and SMIg50 have been highly altered by chlorite, calcite, sericite, and pyrite. SMIg43 and SMIg48 show no alteration effects.

Most intrusions had a minimal metamorphic effect on the country rock. Recrystallized limestone is adjacent to some Eocene rhyolite outcrops, but generally extends for no more than 10 m from the intrusion. One notable exception occurs just east of Sprucemont in which a band of skarn alteration 150 m wide by 1 km long extends toward the northeast (Schrader, 1931).

Several styles of mineralization are present at Spruce Mountain. Carbonate replacement deposits occur throughout the district and were the target of early mining efforts. They occur in multiple forms including stratabound, fissure vein, and skarn deposits, and are located either adjacent to or surrounding rhyolite porphyry intrusions. Stratabound deposits were typically 0.5-1 m thick and extended laterally up to 40 m away from the intrusive-country rock contact within favorable beds. Vein deposits occupied faults and fractures and were typically 2-3 m wide and up to 100 m along strike (Schrader, 1931). Hypogene minerals included argentiferous galena, tetrahedrite, sphalerite, chalcopyrite, pyrite, and bornite. Supergene minerals included cerussite, anglesite, malachite, chrysocolla, and smithsonite (Schrader, 1931). Skarns are less

abundant than other replacement deposits and host copper oxides, gold, and minor scheelite associated with garnet, pyroxene, and fluorite (Schrader, 1931).

Exploration in the late 1970's and early 1980's resulted in the discovery of two centers of low-grade molybdenum mineralization at Sprucemont and Kille Pass (Spadafora, 1979). Molybdenite-bearing quartz veins hosted in rhyolite porphyry and granite porphyry intrusions suggest porphyry molybdenum style mineralization. In the mid 1980's sedimentary rock-hosted gold mineralization was discovered ~1 km northwest of Sprucemont. Jasperoids associated with sedimentary rock-hosted gold suggest the presence of Carlin-type gold mineralization. Most recently, geochemical signatures typical of gold skarn deposits (As, Bi, Te) have been identified (Wolverson, 2010).

Igneous Geochemistry

Whole-rock geochemical analyses are listed in Appendix A. Major oxides and trace elements were normalized to 100 percent on a volatile-free basis. Major elements are presented in Harker diagrams using SiO_2 as the index of differentiation (Fig. 6). As SiO_2 content increases MgO, Fe_2O_3, TiO_2, CaO, and P_2O_5 all decrease. Al_2O_3 and Na_2O increase to ~60 percent SiO_2 after which they decrease. K_2O increases with SiO_2. REE content generally increases with decreasing SiO_2 (Fig. 8). Because of the small sample suite and alteration effects, intrusions that share a common source cannot be identified.

Eocene

Eocene intrusions are all rhyolitic according to TAS and Zr/TiO_2 vs. SiO_2 diagrams (Fig. 7A, B), and contain 74.5 to 79.2 percent SiO_2. Eocene rhyolites plot in either the high K calc-alkalic or shoshonitic series on a K_2O vs. SiO_2 diagram, however

this is likely inaccurate due to alteration (Fig. 7C). Each unit has undergone argillic, silicic, or potassic alteration. Samples from the western side of the district including SMIg44 and SMIg45 contain >79 percent SiO_2 and <0.2 percent Na_2O indicating silicic and argillic alteration. Samples SMIg49 and SMIg51 on the eastern side of the district have been potassically altered with K_2O values of 6.5 and 8.8 percent and Na_2O values of 2.2 and 0.4 percent, respectively. Rare earth element (REE) concentrations are the lowest of the three age groups, display concave up slopes with higher concentrations of LREE, and show negative Eu anomalies. SMIg51 is unique in that it contains very low LREE (Fig. 8). Negative Eu anomalies indicate the melts that formed these intrusions differentiated from parental magmas.

Jurassic

Jurassic intrusions are classified as rhyolite (SMIg46) and dacite porphyry (SMIg47), and contain 75.7 and 67.2 percent SiO_2, respectively. Alteration effects are minimal with only moderate Na_2O loss in the rhyolite. Like the other age groups Jurassic intrusions are enriched in LREE relative to HREE, however they do not display negative Eu anomalies and LREE content is significantly higher than Eocene intrusions.

Undated mafic dikes

Unlike Eocene and Jurassic intrusions, the mafic dikes at Spruce Mountain are inconsistently classified between TAS and Zr/TiO_2 vs. SiO_2 diagrams. The latter is used to name these dikes as it is intended for use with altered rocks. SiO_2 content of andesite and trachyandesite dikes ranges from 52.8 to 57.2 percent. Alteration is variable in intensity and occurs as chlorite and calcite replacement of primary amphibole and plagioclase. MgO is elevated in all samples ranging from 6.4 to 8.4 percent. K_2O is

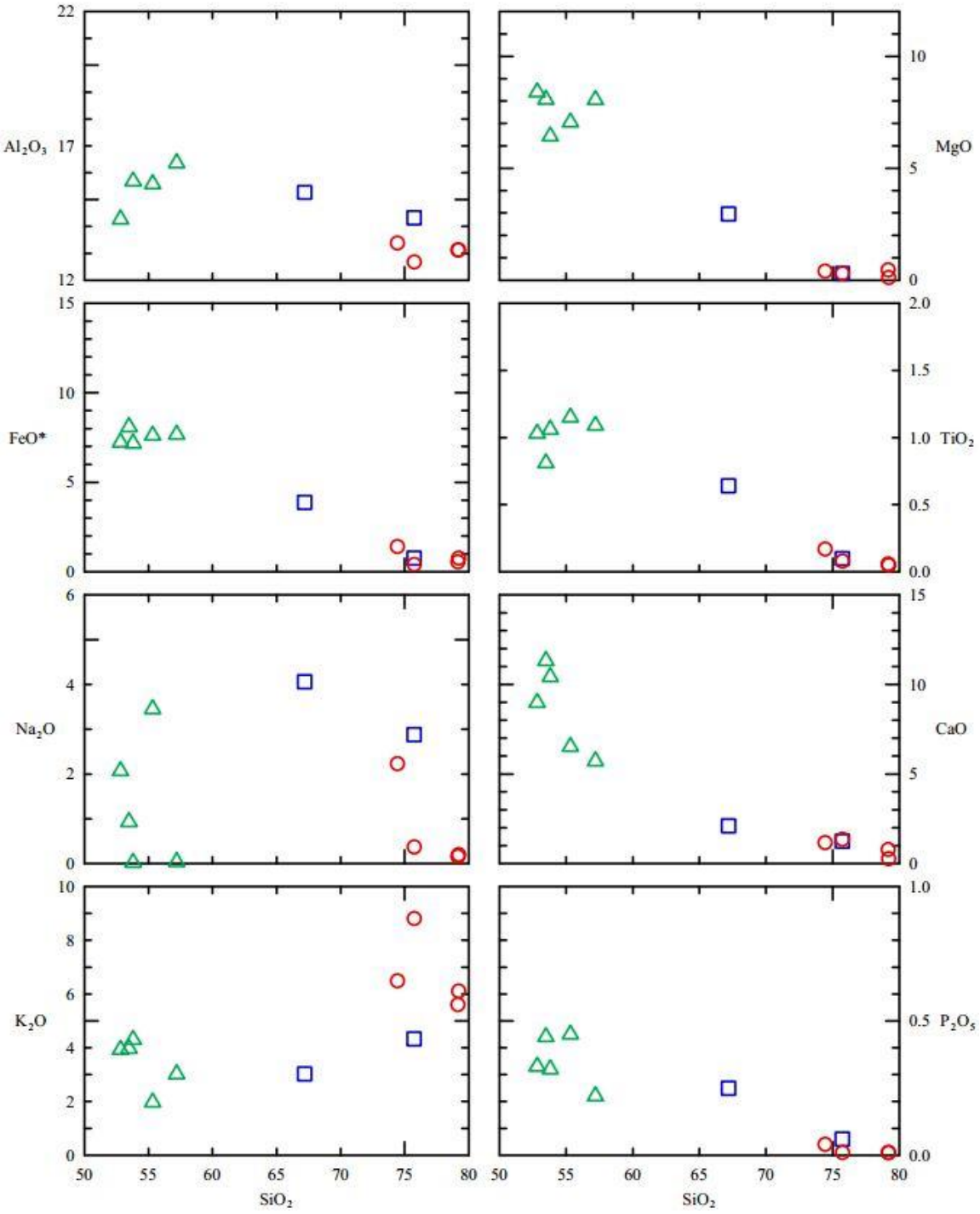

Figure 6. Harker variation diagrams for Spruce Mountain igneous rocks. Red circles – Eocene, blue squares – Jurassic, green triangles – undated.

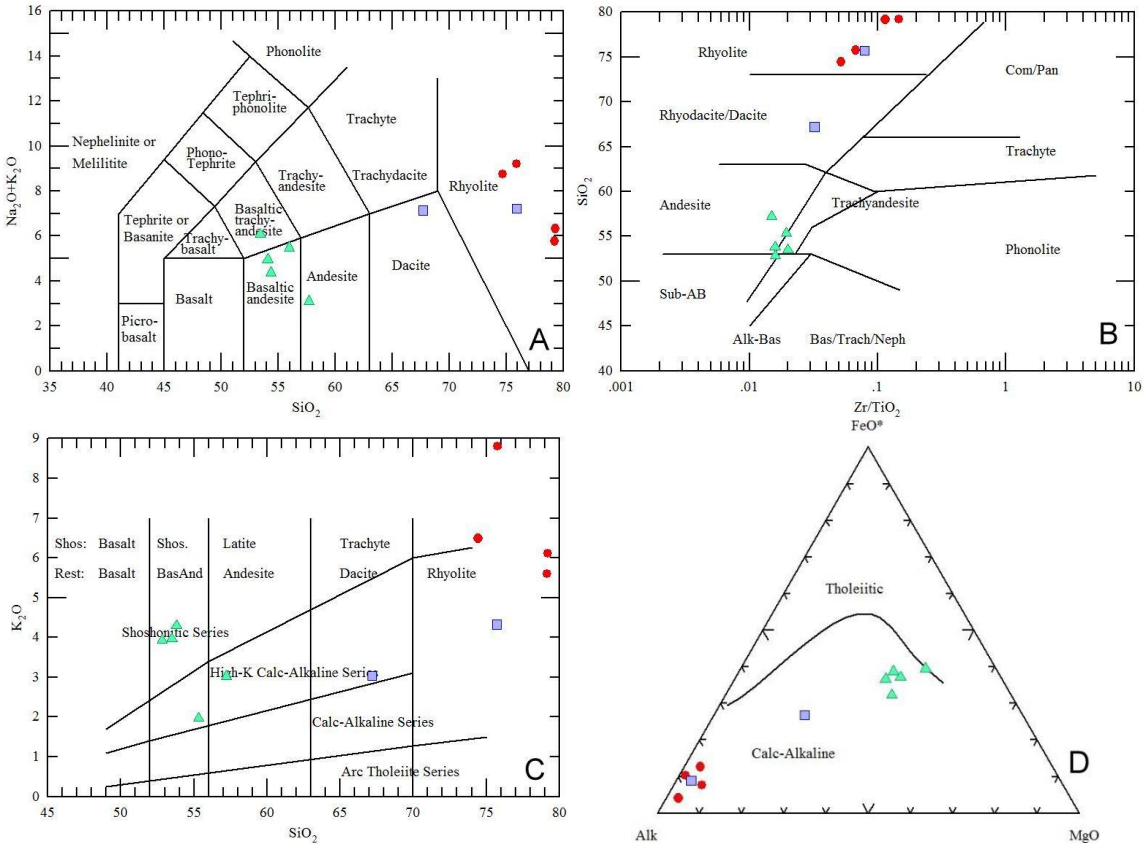

Figure 7. Classification and discrimination diagrams. A. TAS diagram (LeBas et al., 1986). High K_2O values in many of the intrusions hide significant loss of Na_2O. B. Immobile element discrimination diagram (Winchester and Floyd, 1977). C. K_2O vs. SiO_2 from Peccerillo and Taylor (1976). Several rhyolites and mafic dikes plot within the shoshonitic series likely because of hydrothermal alteration. D. AFM diagram from Irvine and Baragar (1971) showing the calc-alkaline nature of the intrusions. This suggests magmatism was subduction related.

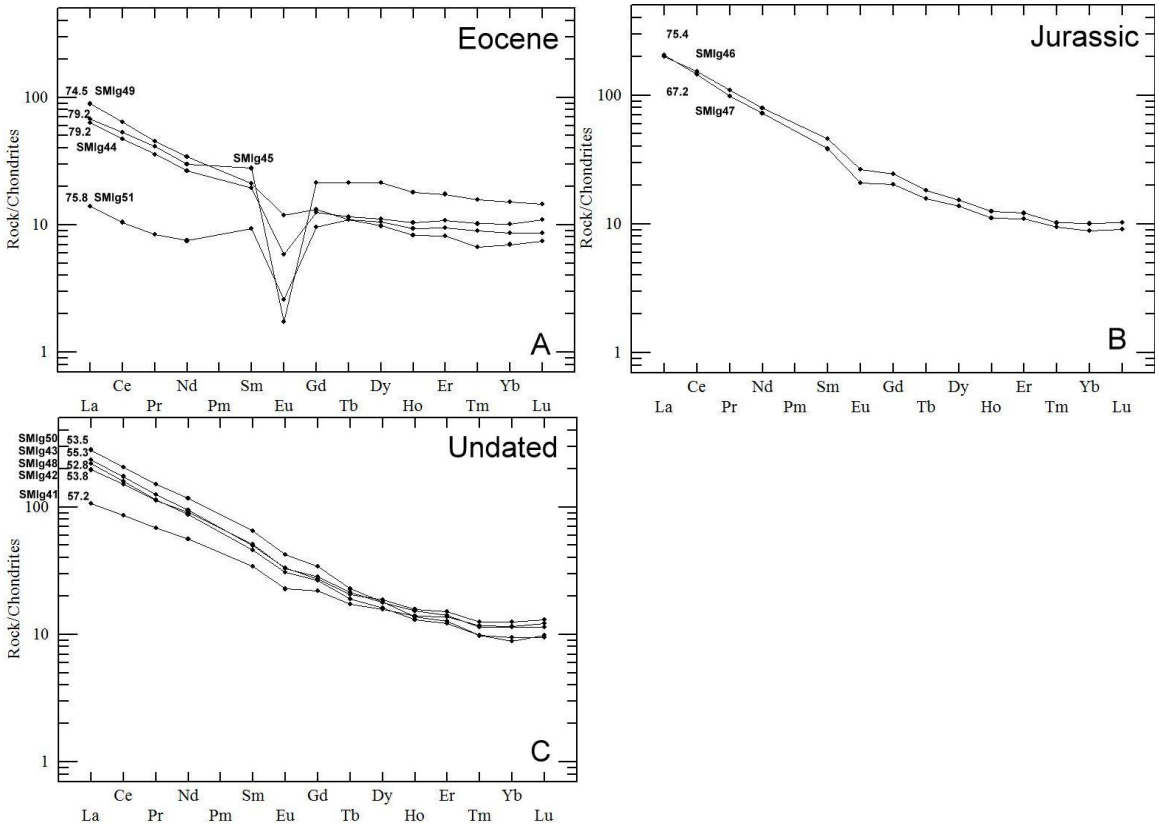

Figure 8. Chondrite-normalized REE diagrams for intrusions of each age group (normalization values from Sun and McDonough, 1989). Number labels are SiO_2 content. A. Pronounced negative Eu anomalies in Eocene rocks are a result of Eu^{2+} substitution for Ca^{2+} in plagioclase that is subsequently separated from the melt.

elevated in four of the five dikes with values >3.0 percent. REE patterns are similar to those of Jurassic rocks with steep slopes and small Eu anomalies, although the dikes show a greater range in LREE content. Differences in REE concentrations between the dikes are insignificant with only SMIg41 having a slightly lower concentration of LREE than the rest.

Igneous Geochronology

Absolute ages of igneous rocks within the district have never been published, and only a few relative ages have been determined through drilling. Rhyolite porphyry cuts granite porphyry and aplite cuts rhyolite porphyry (Spadafora, 1979). Field relationships were not visible for any of the mafic dikes. Data and methodology for U-Pb and Re-Os dating are located in Appendices B and C.

U-Pb

U-Pb dating of zircons was used to determine the crystallization ages of the igneous rocks at Spruce Mountain. Of the eleven igneous bodies sampled only six had an adequate concentration of zircons for analysis. None of the mafic dikes were able to be dated. Results show three pulses of magmatism during the late Jurassic and mid-Eocene epochs (Table 2). Dacite porphyry and rhyolite crystallized at 156 ± 2 Ma and 155 ± 4 Ma, respectively. Granite porphyry is the oldest of the Eocene rocks with a crystallization age of 39.1 ± 0.6 Ma. Rhyolite porphyry, Quartz-feldspar porphyry, and Sprucemont porphyry were all emplaced around the same time at 37.5 ± 0.4, 37.7 ± 0.5, and 37.3 ± 0.4 Ma, respectively.

Table 2. Radiometric dates of Spruce Mountain intrusions.

Sample ID	Location (NAD27)	Description	Dating Method	Age	±2σ
SMIg44	679937, 4492126	Quartz-feldspar porphyry dike	U-Pb	37.7	0.5
SMIg45	680682, 4490741	Sprucemont porphyry	U-Pb	37.3	0.4
SMIg46	683420, 4493380	Rhyolite	U-Pb	155	4
SMIg47	684690, 4491810	Dacite porphyry	U-Pb	156	2
SMIg49	685957, 4492716	Granite porphyry	U-Pb	39.1	0.6
SMIg51	686910, 4492715	Rhyolite porphyry	U-Pb	37.5	0.4
SMIg49	685957, 4492716	Molybdenite in granite porphyry	^{187}Re-^{187}Os	41.34	0.21
SMIg49[1]	685957, 4492716	Biotite in granite porphyry	^{40}Ar-^{39}Ar	38.60	0.13

[1]Unpublished data from Henry, C.D. (2012).

Re-Os

^{187}Re-^{187}Os dating of molybdenite was used to determine the age of hydrothermal activity and sulfide mineralization associated with granite porphyry. Results indicate an age of mineralization of 41.34 ± 0.21 Ma. This date is problematic as it predates the host granite. A possible explanation is the alteration of molybdenite to powellite or ferrimolybdite, which causes loss of rhenium.

Discussion

Formation of igneous rocks in the Spruce Mountain district

Geochronological and geochemical analyses of igneous rocks within the Spruce Mountain district show a development consistent with intrusions throughout northern

Nevada. U-Pb dates indicate three episodes of magmatism at 151-159 Ma, 39.1 Ma, and 37.5 Ma. This combination of Jurassic and Eocene magmatism is present in many other locations including the Ruby, Cortez, Tuscarora, Independence, Piñon, Pilot, and Snake mountain ranges. Jurassic intrusions at Spruce Mountain were emplaced during the most active period of Jurassic magmatism in Nevada, from 155 to 160 Ma (duBray, 2007). Similarly, Eocene intrusions at Spruce Mountain were emplaced during the most active period of Eocene magmatism, 35 to 40 Ma (duBray, 2007). One unique feature of the Spruce Mountain district is the lack of Cretaceous magmatism. Only three other locations in Nevada have only Jurassic and Eocene intrusions – the Cortez, Piñon, and Pilot ranges.

Geochemically, intrusions at Spruce Mountain are consistent with the rest of northern Nevada. Rhyolites, which represent 38 percent of northern Nevada intrusions, are the dominant composition within the district. Dacite, andesite, lamprophyre, and aplite are all represented elsewhere in northern Nevada. AFM and K_2O vs. SiO_2 diagrams indicate that Spruce Mountain intrusions are calc-alkaline and fall within the high K to shoshonite series, although the Eocene rhyolites are likely inaccurately classified due to alteration (Fig. 9A-D). Northern Nevada intrusions are also calc-alkaline and most plot within the high K field. Tectonic setting discrimination diagrams support the subduction related formation of Spruce Mountain intrusions (Fig. 9E). Eocene and Jurassic intrusions plot within the volcanic arc field of a Rb vs. Y+Nb diagram with only one exception, SMIg45, which plots in the syn-collision field because of high Rb (495 ppm), Nb (48.5 ppm), and Y (31.8 ppm). This is likely due to alteration as Rb and Nb are both mobile in hydrothermal fluids associated with porphyry

molybdenum mineralization (Hildreth, 1979; Westra and Keith, 1981, White et al., 1981). Most northern Nevada intrusions plot within the volcanic arc field, although a significant population of Eocene intrusions plot in the within-plate field. Despite the overlapping U-Pb ages of both the Jurassic and Eocene intrusions, there is insufficient data to conclude whether or not intrusions from each age group share a common source. A larger dataset would provide a greater understanding of petrogenesis.

Comparison with the igneous rocks of the Mt. Hope porphyry Mo deposit

Much of the information in this section regarding the history and geology of the Mt. Hope deposit is summarized from Westra and Riedell (1996). Mt. Hope is a transitional Climax-type deposit located 35 km northwest of Eureka, Nevada. Like Spruce Mountain, Mt. Hope has historic production dating back to 1870 when Pb-Zn replacement ores were discovered in altered limestones. Between 1870 and 1965 $1,335,393 of zinc, lead, silver, copper, and gold were produced. In 1978 Exxon Minerals investigated the area and recognized a large alteration zone within a rhyolitic igneous complex. Rock chip and soil sampling showed anomalous Mo, F, and Cu in a central zone surrounded by anomalous Pb, Zn, and Ag. IP surveys indicated the presence of sulfides at depth, and an airborne radiometric survey identified the gamma ray signature of potassic alteration. Drilling commenced shortly after and a resource of 562 t

Figure 9. A-B. K_2O vs. SiO_2 diagrams for Eocene (red) and Jurassic (blue) intrusions at Spruce Mountain compared with unaltered Eocene and Jurassic intrusions (black) from northern Nevada. C-D. AFM diagrams comparing Eocene and Jurassic intrusions with unaltered Eocene and Jurassic intrusions from northern Nevada. E. Tectonic setting discrimination diagram from Pearce et al. (1984) comparing Eocene and Jurassic intrusions from Spruce Mountain and unaltered Eocene and Jurassic intrusions from northern Nevada.

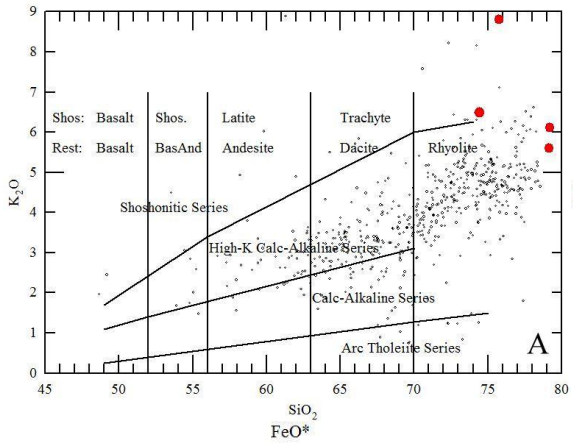
Shos: Basalt
Rest: Basalt
Shos. BasAnd
Latite Andesite
Trachyte Dacite
Rhyolite
Shoshonitic Series
High-K Calc-Alkaline Series
Calc-Alkaline Series
Arc Tholeiite Series
A
K2O
SiO2

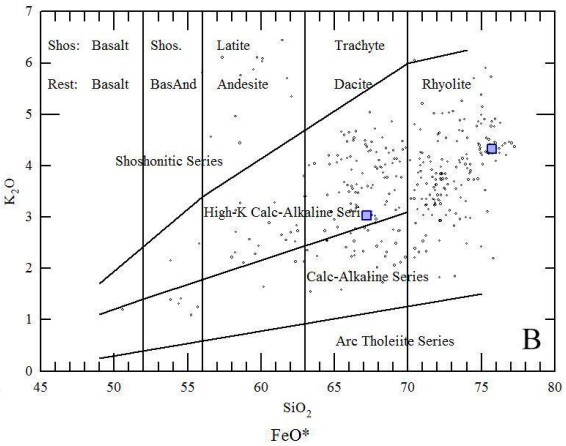
Shos: Basalt
Rest: Basalt
Shos. BasAnd
Latite Andesite
Trachyte Dacite
Rhyolite
Shoshonitic Series
High-K Calc-Alkaline Series
Calc-Alkaline Series
Arc Tholeiite Series
B
K2O
SiO2

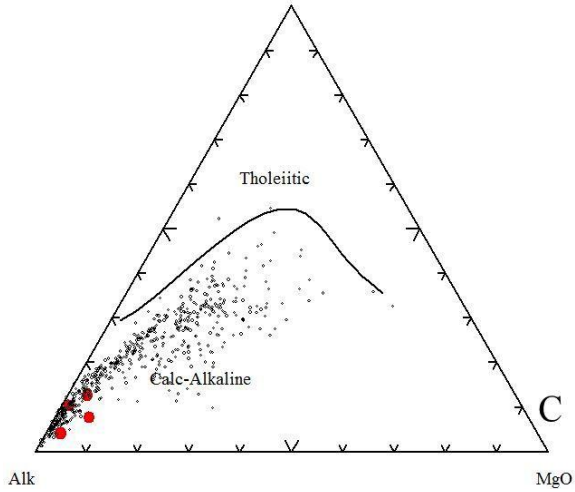
Tholeiitic
Calc-Alkaline
C
FeO*
Alk
MgO

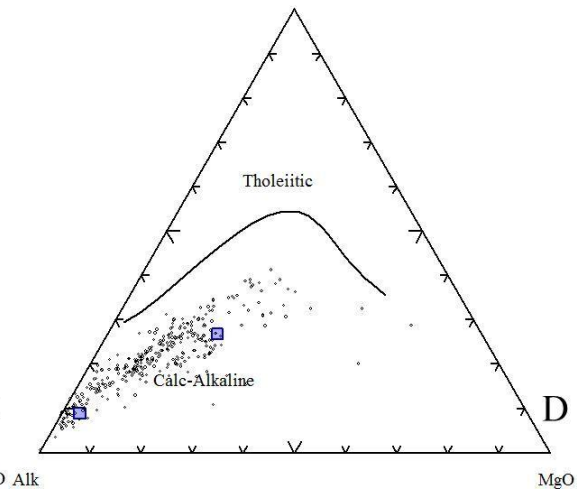
Tholeiitic
Calc-Alkaline
D
FeO*
Alk
MgO

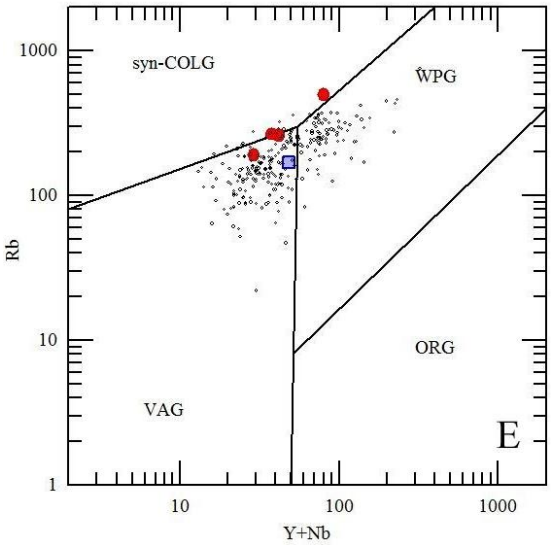
syn-COLG
WPG
ORG
VAG
E
Rb
Y+Nb

at 0.1% Mo was delineated. As of 2008 proven and probable reserves are 966 Mt at 0.068% MoS_2 (Huss, 2008).

The porphyry molybdenum deposit at Mt. Hope is spatially, temporally, and genetically related to a ~38 Ma eruptive center of rhyolites, rhyodacites, and dacites with both intrusive and extrusive phases. Two rhyolitic tuffs – the Mount Hope tuff and a quartz-eye tuff surround a central mass of intrusive quartz porphyry. Textural features shared between the tuffs and intrusives suggests they were comagmatic. Four phases of porphyritic intrusive rocks are present each composed of subhedral to euhedral quartz, K-feldspar, and plagioclase phenocrysts in a fine-grained matrix. The intrusions young successively from margin to core and show an increase in the grain size of the matrix. The earliest and most widespread intrusion crops out at the surface and forms numerous dikes cutting the carbonate country rocks. Where least altered this quartz porphyry shows resorbed quartz, euhedral K-feldspar, and oligoclase phenocrysts in a similar matrix with grain sizes <0.1 mm. Quartz porphyry is cut by younger aplitic quartz porphyry with a similar phenocryst composition but a coarser groundmass of 0.05 to 0.3 mm quartz and K-feldspar. An 80 m contact breccia of porphyry and Vinini skarn fragments separates the aplitic porphyry from the underlying granite porphyry. This granite porphyry contains 6-8 mm euhedral K-feldspar phenocrysts, 2-6 mm euhedral quartz phenocrysts, and finer grained oligoclase and biotite in a matrix of quartz, K-feldspar, and oligoclase 0.1-0.4 mm. Granite porphyry grades into, or is cut by, the deepest intrusion, coarse-grained quartz porphyry with a 0.05-0.2 mm quartz, K-feldspar, and oligoclase matrix. Dikes of biotite quartz monzonite porphyry are located ~1 km west of Mt. Hope and are cut by dikes of quartz porphyry. It is unknown whether these

dikes represent more mafic melts from the same chamber or have a different source. Dacite porphyry dikes occur north and east of Mt. Hope and are distinguished by their 12 mm resorbed quartz phenocrysts and euhedral biotite.

A comparison between intrusive rocks from Mt. Hope and Spruce Mountain reveals similarities in formation, composition, and associated mineralization along with several significant differences (Table 3). Both complexes were emplaced in the mid-Eocene and formed as subduction-related alkali-rich magma series. Shallowly emplaced and highly differentiated granite and rhyolite porphyries are the most common rock type. Potassic alteration is intense and pervasive in multiple intrusions and associated with quartz-molybdenite veins. Pb-Zn-Ag mineralization is found in limestone replacement deposits spatially associated with porphyritic intrusions.

Two notable differences at Spruce Mountain have direct implications on the potential for the formation of an economic molybdenum deposit. Fluorine concentrations in rhyolites at Spruce Mountain are generally lower than at Mt. Hope. Fluorine plays an important role in the formation of molybdenum deposits as it reduces magma viscosity, increases the solubility of water in magma, and lowers the crystallization temperatures of granitic magmas (Westra and Keith, 1981; White et al., 1981). These effects enhance the molybdenum concentration process. If fluorine values do not increase with depth at Spruce Mountain there does not appear to be a sufficient concentration to produce an economic molybdenum deposit. Micrographic textures have not been recognized at Spruce Mountain, but are closely associated with molybdenite mineralization at Mt. Hope. These textures form in the presence of water-rich magmas, generally with a separate chloride-rich aqueous phase (White et al., 1981). If

Table 3. Comparison of intrusive igneous rocks associated with porphyry Mo deposits.

	Spruce Mountain	Mt. Hope	Climax-type deposits
Rock types	Rhyolite porphyry, granite porphyry, aplite porphyry	Rhyolite porphyry, granite porphyry, aplite porphyry	Rhyolite porphyry, granite porphyry, aplite
Magma series	High K calc-alkalic	High K calc-alkalic	High K calc-alkalic, alkali-calcic
Tectonic setting	Subduction-related	Subduction-related	Subduction-related, back-arc spreading
Age (Ma)	37-39	36-40	17-36
Associated mineralization	Mo, Pb, Zn, Cu, Au, Ag, W	Mo, Pb, Zn, Ag, Cu, Au, Cd	Mo, W, Sn, Zn, Ag, Pb, Cu, U
Micrographic and crenulate textures	No	Yes	Yes
SiO_2 %	74-79	71-80	>75
TiO_2 %	0.06-0.17	0.02-0.18	<0.2
Rb ppm	190-495	31-540	200-800
Sr ppm	109-261	7-125	<125
Nb ppm	14-49	9-36	25-200
F ppm	368-3400	220-3300	5000-20000

micrographic textures are not present in granite porphyry with quartz-molybdenite veins at Spruce Mountain, it is possible that this is not a mineralizing intrusion and there is a deeper molybdenum source.

Given the similarities and differences between the igneous rocks of the Spruce Mountain district, Mt. Hope, and other Climax-type deposits, the Spruce Mountain district is a favorable setting for transitional Climax-type porphyry Mo mineralization. Drilling results from Freeport/AMAX exploration in the late 70's and early 80's indicated the presence of two mineralized systems, 105 Mt @ 0.05% MoS_2 at Kille Pass and 80 Mt @ 0.03% MoS_2 at Sprucemont. Alteration and mineralization patterns in several of the deeper holes at Kille Pass suggested Mo mineralization continued at depth but the project was terminated before this was tested (Jones, 1982).

Comparison with Jurassic and Eocene intrusions of the Carlin Trend

The relationship between igneous rocks and Carlin-type gold deposits has long been a source of controversy. Suggested models for the formation of Carlin-type deposits range from entirely amagmatic (Ilchik and Barton, 1997; Hofstra and Cline, 2000; Seedorff and Barton, 2004; Arehart, 1996; Cline et al., 2005) to partly magmatic (Henry and Boden, 1998; Henry and Ressel, 2000; Ressel et al., 2000) to an entirely magmatic origin (Sillitoe and Bonham, 1990; Johnston, 2003; Johnston and Ressel, 2004; Thompson, 2010). Igneous rocks are at least spatially associated with nearly all Carlin-type deposits in Nevada and often played an important role in their development by creating adjacent zones of high fracture density and serving as local aquitards to channel and trap hydrothermal fluids (Volk et al., 1995; Tretbar, 2004; Cline et al., 2005). Mafic intrusions may have donated iron to form reactive ferroan carbonates, which enhanced the precipitation of sulfides (Heitt et al., 2003; Fortuna et al., 2003). A genetic relationship between Carlin-type deposits and magmatism has been difficult to establish because coeval igneous rocks are present in some but not all districts, and metals, ore minerals, and alteration assemblages lack zoning relationships with Eocene igneous rocks (Cline et al., 2005; Ressel and Henry, 2006). Igneous rocks spatially associated with gold deposits of the Carlin trend were emplaced during four magmatic episodes – Jurassic, Cretaceous, Eocene, and Miocene.

Jurassic igneous rocks are associated with each of the more than 40 gold deposits of the Carlin trend (Teal and Jackson, 1997). The largest intrusion is the 157-158 Ma Goldstrike laccolith located in the northern Carlin trend with a total volume of ~3 km^3 (Bettles, 2002; Ressel and Henry, 2006). It is predominantly a quartz diorite with minor

zones of granodiorite and gabbro, and monzonite and diorite porphyry sills. The Little Boulder basin intrusion and Vivian sills with similar ages and compositions may have originally been a part of the Goldstrike intrusion prior to post-emplacement faulting (Chakurian, 2003). A halo of contact metamorphism extends up to 500 m into the surrounding rocks and is composed of diopside hornfels after carbonates, quartz hornfels after siliciclastics, and marble (Bettles, 2002). A small zone of exoskarn is present in the carbonates as well as endoskarn in the intrusion (Walck, 1989). SiO_2 values range from 57 to 66 percent for the various phases of the Goldstrike stock. High-angle lamprophyre dikes are abundant along the entire extent of the Carlin trend as a 3 to 4 km wide swarm with individual dikes ranging in width from 0.1 to 2 m. They are porphyritic with phenocrysts of phlogopite or amphibole set in a matrix of either alkali feldspar or plagioclase. SiO_2 values range from 51 to 55 percent. These lamprophyre dikes indicate the presence of deep structures that penetrated the mantle (Bettles, 2002). A swarm of porphyritic rhyolite dikes is located within a 5 km zone centered on the Goldstrike stock. Individual dikes are up to 15 m wide and 2 km long and contain a phenocryst assemblage of plagioclase, biotite, and quartz. REE patterns for each of the Jurassic rocks are concave up with LREE enriched relative to HREE. Rocks of the Goldstrike stock display overlapping REE patterns with the lamprophyres while the rhyolites have lower concentrations of REE (Ressel and Henry, 2006).

Eocene igneous rocks are also associated with all gold deposits along the Carlin trend and are more abundant than those of Jurassic age (Ressel and Henry, 2006). Eocene rocks include dikes and small stocks that record a nearly continuous eruptive episode that migrated southward from 42 to 34 Ma (duBray, 2007). High-angle

northwest-trending dikes are present along the entire length of the Carlin trend. Nearly all of the dikes are rhyolitic and dacitic, but several basaltic andesite dikes are present at the northern and southern ends of the trend. Textures range from coarsely porphyritic to aphanitic. These rocks are moderately alkalic like those of Jurassic age, but have experienced some alkali loss due to alteration. SiO_2 concentrations range from 77 to 66 percent for the rhyolites and dacites while the basaltic andesites contain ~55 percent. REE concentrations are highest in basaltic andesites and decrease with increasing SiO_2. Shallow Eocene stocks are present in the central and southern Carlin trend in Welches Canyon, Emigrant Pass, and the Rain district. These are small bodies with surface expressions <1 km^2 and compositions ranging from rhyolite to dacite. Textures range from aphanitic to coarsely porphyritic to fine-grained equigranular. SiO_2 contents range from 61 to 65 percent and REE concentrations show slight increases with increasing SiO_2 (Ressel and Henry, 2006).

Igneous rocks of the Spruce Mountain district are similar with those of the Carlin trend in terms of age, formation, composition, and alteration. While four ages of igneous rocks are present along the Carlin trend, only Jurassic and Eocene rocks are associated with each of the gold deposits. The Jurassic rhyolite and dacite at Spruce Mountain were emplaced within six million years of the Goldstrike stock and its associated dikes and sills. The Eocene rhyolite dikes and stocks at Spruce Mountain were emplaced during the 42-34 Ma period of magmatism along the Carlin trend. Subduction was the driver of both periods of magmatic activity at Spruce Mountain and the Carlin trend, producing high K calc-alkalic melts with compositions ranging from lamprophyres to rhyolites (Fig. 10). Jurassic intrusions along the Carlin trend are predominantly rhyolite and andesite,

while Jurassic intrusions at Spruce Mountain are rhyolite and dacite. Eocene intrusions along the Carlin trend are predominantly rhyolitic and dacitic while those within the Spruce Mountain district are rhyolitic. The highly silicic nature of the Eocene intrusions at Spruce Mountain requires the formation of a large magma chamber to accommodate the various differentiation processes (Hildreth, 1981). If there is a large Eocene magma chamber underlying the Spruce Mountain district similar to the several large plutons possibly underlying the Carlin trend, the potential for Carlin-type gold mineralization exists at Spruce Mountain (Ressel and Henry, 2006). Alteration of intrusions near or within Au deposits along the Carlin trend is commonly phyllic (Ressel, 2005) or argillic (Thompson, 2010) regardless of original composition. Intrusions in more distal settings from ore deposits show argillic alteration. Jurassic intrusions at Spruce Mountain are only weakly altered by chlorite, calcite, and sericite. Eocene intrusions all display moderate to intense hydrothermal alteration with argillic, phyllic, and potassic assemblages.

Figure 10. Discrimination diagrams featuring Eocene and Jurassic intrusions from Spruce Mountain and the Carlin trend. A. Tectonic setting diagram showing a volcanic arc affinity for Eocene intrusions at Spruce Mountain (red) and the Carlin trend (black). Sample SMIg45 plots in the within-plate field because of enrichment in Rb, Nb, and Y. This is likely due to alteration by fluorine-rich fluids in which the typically immobile Rb, Nb, and Yare mobilized. B. Jurassic intrusions at Spruce Mountain (blue) and the Carlin Trend (black) show volcanic arc affinities. C-D. K_2O vs. SiO_2 diagram showing the high K calc-alkaline nature of Eocene and Jurassic intrusions at Spruce Mountain and along the Carlin trend. E-F. Eocene intrusions along the Carlin trend are predominantly rhyolite and dacite while those within the Spruce Mountain district are strictly rhyolite. Jurassic intrusions along the Carlin trend are predominantly rhyolite and andesite while those within the Spruce Mountain district are rhyolite and dacite.

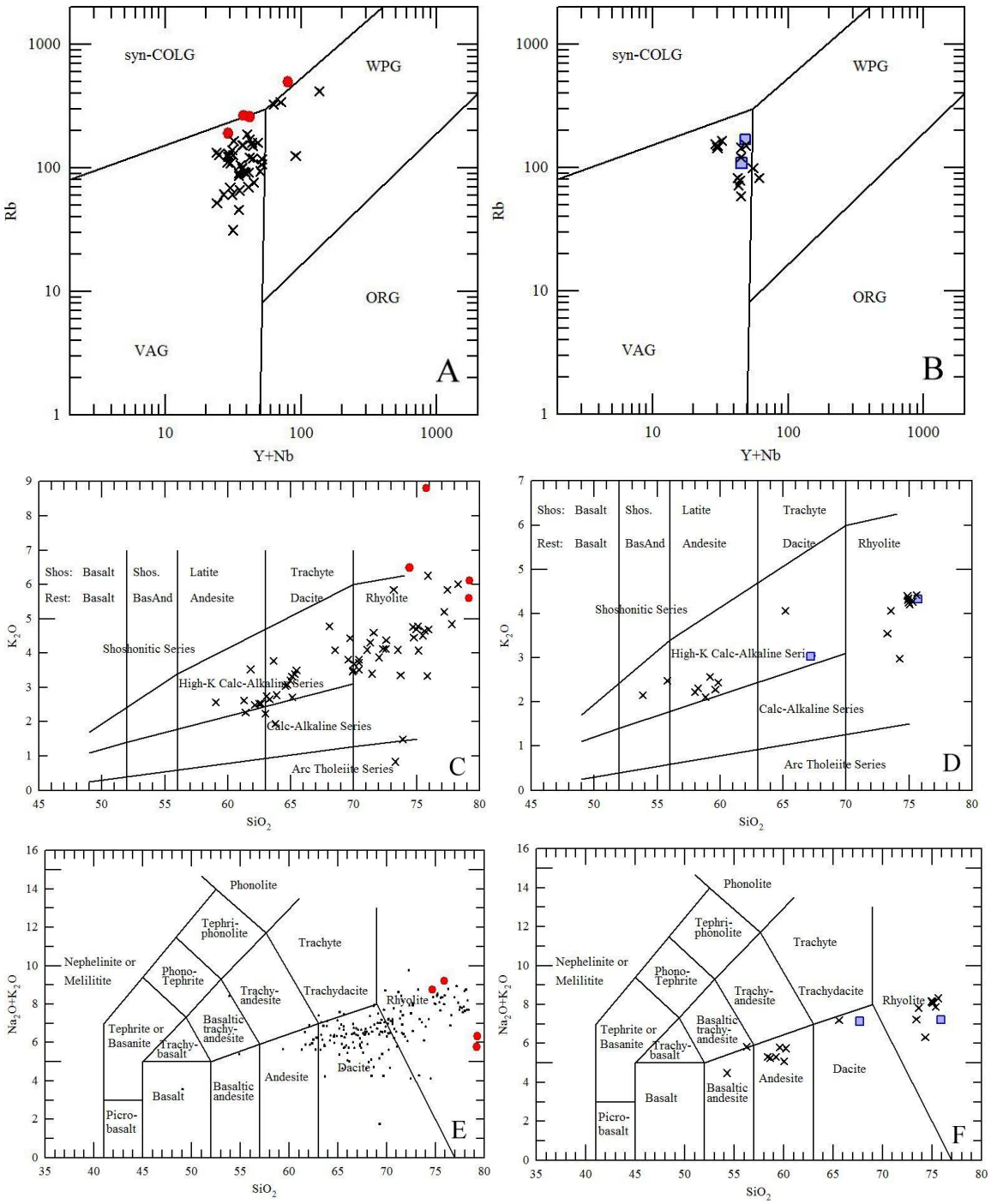
syn-COLG
WPG
ORG
VAG
A
B
Rb
Y+Nb
1000
100
10
1
Shos: Basalt
Rest: Basalt
Shos.
BasAnd
Latite
Andesite
Trachyte
Dacite
Rhyolite
Shoshonitic Series
High-K Calc-Alkaline Series
Calc-Alkaline Series
Arc Tholeiite Series
C
D
K2O
SiO2
Phonolite
Tephri-phonolite
Trachyte
Nephelinite or Melilitite
Phono-Tephrite
Trachy-andesite
Trachydacite
Rhyolite
Tephrite or Basanite
Trachy-basalt
Basaltic trachy-andesite
Andesite
Dacite
Basalt
Basaltic andesite
Picro-basalt
E
F
Na2O+K2O

Conclusions

This study has shown the nature and timing of igneous activity in the Spruce Mountain district. Dikes and stocks of dacite to rhyolite composition were emplaced during at least three events at 151-159 Ma, 39.1 Ma, and 37.7-37.3 Ma. Andesite and trachyandesite dikes were likely emplaced during one or more of these periods. Subduction was the driver of this high K calc-alkaline magmatism that may have formed one or more large magma chambers underlying the district. Jurassic intrusions were likely sourced from volatile-poor plutons and thus show only minor effects of hydrothermal alteration. Eocene intrusions were likely sourced from volatile-rich plutons which produced abundant hydrothermal fluids sufficient to alter the intrusions to argillic, phyllic, and potassic assemblages.

The intrusions at Spruce Mountain are similar in composition, timing, and alteration to intrusions associated with transitional Climax-type stockwork porphyry molybdenum deposits of western North America and Carlin-type gold deposits along the Carlin trend. The 1 billion pound molybdenum deposit at Mt. Hope is hosted in a complex of mid-Eocene high silica rhyolites and granites, which are similar to those found at Spruce Mountain. Because Climax-type molybdenum deposits are genetically related to these types of igneous rocks, the potential for economic molybdenum mineralization exists at Spruce Mountain. Carlin-type gold deposits may not share the same genetic tie to igneous activity, but pre-mineral intrusions help to localize ore fluids while coeval magmatism may serve as the heat source driving the hydrothermal system. The fact that Spruce Mountain has both Jurassic and Eocene intrusions like each of the

gold deposits along the Carlin trend makes it prospective ground for hosting Carlin-type gold mineralization.

Recommendations For Future Work

Further investigation of the igneous rocks within the Spruce Mountain district would provide a more complete understanding of the magmatic history of the area. A larger sample suite for geochemical analysis would allow identification of shared source plutons among the intrusive units. If there are multiple sources for the intrusions within the district they should each be located as they are prospective areas for mineralization. More radiometric data could better constrain the timing of igneous activity in the district. Several of the mafic dikes have unaltered amphiboles that could be used for ^{40}Ar-^{39}Ar dating. The U-Pb dates provided in this study could be improved by using ID-TIMS analysis with a precision of less than 0.1 percent.

References

Arehart, G.B., 1996, Characteristics and origin of sediment-hosted gold deposits: A review: Ore Geology Reviews, v. 11, p. 383-403.

Barton, M.D., 1996, Granitic magmatism and metallogeny of southwestern North America: Transactions of the Royal Society of Edinburgh–Earth Sciences, v. 87, p. 261-280.

Bettles, K., 2002, Exploration and geology, 1962 to 2002, at the Goldstrike property, Carlin trend, Nevada: Society of Economic Geologists Special Publication 9, p. 275-298.

Camilleri, P. A., and Chamberlain, K.R., 1997, Mesozoic Tectonics and Metamorphism in the Pequop Mountains and Wood Hills Region, Northeast Nevada: Implications for the Architecture and Evolution of the Sevier Orogen: GSA Bulletin 109.1, p. 74-94.

Cline, J.S., Hofstra, A.H., Muntean, J.L., and Tosdal, R.M., and Hickey, K.A., 2005, Carlin-type gold deposits in Nevada: Critical geologic characteristics and viable models: Economic Geology100th Anniversary Volume, p. 451-484.

Dickinson, W.R., 2006, Geotectonic evolution of the Great Basin: Geosphere, v. 2, no. 7, p. 353-368.

duBray, E.A., 2007, Time, space, and composition relations among northern Nevada intrusive rocks and their metallogenic implications: Geosphere, v. 3, no. 5, p. 381-405.

Fortuna, J., Kesler, S.E., and Stenger, D.P., 2003, Source of iron for sulfidation and gold deposition, Twin Creeks Carlin-type deposit, Nevada: Economic Geology v. 98. p. 1213-1224.

Granger, A.E., 1957, Geology and Mineral Resources of Elko County, Nevada: NBMG Bulletin, v. 54, p. 137-147.

Harlow, G.R., 1956, The Stratigraphy and Structure of the Spruce Mountain Area, Elko County, Nevada: M.S thesis, University of Washington, 65 p.

Heitt, D.G., Dunbar, W.W., Thompson, T.B., and Jackson, R.G., 2003, Geology and geochemistry of the Deep Star gold deposit, Carlin trend, Nevada: Economic Geology, v. 98, p. 1107-1136.

Henry, C.D., and Boden, D.R., 1998, Eocene magmatism: The heat source for Carlin-type gold deposits of northern Nevada: Geology, v. 26, p. 1067-1070.

Henry, C.D., and Ressel, M.W., 2000, Eocene magmatism of northeastern Nevada: The smoking gun for Carlin-type gold deposits: Geological Society of Nevada, Geology and Ore Deposits 2000: The Great Basin and Beyond Symposium, Reno/Sparks, Nevada, May 15-18, 2000, Proceedings, p. 365-388.

Hildreth, W., 1981, Gradients in silicic magma chambers: Implications for lithospheric magmatism: Journal of Geophysical Research, v. 86, p. 10153-10192.

Hofstra, A.H., and Cline, J.S., 2000, Characteristics and models for Carlin-type gold deposits: Reviews in Economic Geology, v. 13, p. 163-220.

Hope, R.A., 1972, Geologic Map of the Spruce Mountain Quadrangle, Elko County, Nevada.

Humphreys, E.D., 1995, Post-Laramide removal of the Farallon slab, western United States: Geology, v. 23, p. 987-990.

Huss, C., 2008, NI 43-101 Technical Report Mount Hope Project, 138 p.

Ilchik, R.P., and Barton, M.D., 1997, An amagmatic origin of Carlin-type gold deposits: Economic Geology, v. 92, p. 269-288.

Johnston, M.K., 2003, Geology of the Cove Mine, Lander County, Nevada, and a genetic model for the McCoy-Cove magmatic-hydrothermal system: Unpublished Ph.D. dissertation, University of Nevada, Reno, 353 p.

Johnston, M.K., and Ressel, M.W., 2004, Carlin-type and distal-disseminated Au-Ag deposits: Related distal expressions of Eocene intrusive centers in north-central Nevada: Society of Economic Geologists Newsletter 59, p. 12-14.

Jones, M.B., 1980, Spruce Mountain Project, Elko County, Nevada, 1979 Progress Report: Freeport Exploration Company internal memorandum, 42 p.

Keith, S.B., 1978, Paleosubduction geometries inferred from Cretaceous and Tertiary magmatic patterns in southwestern North America: Geology, v. 6, p. 516-521.

Pearce, J.A., Harris, N.B.W., and Tindle, A.G., 1984, Trace Element Discrimination Diagrams for the Tectonic Interpretation of Granitic Rocks: Journal of Petrology, v. 25, no. 4, p. 956-983.

Ressel, M.W., 2005, Igneous Geology of the Carlin Trend, Nevada: The Importance of Eocene Magmatism in Gold Mineralization: PhD dissertation, University of Nevada, Reno, 299 p.

Ressel, M.W., and Henry, C.D., 2006, Igneous Geology of the Carlin Trend, Nevada: Development of the Eocene Plutonic Complex and Significance for Carlin-Type Gold Deposits: Economic Geology, v. 101, p. 347-383.

Ressel, M.W., Noble. D.C., Henry, C.D., and Trudel, W.S., 2000, Dike-hosted ores of the Beast deposit and the importance of Eocene magmatism in gold mineralization of the Carlin trend, Nevada: Economic Geology, v. 95, p. 1417-1444.

Schrader, F.C., 1931, Spruce Mountain District Elko County: University of Nevada Bulletin, v. 25, no. 7, 24 p.

Seedorff, E., and Barton, M.D., 2004, Enigmatic origin of Carlin-type deposits: an amagmatic solution?: Society of Economic Geologists Newsletter 59, p. 14-18.

Sillitoe, R.H., and Bonham, H.F., 1990, Sediment-hosted gold deposits: Distal products of magmatic-hydrothermal systems: Geology, v. 18 p. 157-161.

Spadafora, M.J., 1979, Spruce Mountain Project, Elko County, Nevada, Report on 1978 Field Season: Freeport Exploration Company internal memorandum, 75 p.

Speed, P., Elison, M.W., and Heck, F.R., 1988, Phanerozoic tectonic evolution of the Great Basin *in* Ernst, W.G., Metamorphism and crustal evolution of the western United States, p. 572-605.

Teal, L., and Jackson, M., 1997, Geologic overview of the Carlin trend gold deposits and descriptions of recent deep discoveries *in* Vikre, P., Thompson, T.B., Bettles, K., Christensen, O., and Parratt, R. eds., Carlin-type Gold Deposits Field Conference, Society of Economic Geologists Guidebook Series, v. 28, p. 3-37.

Thompson, T.B., 2010, Origin of Fluids Associated with Carlin-type Ore Systems *in* Steininger, R., and Pennell, B., eds., Great Basin Evolution and Metallogeny: Geological Society of Nevada Symposium Proceedings, Reno/Sparks, Nevada, May 2010, p. 201-219.

Tingley, J.V., 1981, Summary Report, Mineral Inventory of the Wells Resource Area, Elko District, Elko County, Nevada: NBMG Open-File Report 81-4, 50 p.

Tosdal, R.M., Wooden, J.L., and Kistler, R.W., 2000, Geomotery of the Neoproterozoic continental breakup, and implications for location of Nevadan mineral belts: Geological Society of Nevada, Geology and Ore Deposits 2000: The Great Basin and Beyond Symposium, Reno/Sparks, Nevada, May 15-18, 2000, Proceedings, p. 451-466.

Tretbar, D.R., 2004, The geology and geochemistry of the 194 orebody, Getchell Mine, Humboldt County, Nevada: Unpublished M.S. thesis, University of Nevada, Reno.

Volk, J., Lauha, E., Leonardson, R., and Rahn, J., 1995, Structural geology of the Betze-Post and Meikle deposits, Elko and Eureka Counties, *in* Green, S., ed., Trip B – Structural Geology of the Carlin trend, Geology and Ore Deposits of the American Cordillera: Geological Society of Nevada Field tip Guidebook, Reno, p. 180-194.

Walck, C.M., 1989, Petrology and petrography of the metamorphic aureole associated with the deep post orebody, Eureka County, Nevada: M.S. thesis, University of Missouri, Rolla, 49 p.

Westra, G., and Keith, S.B., 1981, Classification and Genesis of Stockwork Molybdenum Deposits: Economic Geology v. 76, p. 844-873.

Westra, G., and Riedell, K.B., 1996, Geology of the Mount Hope stockwork molybdenum deposit, Eureka County, Nevada, *in* Coyner, A.R., and Fahey, P.L., eds., Geology and Ore Deposits of the America Cordillera: Geological Society of Nevada Symposium Proceedings, Reno/Sparks, Nevada, April 1995, p. 1639-1666.

White, W.H., Bookstrom, A.A., Kamilli, R.J., Ganster, M.W., Smith, R.P., Ranta, D.E., and Steininger, R.C., 1981, Character and Origin of Climax-Type Molybdenum Deposits: Economic Geology, 75th Anniversary Volume, p. 270-316.

Winchester, J.A., and Floyd, P.A., 1977, Geochemical discrimination of different magma series and their differentiation products using immobile elements: Chemical Geology, v. 20, p. 325-343.

Wolverson, N.J., 2010, Technical Report on the Spruce Mountain Property, Elko County, Nevada, USA, 79 p.

Zoback, M.L., McKee, E.H., Blakely, R.J., and Thompson, G.A., 1994, The northern Nevada rift: Regional tectono-magmatic relations and middle Miocene stress direction: GSA Bulletin, v. 106, p. 371-382

Appendix A – Whole-rock Geochemical Data

Sample	SMlg41	SMlg42	SMlg43	SMlg44	SMlg45	SMlg46
Location	680516, 4487718	680387, 4487543	679756, 4492990	679937, 4492126	680682, 4490741	683420, 4493380
Rock type	Andesite	Andesite	Andesite	Rhyolite	Rhyolite	Rhyolite
SiO_2	57.21	53.81	55.33	79.22	79.17	75.74
TiO_2	1.09	1.06	1.15	0.05	0.06	0.10
Al_2O_3	16.36	15.68	15.58	13.13	13.13	14.33
Fe_2O_2	8.07	7.55	8.02	0.82	0.58	0.82
MnO	0.08	0.12	0.10	0.01	0.01	0.02
MgO	8.06	6.43	7.05	0.12	0.46	0.30
CaO	5.72	10.42	6.53	0.27	0.78	1.25
Na_2O	0.04	0.02	3.45	0.20	0.16	2.88
K_2O	3.02	4.30	1.97	6.11	5.60	4.33
P_2O_5	0.22	0.32	0.45	0.01	0.01	0.06
Ba	459	1797	1773	386	228	1047
Ce	52.7	91.9	106.2	28.7	32.7	93.0
Cr	505	270	439	10	10	5
Cs	4.90	27.96	1.59	2.91	5.28	4.70
Dy	4.01	4.50	4.74	2.81	5.45	3.90
Er	2.29	2.34	2.50	1.79	2.88	2.01
Eu	1.32	1.90	1.93	0.34	0.10	1.54
Ga	18.3	19.0	17.4	15.8	25.5	18.5
Gd	4.50	5.84	5.59	2.57	4.41	5.04
Hf	4.17	4.46	5.02	3.50	4.10	3.23
Ho	0.79	0.87	0.89	0.59	1.02	0.71
La	25.3	46.5	55.6	15.0	16.0	47.3
Lu	0.31	0.29	0.33	0.28	0.37	0.26
Nb	9.1	12.5	20.0	24.2	48.5	26.8
Nd	26.2	42.1	44.3	12.4	13.9	37.0
Pr	6.5	10.7	11.9	3.4	3.9	10.4
Rb	139	311	61	260	495	170
Sm	5.22	7.78	7.59	2.98	4.26	7.02
Sn	1	1	1	2	10	2
Sr	131	438	845	36	109	365
Ta	0.5	0.7	1.2	2.5	6.6	2.0
Tb	0.65	0.80	0.77	0.43	0.80	0.68
Th	5.2	7.4	10.8	26.4	21.8	14.5
Tl	0.9	1.2	0.3	1.9	4.3	0.6

Tm	0.30	0.29	0.32	0.26	0.40	0.26
U	1.37	2.20	2.60	6.85	7.97	4.24
V	204	201	153	3	3	3
W	2	4	1	3	4	2
Y	22.62	23.85	25.00	18.03	31.79	21.67
Yb	1.97	1.95	2.13	1.73	2.57	1.71
Zr	163	168	223	73	69	79
As	7.6	2.9	11.1	8.0	3.4	0.6
Bi	0.10	0.09	0.03	0.07	0.15	0.04
Hg	0.356	0.155	0.013	0.005	0.012	0.009
Sb	0.87	0.74	0.15	0.37	0.33	0.03
Se	0.4	0.6	0.6	0.9	0.6	0.4
Te	0.46	0.13	0.01	0.01	0.02	0.01
Ag	0.88	0.29	0.52	6.90	0.51	0.26
Cd	0.27	0.29	0.26	3.09	0.26	0.26
Co	25.3	27.0	26.1	0.5	0.5	0.5
Cu	37	40	38	19	1	1
Mo	1	1	1	1	1	1
Ni	156	78	141	1	4	1
Pb	1	2	6	36	12	17
Zn	66	59	64	6542	45	52
F	813	658	669	299	656	510
Au	0.12	0.04	0.00	0.00	0.00	0.00

Sample	SMlg47	SMlg48	SMlg49	SMlg50	SMlg51
Location	684690, 4491810	686002, 4492844	685957, 4492716	684044, 4493328	686910, 4492715
Rock type	Dacite	Andesite	Granite	Trachyandesite	Rhyolite
SiO_2	67.20	52.83	74.45	53.49	75.76
TiO_2	0.64	1.03	0.17	0.81	0.08
Al_2O_3	15.27	14.27	13.38	11.92	12.68
Fe_2O_2	4.09	7.62	1.47	8.52	0.45
MnO	0.06	0.12	0.02	0.17	0.03
MgO	2.96	8.40	0.41	8.07	0.30
CaO	2.10	8.98	1.17	11.33	1.35
Na_2O	4.06	2.07	2.23	0.93	0.37
K_2O	3.03	3.93	6.49	3.97	8.81
P_2O_5	0.25	0.33	0.04	0.44	0.01
Ba	1905	1714	1180	1477	1163
Ce	88.4	97.0	39.4	125.1	6.4
Cr	114	665	20	677	20
Cs	1.35	13.86	3.55	2.58	1.61
Dy	3.50	4.10	2.49	4.55	2.69
Er	1.82	2.03	1.35	2.11	1.56
Eu	1.21	1.78	0.69	2.46	0.15
Ga	19.7	18.8	19.5	15.3	17.1
Gd	4.18	5.43	2.73	7.06	1.97
Hf	5.18	4.13	2.96	4.19	2.49
Ho	0.63	0.74	0.47	0.78	0.53
La	48.4	51.9	21.1	66.6	3.3
Lu	0.23	0.24	0.19	0.25	0.22
Nb	26.4	32.8	14.4	15.9	20.9
Nd	33.8	40.7	16.0	54.9	3.5
Pr	9.3	10.8	4.3	14.3	0.8
Rb	109	143	190	121	266
Sm	5.87	7.02	3.24	9.90	1.43
Sn	2	3	2	1	1
Sr	785	1109	242	687	261
Ta	2.0	1.9	1.4	0.8	2.8
Tb	0.59	0.71	0.41	0.85	0.41
Th	15.4	8.8	15.3	14.2	16.8
Tl	0.5	0.5	0.6	1.3	0.9

Tm	0.24	0.25	0.17	0.25	0.23
U	5.26	2.52	5.60	3.40	4.53
V	69	196	17	212	6
W	2	2	60	2	2
Y	19.16	20.77	14.71	22.34	16.90
Yb	1.51	1.61	1.19	1.51	1.47
Zr	206	164	88	162	54
As	0.7	1.0	1.0	3.7	1.0
Bi	0.08	0.05	0.12	0.02	0.07
Hg	0.018	0.011	0.061	0.014	0.015
Sb	0.06	0.09	0.13	0.06	0.07
Se	0.5	0.5	0.4	0.5	0.3
Te	0.01	0.02	0.03	0.01	0.01
Ag	0.26	0.25	0.26	0.75	1.29
Cd	0.26	0.50	0.26	0.27	0.50
Co	11.4	26.2	1.0	33.3	0.5
Cu	13	1	41	23	24
Mo	1	1	10	1	1
Ni	60	146	2	97	3
Pb	21	7	13	6	6
Zn	75	96	13	89	9
F	683	1754	368	1106	428
Au	0.00	0.00	0.00	0.00	0.00

Appendix B – U-Pb Dating Methodology and Data

U-Pb dates were obtained by the laser ablation inductively coupled plasma mass spectrometry (LA-ICP-MS) method from spots placed on zircon in six samples. Zircon grains were separated from rocks using standard techniques and mounted in epoxy and polished until the center of the grains were exposed. Cathodoluminescence (CL) images were obtained with a JEOL JSM-1300 scanning electron microscope and Gatan MiniCL. CL images were used to guide the placement of LA-ICPMS spots.

U-Pb isotope systematics and trace element compositions were analyzed by LA-ICPMS using a ThermoElectron X-Series II quadrupole ICPMS and New Wave Research UP-213 Nd:YAG UV (213 nm) laser ablation system. In-house analytical protocols, standard materials, and data reduction software were used for simultaneous acquisition and real-time calibration of U-Pb dates and a suite of HFSE and REE elements using the high sensitivity and unique properties of the interface (Xs cones), extraction lens, and quadrupole analyzer of the X-Series II. Zircons were ablated with a laser diameter of 25 microns using fluence and pulse rates of 5 J/cm^2 and 10 Hz, respectively, during a 30 second analysis (15 sec gas blank, 45 sec ablation) that excavated a pit ~25 μm deep. Ablated material was carried by a 1.2 L/min He gas stream to the nebulizer flow of the plasma. Dwell times were 5 ms for Si and Zr; 100 ms for ^{49}Ti and ^{207}Pb, 40 ms for ^{238}U, ^{232}Th, ^{202}Hg, ^{204}Pb, ^{206}Pb and ^{208}Pb isotopes; and 10 ms all other HFSE and REE elements. Background count rates for each analyte were obtained prior to each spot analysis and subtracted from the raw count rate for each analyte.

For U-Pb dates, instrumental fractionation of the background-subtracted ^{206}Pb/^{238}U and ^{207}Pb/^{206}Pb ratios was corrected, and dates were calibrated with respect to

interspersed measurements of the Plesovice zircon standard (Sláma et al., 2008). Signals at mass 204 were indistinguishable from zero following subtraction of mercury backgrounds measured during the gas blank (<1000 cps ^{202}Hg), and thus dates are reported without common Pb correction. Radiogenic isotope ratio and age error propagation for each spot includes uncertainty contributions from counting statistics and background subtraction. For concentration calculations, background-subtracted count rates for each analyte were internally normalized to ^{29}Si and calibrated with respect to NIST SRM-610 and -612 glasses as the primary standards.

Errors on weighted mean ^{206}Pb/^{238}U dates given below are presented at 2σ as follows: weighted mean date ± x / y, where x is the internal error and y is the error including the uncertainty on the standard calibration, which are propagated in quadrature. Weighted mean calculations were performed using Isoplot 3.0 (Ludwig, 2003). A standard calibration uncertainty of 1.0% (2σ) is used because that is the average of these experiments. In Table 1 errors on single dates do not include uncertainties on the standard calibration.

Zircon standard AUSZ2 was measured as an unknown during the experiment as a quality control standard. Twenty-three analyses of AUSZ2 yielded a weighted mean ^{206}Pb/^{238}U date of 38.4 ± 0.4 / 0.5 Ma, in agreement with the CA-TIMS weighted mean date of 38.86 ± 0.01 Ma (2σ internal error, unpublished data, Boise State University).

Table B-1. LA-ICP-MS data from sample SMIg44

Analysis	U ppm	Th ppm	Pb* ppm	Th/U	206Pb 204Pb	206Pb* 207Pb*	±2σ (%)	207Pb* 235U*	±2σ (%)	206Pb* 238U	±2σ (%)	error corr.	238U 206Pb*	±2σ (%)	207Pb* 206Pb*	±2σ (%)	error corr.	207Pb* 206Pb*	±2σ (Ma)	207Pb* 235U	±2σ (Ma)	206Pb* 238U*	±2σ (Ma)
SMIg44																							
SMIg44 M 76 5/16/201	2253	972	18.5	0.43	2928.04	20.9834	4.28	0.04336	6.483	0.0066	4.869	0.75	151.551	4.869	0.04766	4.28	1.70471E-16	82	102	43	3	42.4	2.1
SMIg44 M 84 5/16/201	3255	878	23.5	0.27	2201.52	21.3501	3.941	0.0408	7.113	0.00632	5.921	0.83	158.302	5.921	0.04684	3.941	0	41	94	41	3	40.6	2.4
SMIg44 M 79 5/16/201	4267	1419	29.5	0.33	716.555	21.0276	3.791	0.04111	6.673	0.00627	5.492	0.82	159.491	5.492	0.04756	3.791	0	77	90	41	3	**40.3**	**2.2**
SMIg44 M 75 5/16/201	2198	830	16.6	0.38	3534.6	20.9569	5.285	0.04085	6.924	0.00621	4.474	0.65	161.057	4.474	0.04772	5.285	0	85	125	41	3	**39.9**	**1.8**
SMIg44 M 88 5/16/201	2909	806	21	0.28	2754.99	21.0877	2.591	0.04049	5.406	0.00619	4.744	0.88	161.48	4.744	0.04742	2.591	-2.8899E-16	70	62	40	2	**39.8**	**1.9**
SMIg44 M 83 5/16/201	6136	2692	47.5	0.44	21662	21.8153	4.567	0.03908	7.979	0.00618	6.543	0.82	161.714	6.543	0.04584	4.567	2.37796E-16	-11	110	39	3	**39.7**	**2.6**
SMIg44 M 82 5/16/201	6629	3108	53	0.47	1876	18.2508	10.35	0.04669	12.39	0.00618	6.809	0.55	161.795	6.809	0.05479	10.35	2.01733E-16	404	232	46	6	**39.7**	**2.7**
SMIg44 M 87 5/16/201	5314	1879	38.6	0.35	729.614	16.0512	11.52	0.05298	13.31	0.00617	6.674	0.5	162.144	6.674	0.0623	11.52	-3.6961E-16	684	246	52	7	**39.6**	**2.6**
SMIg44 M 70 5/16/201	4080	1194	28.6	0.29	1505.09	20.2953	4.558	0.04177	7.81	0.00615	6.343	0.81	162.63	6.343	0.04927	4.558	4.91591E-16	161	107	42	3	**39.5**	**2.5**
SMIg44 M 81 5/16/201	5879	2848	45.5	0.48	4487.04	21.1574	3.765	0.03985	5.949	0.00612	4.605	0.77	163.531	4.605	0.04726	3.765	2.04884E-16	63	90	40	2	**39.3**	**1.8**
SMIg44 L 5 5/16/2012	4760	1821	23.7	0.38	1179.15	21.5586	1.876	0.0388	4.705	0.00607	4.315	0.92	164.824	4.315	0.04639	1.876	0	18	45	39	2	**39.0**	**1.7**
SMIg44 M 71 5/16/201	3440	1075	24.1	0.31	1849.01	21.7167	5.693	0.03834	8.355	0.00604	6.116	0.73	165.603	6.116	0.04605	5.693	0	0	137	38	3	**38.8**	**2.4**
SMIg44 M 78 5/16/201	4202	1232	29.2	0.29	2063.06	20.8773	3.941	0.03953	6.024	0.00598	4.556	0.76	167.09	4.556	0.0479	3.941	1.97855E-16	94	93	39	2	**38.5**	**1.7**
SMIg44 M 69 5/16/201	6225	2953	41.8	0.47	444.318	15.8354	10.6	0.05198	12.53	0.00597	6.694	0.53	167.505	6.694	0.06315	10.6	-2.0035E-16	713	225	51	6	**38.4**	**2.6**
SMIg44 M 73 5/16/201	4361	1082	30.2	0.25	8206.27	21.0859	3.407	0.03896	4.898	0.00596	3.519	0.72	167.835	3.519	0.04743	3.407	1.48164E-16	71	81	39	2	**38.3**	**1.3**
SMIg44 M 80 5/16/201	4991	2158	36.8	0.43	2546.55	19.9656	4.298	0.04101	5.476	0.00594	3.393	0.62	168.387	3.393	0.05009	4.298	0	199	100	41	2	**38.2**	**1.3**
SMIg44 M 72 5/16/201	5204	1879	35.5	0.36	1118.4	20.9615	2.905	0.03903	5.426	0.00593	4.582	0.84	168.516	4.582	0.04771	2.905	0	85	69	39	2	**38.1**	**1.7**
SMIg44 L 4 5/16/2012	5082	2046	23.8	0.40	1218.78	22.1039	3.204	0.03687	5.756	0.00591	4.781	0.83	169.189	4.781	0.04524	3.204	0	-43	78	37	2	**38.0**	**1.8**
SMIg44 M 85 5/16/201	6683	3271	45	0.49	647.426	21.7624	3.11	0.03742	7.938	0.00591	7.304	0.92	169.328	7.304	0.04595	3.11	-3.1279E-16	-5	75	37	3	**38.0**	**2.8**
SMIg44 M 86 5/16/201	7651	4236	58.6	0.55	3262.71	21.7164	4.091	0.03748	7.659	0.0059	6.475	0.85	169.413	6.475	0.04605	4.091	0	0	99	37	3	**37.9**	**2.4**
SMIg44 M 67 5/16/201	6111	2422	41.9	0.40	1647.78	21.4794	3.699	0.03767	5.667	0.00587	4.293	0.76	170.392	4.293	0.04656	3.699	2.23733E-16	27	89	38	2	**37.7**	**1.6**
SMIg44 M 74 5/16/201	5791	3001	41.3	0.52	912.644	21.0976	3.367	0.03832	4.954	0.00586	3.634	0.73	170.547	3.634	0.0474	3.367	-1.4519E-16	69	80	38	2	**37.7**	**1.4**
SMIg44 M 77 5/16/201	4576	1643	31.4	0.36	1825.09	21.8109	3.859	0.03668	6.403	0.0058	5.109	0.8	172.339	5.109	0.04585	3.859	-3.6038E-16	-10	93	37	2	**37.3**	**1.9**
SMIg44 L 8 5/16/2012	5317	1615	28.7	0.30	673.754	20.957	3.186	0.03794	5.162	0.00577	4.062	0.79	173.402	4.062	0.04772	3.186	0	85	76	38	2	**37.1**	**1.5**
SMIg44 L 3 5/16/2012	4596	1791	20.3	0.39	2643.81	20.6179	2.491	0.03854	5.176	0.00576	4.537	0.88	173.539	4.537	0.0485	2.491	1.57199E-16	124	59	38	2	**37.0**	**1.7**
SMIg44 L 10 5/16/2012	2895	849	16.3	0.29	460.987	20.9779	3.852	0.03758	5.231	0.00572	3.539	0.68	174.893	3.539	0.04767	3.852	1.30287E-16	83	91	37	2	**36.8**	**1.3**
SMIg44 L 1 5/16/2012	6506	3238	20.6	0.50	1712.77	15.0368	4.754	0.05209	5.698	0.00568	3.142	0.55	176.035	3.142	0.0665	4.754	-2.3788E-16	822	99	52	3	**36.5**	**1.1**
SMIg44 M 68 5/16/201	5676	2208	39.1	0.39	5414.53	20.2479	3.865	0.03865	7.611	0.00568	6.557	0.86	176.182	6.557	0.04939	3.865	-2.8037E-16	166	90	39	3	**36.5**	**2.4**
SMIg44 L 6 5/16/2012	6177	2148	28	0.35	2629.03	21.2608	3.546	0.03655	5.706	0.00564	4.471	0.78	177.433	4.471	0.04703	3.546	2.24111E-16	51	85	36	2	**36.2**	**1.6**
SMIg44 L 2 5/16/2012	4063	1855	18	0.46	759.464	20.6529	4.363	0.03726	6.609	0.00558	4.964	0.75	179.159	4.964	0.04842	4.363	0	120	103	37	2	**35.9**	**1.8**
SMIg44 L 7 5/16/2012	4590	1528	21.3	0.33	2334.35	20.7384	3.475	0.03695	5.073	0.00556	3.696	0.73	179.91	3.696	0.04822	3.475	0	110	82	37	2	**35.7**	**1.3**
SMIg44 L 9 5/16/2012	4153	1468	19.5	0.35	1460.99	21.3497	3.219	0.03582	4.924	0.00555	3.727	0.76	180.307	3.727	0.04684	3.219	-1.481E-16	41	77	36	2	**35.7**	**1.3**

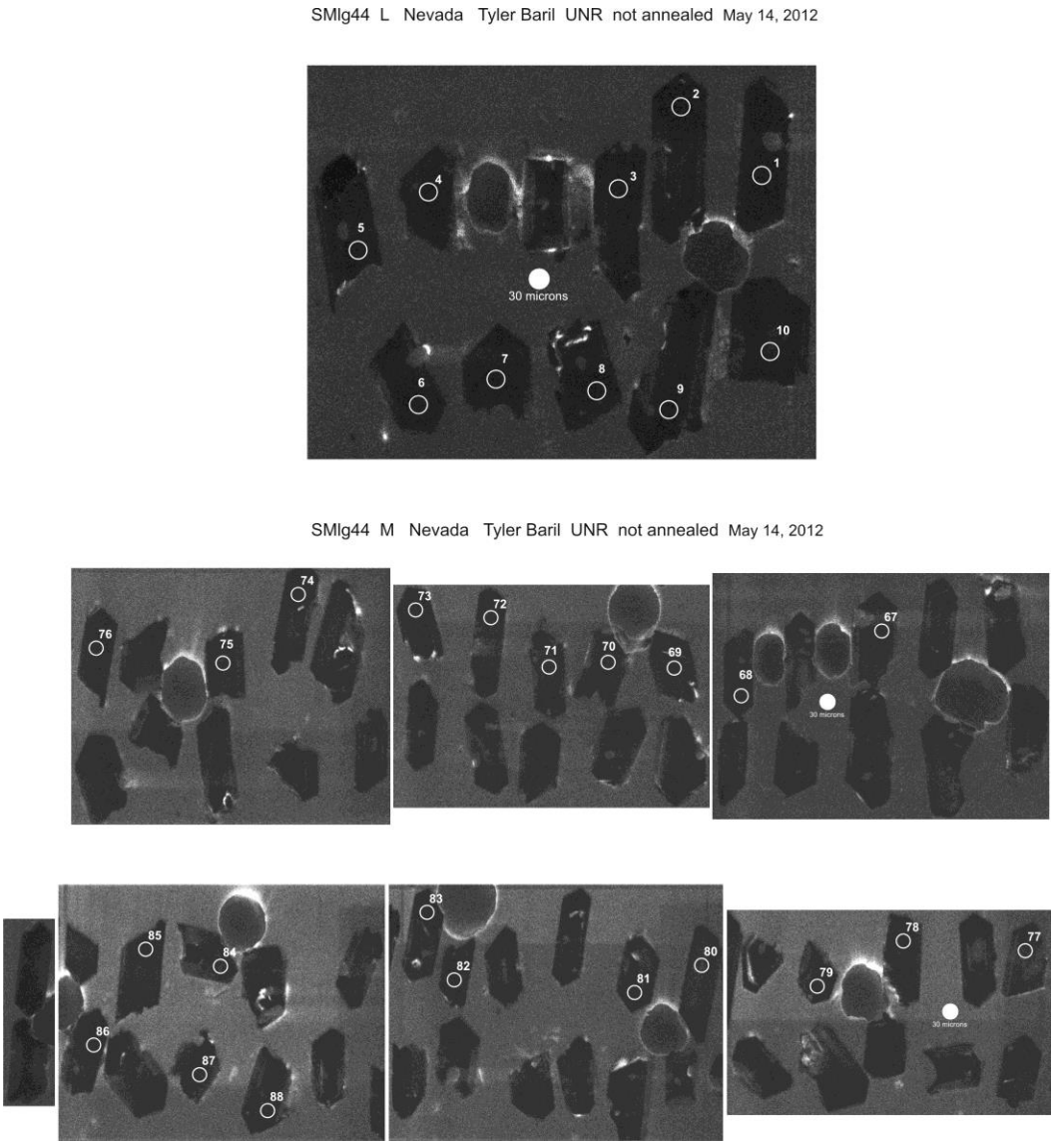

Figure B-1. Cathodeluminescence images of zircons from SMIg44.

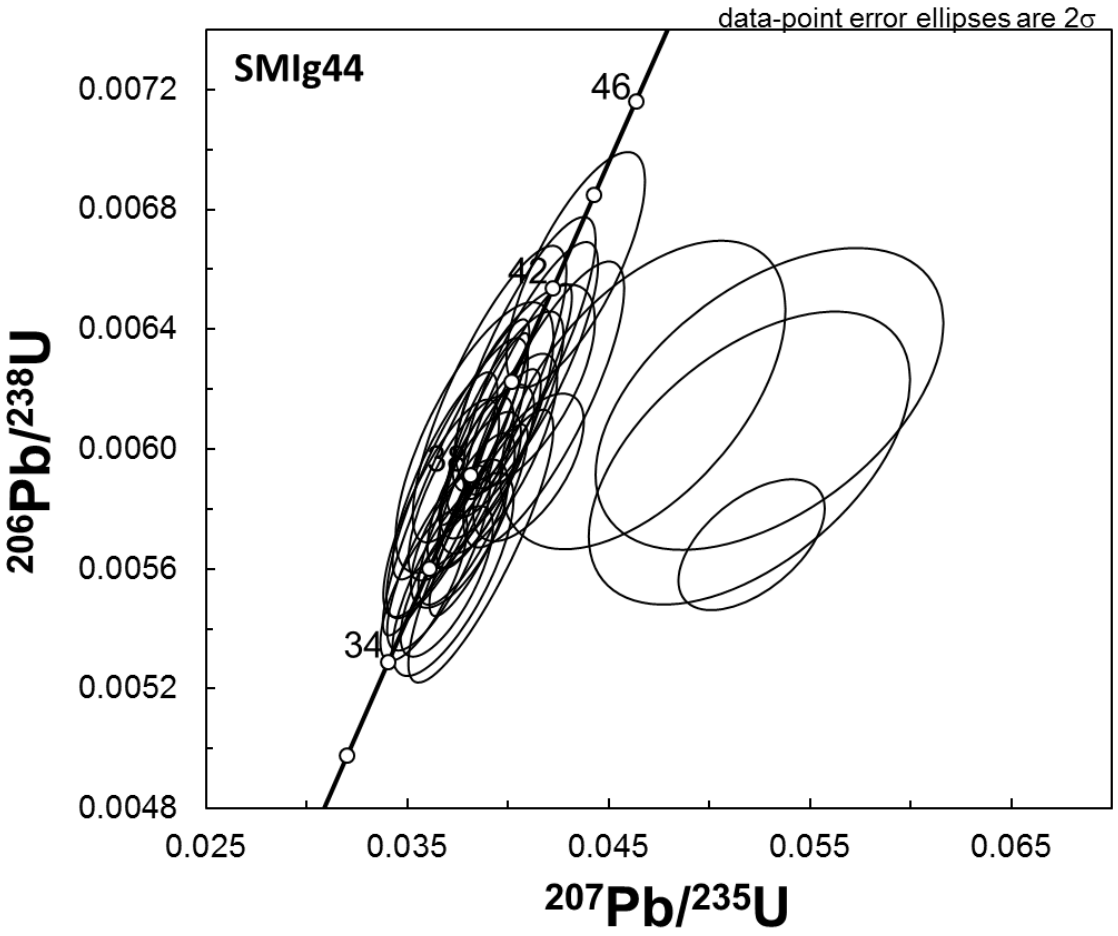

Figure B-2. Concordia plot of zircon ages from SMIg44.

Table B-2. LA-ICP-MS data from sample SMIg45.

Analysis		U ppm	Th ppm	Pb* ppm	Th/U	206Pb 204Pb	206Pb* 207Pb*	±2σ (%)	207Pb* 235U*	±2σ (%)	206Pb* 238U	±2σ (%)	error corr.	238U 206Pb*	±2σ (%)	207Pb* 206Pb*	±2σ (%)	error corr.	207Pb* 206Pb*	±2σ (Ma)	207Pb* 235U	±2σ (Ma)	206Pb* 238U*	±2σ (Ma)
SMIg45																								
SMIg45 L 15	5/16/2012	336	186	2.66	0.55	55.1688	10.3333	10.23	0.0836	11.81	0.00626	5.9	0.5	159.618	5.9	0.09677	10.23	-2.3543E-16	1563	192	82	9	**40.3**	**2.4**
SMIg45 M 105	5/16/20	434	324	2.43	0.75	193.366	20.0503	9.044	0.04204	10.41	0.00611	5.154	0.5	163.565	5.154	0.04987	9.044	1.52452E-16	189	210	42	4	**39.3**	**2.0**
SMIg45 M 95	5/16/201	491	292	3.12	0.59	243.983	20.4862	11.56	0.04071	12.66	0.00605	5.162	0.41	165.344	5.162	0.04881	11.56	0	139	272	41	5	**38.9**	**2.0**
SMIg45 M 94	5/16/201	164	76	-0.4	0.46	81.8665	12.4646	18.68	0.06659	20.75	0.00602	9.037	0.44	166.125	9.037	0.08023	18.68	-1.6833E-16	1203	368	65	13	**38.7**	**3.5**
SMIg45 M 98	5/16/201	438	540	3.59	1.23	190.558	20.5651	8.07	0.04026	9.511	0.006	5.033	0.53	166.534	5.033	0.04863	8.07	-1.7495E-16	130	190	40	4	**38.6**	**1.9**
SMIg45 M 93	5/16/201	397	198	-4	0.50	52.4362	21.3658	10.55	0.03861	13.63	0.00598	8.625	0.63	167.136	8.625	0.0468	10.55	0	39	252	38	5	**38.5**	**3.3**
SMIg45 M 97	5/16/201	446	555	4.38	1.25	255.326	22.1068	9.57	0.03724	10.66	0.00597	4.702	0.44	167.479	4.702	0.04523	9.57	0	-43	233	37	4	**38.4**	**1.8**
SMIg45 M 110	5/16/20	139	101	-0.8	0.72	20.6676	17.6569	14.39	0.04625	16.19	0.00592	7.424	0.46	168.858	7.424	0.05664	14.39	2.66048E-16	477	318	46	7	**38.1**	**2.8**
SMIg45 M 100	5/16/20	499	757	3.73	1.52	157.655	22.1894	8.101	0.03642	10.06	0.00586	5.958	0.59	170.597	5.958	0.04507	8.101	2.94422E-16	-52	197	36	4	**37.7**	**2.2**
SMIg45 L 12	5/16/2012	121	101	0.85	0.83	80.7507	27.4403	27.01	0.02945	27.71	0.00586	6.179	0.22	170.64	6.179	0.03644	27.01	3.40586E-16	-598	734	29	8	**37.7**	**2.3**
SMIg45 M 103	5/16/20	484	434	3.9	0.90	589.402	19.8306	11.05	0.04066	11.62	0.00585	3.609	0.31	170.999	3.609	0.05043	11.05	0	215	256	40	5	**37.6**	**1.4**
SMIg45 M 102	5/16/20	263	245	-1.7	0.93	43.2243	18.2166	15.61	0.04405	16.16	0.00582	4.19	0.26	171.822	4.19	0.0549	15.61	4.34677E-16	408	349	44	7	**37.4**	**1.6**
SMIg45 M 109	5/16/20	773	850	4.13	1.10	223.328	22.1047	8.162	0.03608	9.236	0.00578	4.323	0.47	172.87	4.323	0.04524	8.162	0	-43	198	36	3	**37.2**	**1.6**
SMIg45 L 16	5/16/2012	307	167	3.48	0.54	31.0409	19.5496	10.83	0.04079	11.41	0.00578	3.59	0.31	172.905	3.59	0.05115	10.83	-3.6546E-16	248	249	41	5	**37.2**	**1.3**
SMIg45 L 14	5/16/2012	287	140	3.04	0.49	43.9771	20.8959	10.49	0.03795	11.49	0.00575	4.684	0.41	173.849	4.684	0.04786	10.49	-2.8915E-16	92	249	38	4	**37.0**	**1.7**
SMIg45 M 101	5/16/20	263	288	-0	1.09	66.7938	24.0132	17.52	0.03302	18.65	0.00575	6.394	0.34	173.904	6.394	0.04164	17.52	-2.5367E-16	-248	443	33	6	**37.0**	**2.4**
SMIg45 M 106	5/16/20	265	272	1.44	1.03	185.282	22.122	13.07	0.03584	13.92	0.00575	4.806	0.35	173.915	4.806	0.0452	13.07	-2.2629E-16	-45	318	36	5	**37.0**	**1.8**
SMIg45 L 17	5/16/2012	470	273	2.18	0.58	604.994	22.0684	10.08	0.03584	10.61	0.00574	3.32	0.31	174.335	3.32	0.04531	10.08	-4.2474E-16	-39	245	36	4	**36.9**	**1.2**
SMIg45 M 112	5/16/20	156	73.9	0.84	0.47	423.996	40.506	29.43	0.01927	30.1	0.00566	6.314	0.21	176.607	6.314	0.02469	29.43	0	-1804	1052	19	6	**36.4**	**2.3**
SMIg45 M 107	5/16/20	266	214	0.8	0.81	96.4367	24.3713	14.4	0.03198	15.52	0.00565	5.805	0.37	176.897	5.805	0.04103	14.4	1.70042E-16	-286	367	32	5	**36.3**	**2.1**
SMIg45 M 99	5/16/201	144	153	-3.9	1.06	19.5313	21.9357	27.91	0.03538	28.81	0.00563	7.148	0.25	177.645	7.148	0.04559	27.91	-2.8494E-16	-24	676	35	10	**36.2**	**2.6**
SMIg45 M 111	5/16/20	220	121	-0.9	0.55	21.8415	26.9262	20.23	0.02881	21	0.00563	5.648	0.27	177.756	5.648	0.03714	20.23	2.48798E-16	-546	544	29	6	**36.2**	**2.0**
SMIg45 L 11	5/16/2012	814	839	1.85	1.03	6137.11	21.0796	6.506	0.03673	7.205	0.00562	3.098	0.43	178.082	3.098	0.04744	6.506	1.763E-16	71	155	37	3	**36.1**	**1.1**
SMIg45 M 113	5/16/20	212	171	0.85	0.81	104.427	17.328	13.68	0.04321	15.63	0.00543	7.561	0.48	184.152	7.561	0.05771	13.68	0	519	300	43	7	**34.9**	**2.6**
SMIg45 L 13	5/16/2012	342	162	2.65	0.47	67.9362	21.3116	13.64	0.03454	14.46	0.00534	4.799	0.33	187.299	4.799	0.04692	13.64	0	45	326	34	5	34.3	1.6

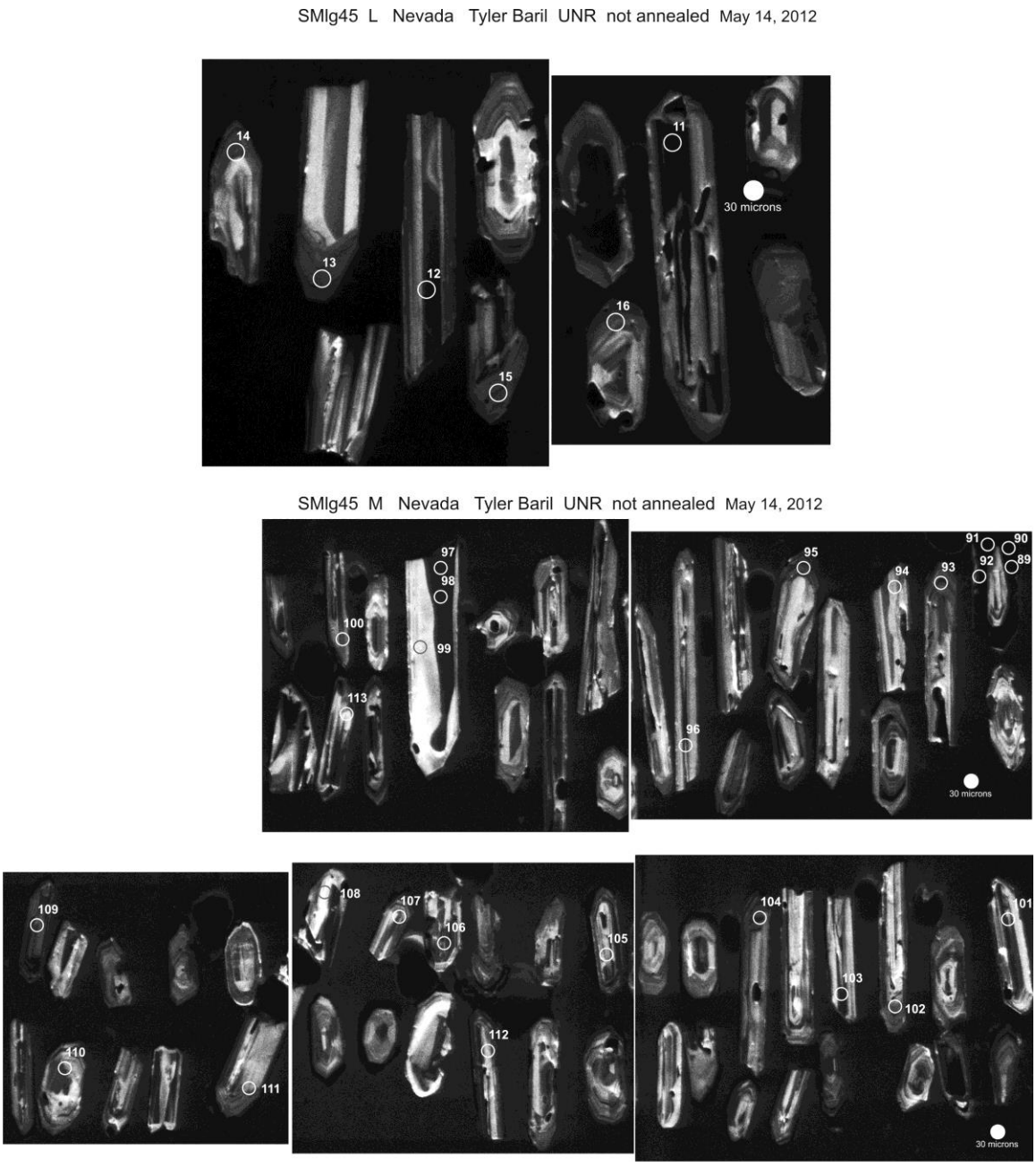

Figure B-3. Cathodeluminescence images of zircons from SMIg45.

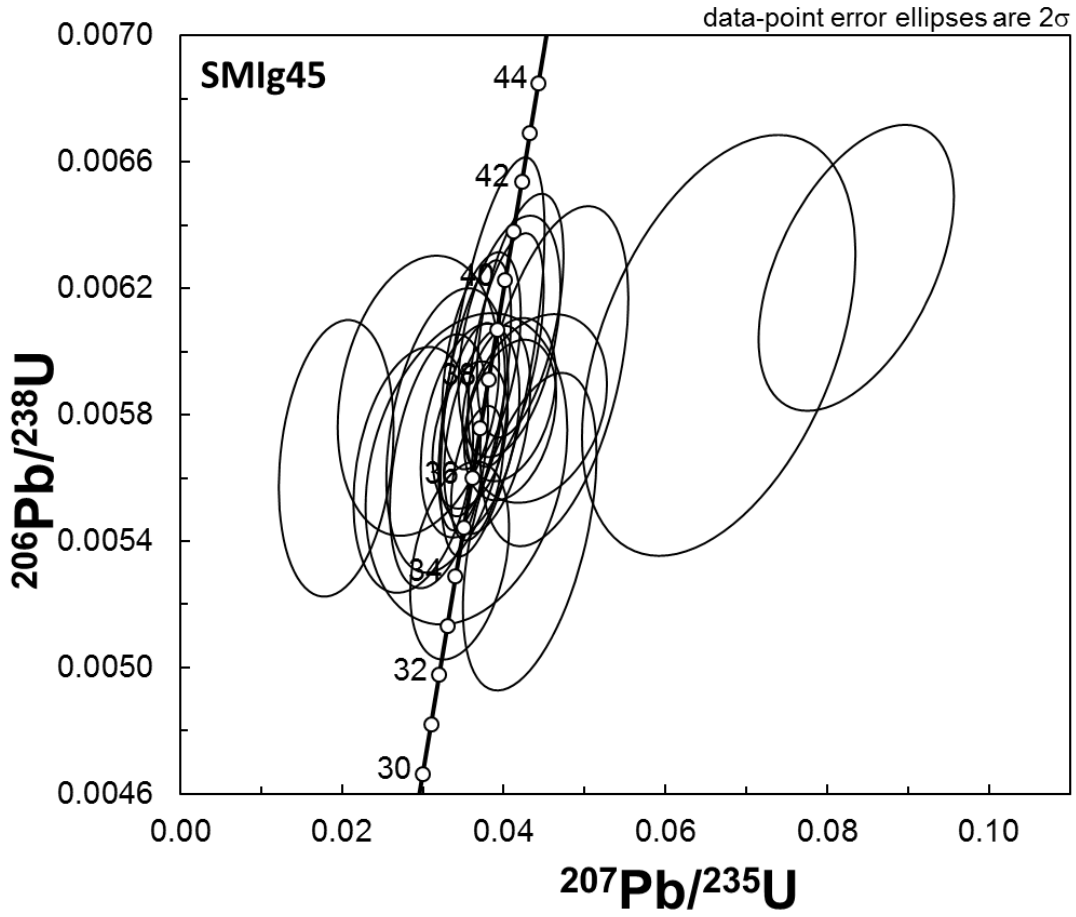

Figure B-4. Concordia plot of zircon ages from SMIg45.

Table B-3. LA-ICP-MS data from sample SMIg46.

Analysis	U ppm	Th ppm	Pb* ppm	Th/U	206Pb 204Pb	206Pb* 207Pb*	±2σ (%)	207Pb* 235U*	±2σ (%)	206Pb* 238U	±2σ (%)	error corr.	238U 206Pb*	±2σ (%)	207Pb* 206Pb*	±2σ (%)	error corr.	207Pb* 206Pb*	±2σ (Ma)	207Pb* 235U	±2σ (Ma)	206Pb* 238U*	±2σ (Ma)
SMIg46																							
SMIg46 M 116 5/16/20	105.66	31.11	54.68	0.29	2340.61	5.2423	1.189	11.0985	6.888	0.42197	6.785	0.98	2.36981	6.785	0.19076	1.189	4.40222E-16	2749	20	2531	64	2269.4	129.8
SMIg46 L 20 5/16/2012	312.93	114.5	52.11	0.37	12053.2	12.9801	2.489	1.91058	5.219	0.17986	4.587	0.88	5.55978	4.587	0.07704	2.489	1.55607E-16	1122	50	1085	35	1066.2	45.1
SMIg46 S 175 5/16/201	413.13	126.3	88.25	0.31	1247.3	13.2422	2.085	1.791	3.703	0.17201	3.061	0.83	5.81361	3.061	0.07552	2.085	-2.7842E-16	1082	42	1042	24	1023.2	29.0
SMIg46 S 169 5/16/201	609.33	237.7	137.2	0.39	2884.55	12.4875	1.867	1.7468	4.719	0.1582	4.334	0.92	6.32092	4.334	0.08008	1.867	0	1199	37	1026	30	946.8	38.2
SMIg46 S 170 5/16/201	803.78	320.9	132.9	0.40	5926.3	12.8431	2.192	1.19284	6.525	0.11111	6.146	0.94	9.00013	6.146	0.07786	2.192	0	1143	44	797	36	679.2	39.6
SMIg46 S 179 5/16/201	504.41	242.2	41.04	0.48	74.7635	3.57292	10.78	1.79216	13.88	0.04644	8.744	0.63	21.5328	8.744	0.27988	10.78	-3.0137E-16	3362	168	1043	90	292.6	25.0
SMIg46 S 177 5/16/201	6426.1	1E+06	28631	170.03	130.529	8.9503	22.68	0.60297	30.24	0.03914	20	0.66	25.5487	20	0.11173	22.68	0	1828	411	479	115	247.5	48.6
SMIg46 S 176 5/16/201	21388	4E+06	99800	188.16	124.348	7.97298	15.77	0.5863	20.73	0.0339	13.45	0.65	29.4958	13.45	0.12542	15.77	1.33954E-16	2035	279	469	78	214.9	28.4
SMIg46 S 168 5/16/201	622.97	165.1	18.31	0.26	243.04	10.8345	24.47	0.37988	25.32	0.02985	6.487	0.26	33.5	6.487	0.0923	24.47	3.58074E-16	1473	464	327	71	***189.6***	***12.1***
SMIg46 S 178 5/16/201	20096	4E+06	1E+05	193.77	295.136	12.0193	10.18	0.33623	16.62	0.02931	13.14	0.79	34.1183	13.14	0.0832	10.18	-2.1244E-16	1274	199	294	42	***186.2***	***24.1***
SMIg46 M 115 5/16/20	634.43	188.5	17.86	0.30	274.828	10.4291	15.94	0.38213	19.34	0.0289	10.94	0.57	34.5971	10.94	0.09589	15.94	-1.6292E-16	1546	300	329	54	***183.7***	***19.8***
SMIg46 S 171 5/16/201	1234.1	366.7	49.19	0.30	2302.86	17.07	5.999	0.22923	6.993	0.02838	3.595	0.51	35.2375	3.595	0.05858	5.999	0	552	131	210	13	***180.4***	***6.4***
SMIg46 S 172 5/16/201	725.02	312.1	21.24	0.43	225.177	12.2621	19.65	0.31288	19.86	0.02783	2.923	0.15	35.9379	2.923	0.08155	19.65	0	1235	385	276	48	***176.9***	***5.1***
SMIg46 S 173 5/16/201	28619	4E+06	84117	142.05	342.798	15.4461	5.78	0.24192	13.69	0.0271	12.4	0.91	36.8984	12.4	0.06474	5.78	-3.9638E-16	766	122	220	27	***172.4***	***21.1***
SMIg46 M 114 5/16/20	901.86	263.8	23.63	0.29	3554.43	18.9474	4.316	0.18129	6.93	0.02491	5.422	0.78	40.1407	5.422	0.05278	4.316	1.51832E-16	319	98	169	11	**158.6**	**8.5**
SMIg46 L 18 5/16/2012	460.44	676.4	3.899	1.47	438.004	19.6995	3.318	0.169	5.441	0.02415	4.312	0.79	41.4148	4.312	0.05076	3.318	-2.4829E-16	230	77	159	8	**153.8**	**6.6**
SMIg46 L 19 5/16/2012	442.27	479.9	5.868	1.08	489.128	19.6049	6.021	0.16735	8.363	0.02379	5.805	0.69	42.0258	5.805	0.05101	6.021	2.03306E-16	241	139	157	12	**151.6**	**8.7**

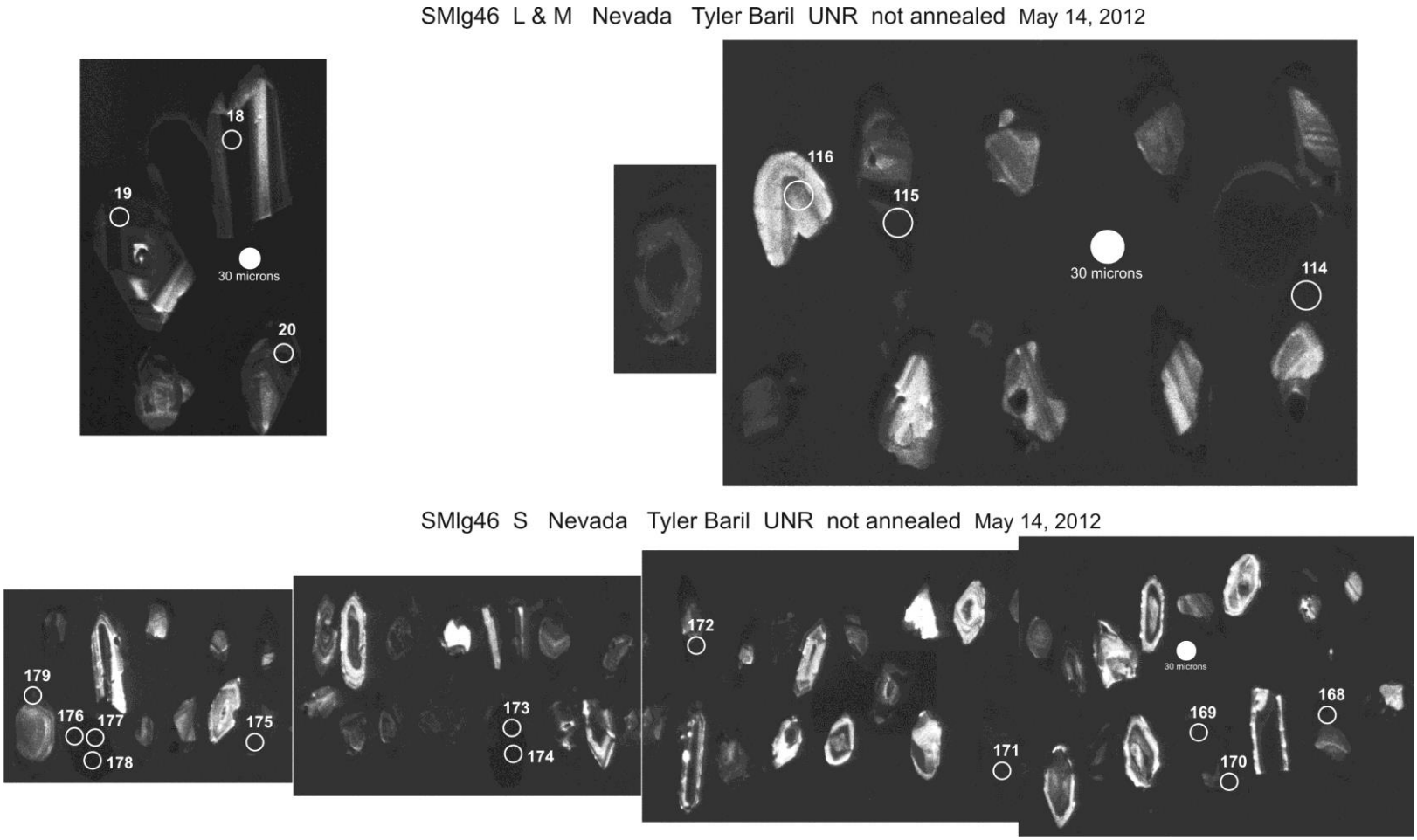

Figure B-5. Cathodeluminescence images of zircons from SMIg46.

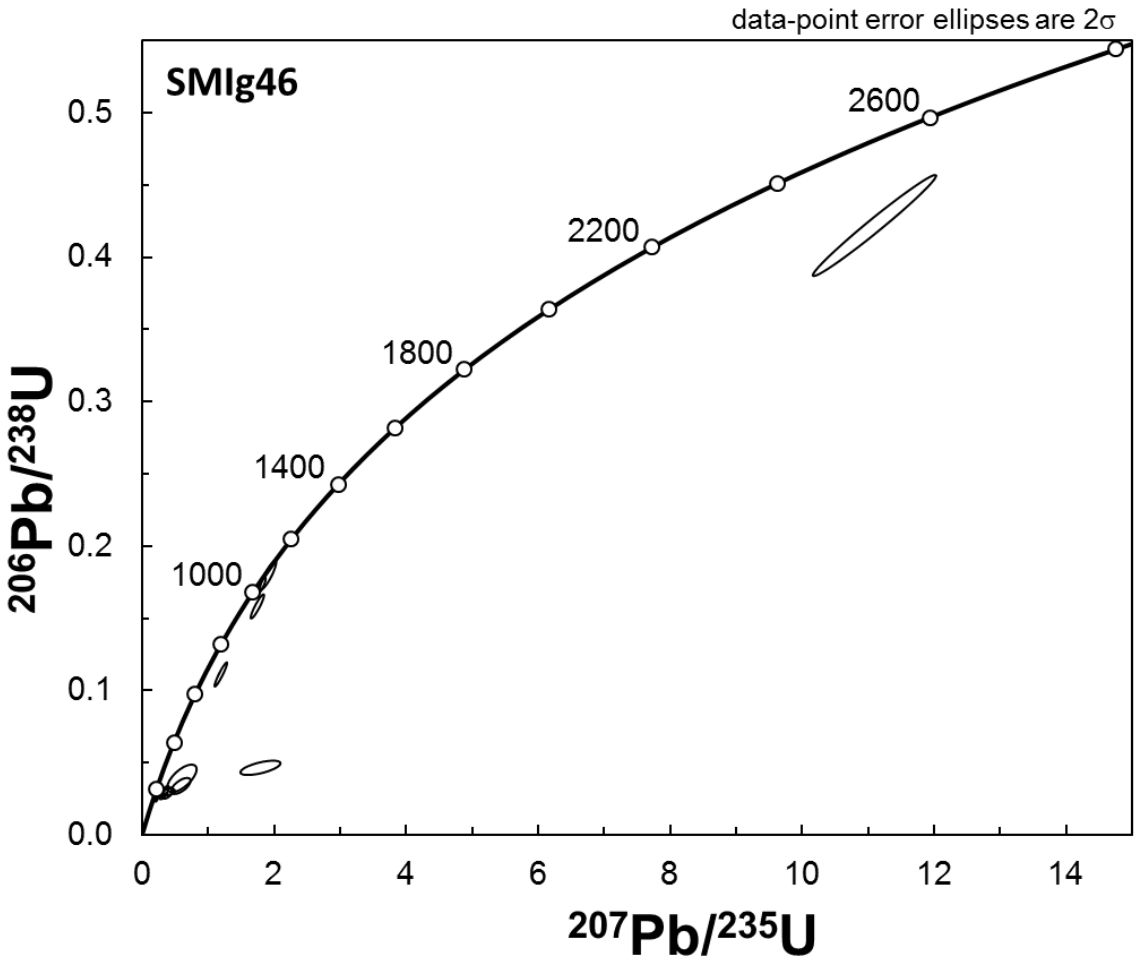

Figure B-6. Concordia plot of zircon ages from SMIg46.

Table B-4. LA-ICP-MS data from sample SMIg47.

Analysis	U ppm	Th ppm	Pb* ppm	Th/U	206Pb 204Pb	206Pb* 207Pb*	±2σ (%)	207Pb* 235U*	±2σ (%)	206Pb* 238U	±2σ (%)	error corr.	238U 206Pb*	±2σ (%)	207Pb* 206Pb*	±2σ (%)	error corr.	207Pb* 206Pb*	±2σ (Ma)	207Pb* 235U	±2σ (Ma)	206Pb* 238U*	±2σ (Ma)
SMIg47																							
SMIg47 M 139 5/16/20	561.98	258.4	13.5	0.46	7064.82	20.1177	2.996	0.18133	6.422	0.02646	5.68	0.88	37.7959	5.68	0.04971	2.996	0	181	70	169	10	168.3	9.4
SMIg47 L 22 5/16/2012	315.82	155	7.867	0.49	236.972	20.143	4.648	0.18011	6.111	0.02631	3.966	0.65	38.0047	3.966	0.04964	4.648	0	178	108	168	9	167.4	6.6
SMIg47 M 141 5/16/20	384.65	180.8	9.283	0.47	783.081	19.8948	4.622	0.17953	6.696	0.0259	4.845	0.72	38.6031	4.845	0.05026	4.622	0	207	107	168	10	**164.9**	**7.9**
SMIg47 M 134 5/16/20	465.26	194.4	11.3	0.42	607.68	20.2251	6.529	0.17567	8.042	0.02577	4.695	0.58	38.8067	4.695	0.04944	6.529	-2.3179E-16	169	152	164	12	**164.0**	**7.6**
SMIg47 M 142 5/16/20	360.34	173.1	8.547	0.48	458.427	21.4784	5.096	0.16326	7.552	0.02543	5.574	0.74	39.32	5.574	0.04656	5.096	1.25077E-16	27	122	154	11	**161.9**	**8.9**
SMIg47 M 131 5/16/20	515.49	254.1	11.4	0.49	3544.56	20.5262	4.739	0.16989	6.208	0.02529	4.01	0.65	39.5401	4.01	0.04872	4.739	1.86932E-16	134	111	159	9	**161.0**	**6.4**
SMIg47 M 121 5/16/20	230.09	116.5	5.3	0.51	407.896	15.9087	7.306	0.21836	8.28	0.02519	3.896	0.47	39.6909	3.896	0.06286	7.306	0	703	155	201	15	**160.4**	**6.2**
SMIg47 M 129 5/16/20	1486.2	1328	26.62	0.89	10973.4	20.1696	2.958	0.17178	5.007	0.02513	4.039	0.81	39.7952	4.039	0.04958	2.958	-2.9735E-16	175	69	161	7	**160.0**	**6.4**
SMIg47 M 138 5/16/20	549.62	207.9	12.93	0.38	501.144	19.1293	5.264	0.17994	6.982	0.02496	4.586	0.66	40.0576	4.586	0.05228	5.264	-1.4716E-16	297	120	168	11	**159.0**	**7.2**
SMIg47 M 140 5/16/20	493.77	272.2	10.96	0.55	3172.35	20.0318	3.422	0.17137	5.358	0.0249	4.123	0.77	40.1655	4.123	0.04992	3.422	0	191	80	161	8	**158.5**	**6.5**
SMIg47 M 136 5/16/20	679.51	239.1	16.22	0.35	664.657	19.7183	4.055	0.1737	6.167	0.02484	4.647	0.75	40.2564	4.647	0.05071	4.055	0	228	94	163	9	**158.2**	**7.3**
SMIg47 M 135 5/16/20	510.21	198.3	12.25	0.39	331.473	19.8401	3.9	0.17229	5.379	0.02479	3.704	0.69	40.3366	3.704	0.0504	3.9	0	214	90	161	8	**157.9**	**5.8**
SMIg47 M 132 5/16/20	487.55	553.7	7.743	1.14	382.844	18.8063	4.127	0.18084	4.775	0.02467	2.402	0.5	40.5424	2.402	0.05317	4.127	-1.7917E-16	336	94	169	7	**157.1**	**3.7**
SMIg47 L 23 5/16/2012	327.52	259.5	6.812	0.79	299.04	19.58	6.906	0.17291	7.782	0.02455	3.586	0.46	40.7267	3.586	0.05107	6.906	-2.8693E-16	244	159	162	12	**156.4**	**5.5**
SMIg47 M 137 5/16/20	561.45	204.2	13.39	0.36	280.218	20.246	5.213	0.16718	7.129	0.02455	4.863	0.68	40.7354	4.863	0.04939	5.213	-1.4015E-16	166	122	157	10	**156.3**	**7.5**
SMIg47 M 117 5/16/20	572.31	208.1	14	0.36	678.278	19.6246	4.277	0.17226	6.5	0.02452	4.895	0.75	40.7866	4.895	0.05096	4.277	1.69713E-16	239	99	161	10	**156.1**	**7.6**
SMIg47 M 119 5/16/20	644.88	222.9	15.26	0.35	369.766	20.7393	3.664	0.1624	4.99	0.02443	3.387	0.68	40.9379	3.387	0.04822	3.664	0	110	87	153	7	**155.6**	**5.2**
SMIg47 M 128 5/16/20	266.19	145.4	5.573	0.55	3797.19	17.5856	5.091	0.1908	6.666	0.02434	4.304	0.65	41.0925	4.304	0.05686	5.091	-1.6214E-16	486	112	177	11	**155.0**	**6.6**
SMIg47 L 21 5/16/2012	350.85	149.1	8.052	0.42	279.838	20.7315	5.987	0.1602	7.522	0.02409	4.554	0.61	41.5156	4.554	0.04824	5.987	1.30306E-16	111	141	151	11	**153.4**	**6.9**
SMIg47 M 126 5/16/20	537.85	204.9	12.08	0.38	1051.72	18.5894	5.238	0.17852	6.724	0.02407	4.215	0.63	41.5487	4.215	0.05379	5.238	-1.6091E-16	362	118	167	10	**153.3**	**6.4**
SMIg47 M 122 5/16/20	127.26	70.46	2.732	0.55	410.807	20.6648	8.271	0.16006	9.111	0.02399	3.821	0.42	41.6856	3.821	0.04839	8.271	2.24825E-16	118	195	151	13	**152.8**	**5.8**
SMIg47 M 125 5/16/20	223.04	134.1	4.65	0.60	216.67	20.4238	6.072	0.16156	7.99	0.02393	5.193	0.65	41.7861	5.193	0.04896	6.072	1.12661E-16	146	142	152	11	**152.5**	**7.8**
SMIg47 M 120 5/16/20	633.37	251.7	14.55	0.40	1491.67	19.8786	3.798	0.16465	5.972	0.02374	4.608	0.77	42.1266	4.608	0.05031	3.798	-2.0298E-16	209	88	155	9	**151.2**	**6.9**
SMIg47 M 143 5/16/20	451.66	335.6	9.178	0.74	313.914	20.1682	5.6	0.16007	7.772	0.02341	5.39	0.69	42.7106	5.39	0.04958	5.6	1.17704E-16	175	131	151	11	**149.2**	**7.9**
SMIg47 M 118 5/16/20	150.53	133.8	3.081	0.89	430.547	19.6132	7.542	0.16453	8.994	0.0234	4.901	0.54	42.7282	4.901	0.05099	7.542	1.92242E-16	240	174	155	13	**149.1**	**7.2**
SMIg47 M 144 5/16/20	376.72	467.7	6.482	1.24	289.042	20.1455	5.412	0.1595	7.283	0.0233	4.874	0.67	42.9113	4.874	0.04964	5.412	1.34689E-16	178	126	150	10	**148.5**	**7.2**

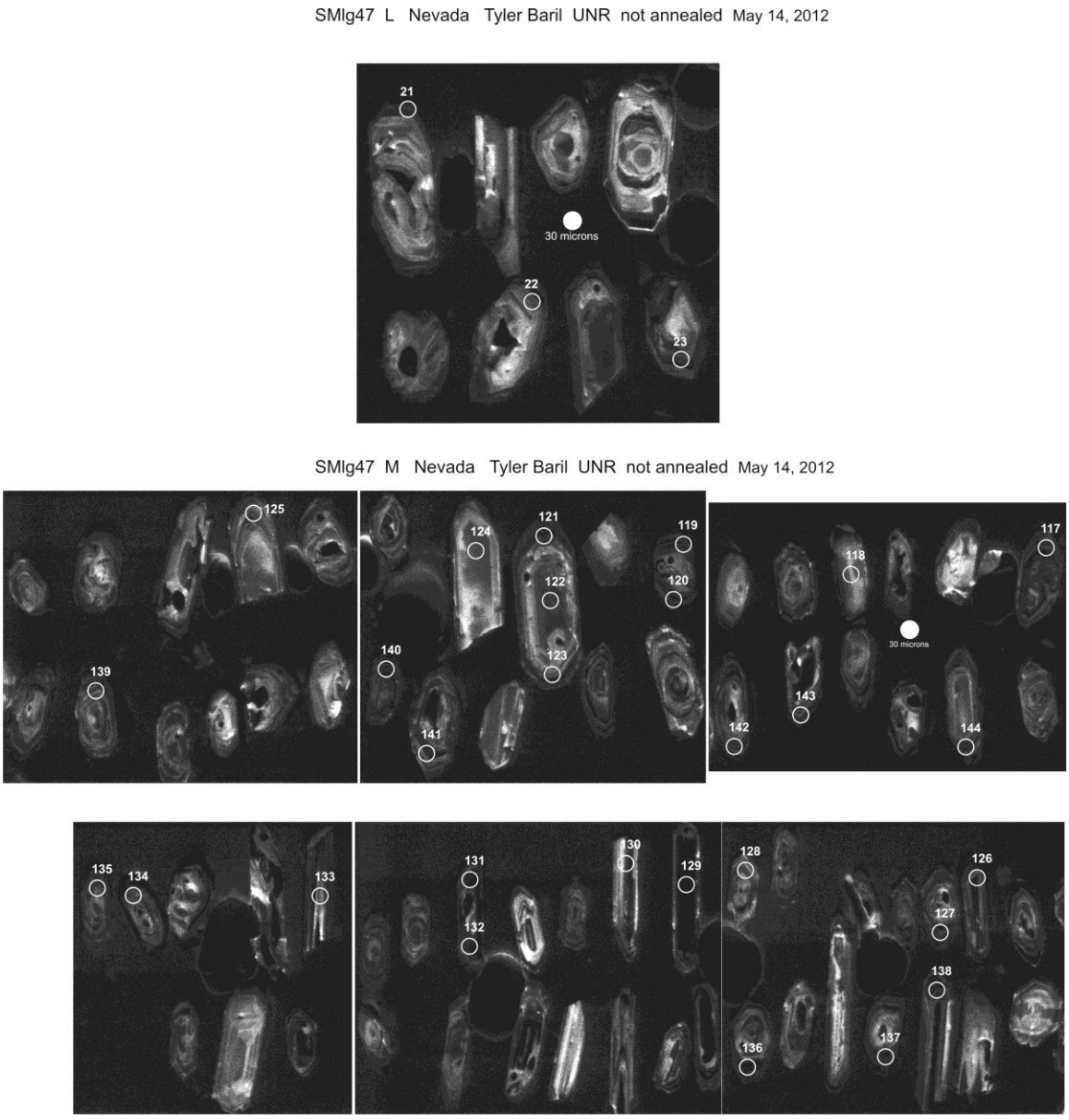

Figure B-7. Cathodeluminescence images of zircons from SMIg47.

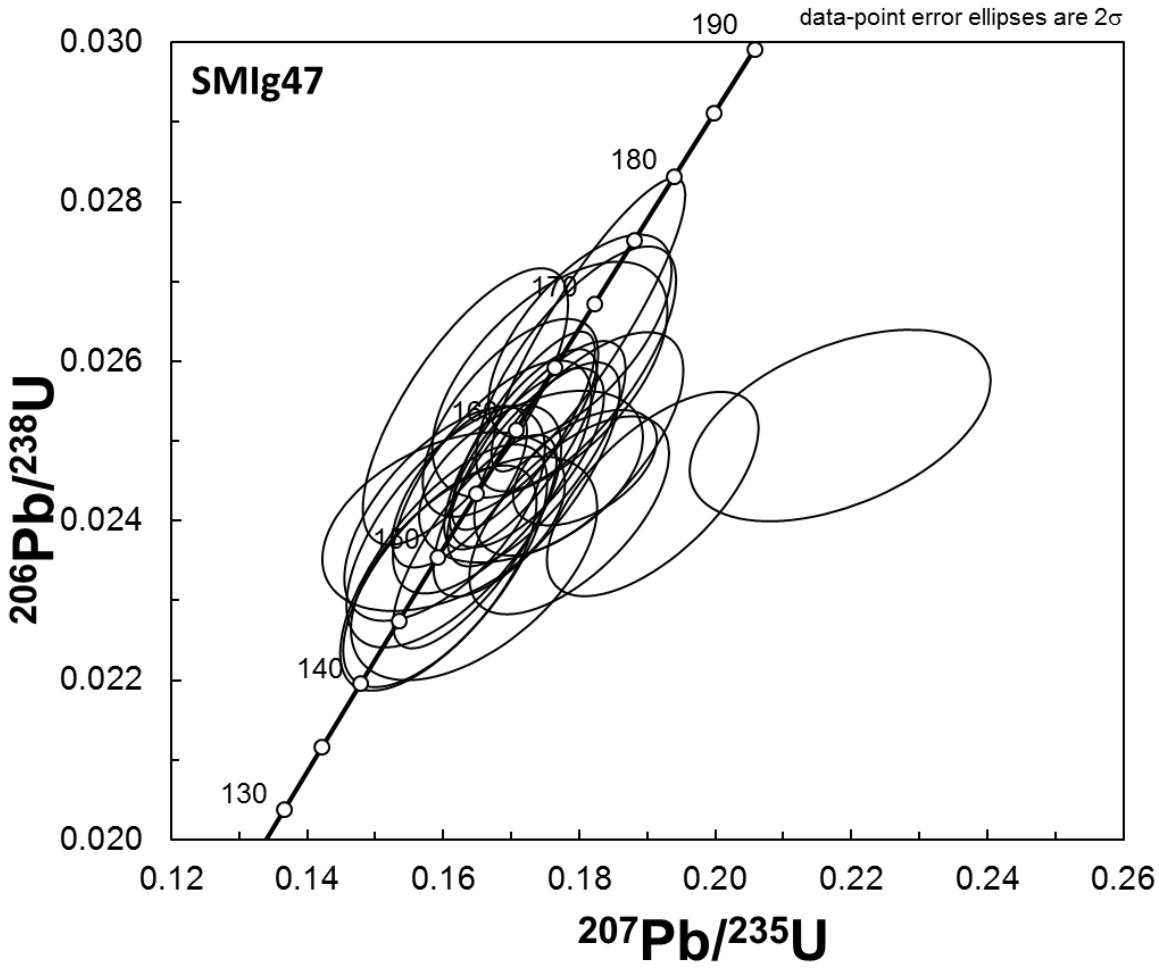

Figure B-8. Concordia plot of zircon ages from SMIg47.

Table B-5. LA-ICP-MS data from sample SMIg49.

Analysis		U ppm	Th ppm	Pb* ppm	Th/U	206Pb 204Pb	206Pb* 207Pb*	±2σ (%)	207Pb* 235U*	±2σ (%)	206Pb* 238U	±2σ (%)	error corr.	238U 206Pb*	±2σ (%)	207Pb* 206Pb*	±2σ (%)	error corr.	207Pb* 206Pb*	±2σ (Ma)	207Pb* 235U	±2σ (Ma)	206Pb* 238U*	±2σ (Ma)
SMIg49																								
SMIg49 L 54	5/16/2012	2216	811.5	16.9	0.37	2599.23	22.2116	5.531	0.0425	11.14	0.00685	9.673	0.87	146.071	9.673	0.04502	5.531	0	-55	135	42	5	44.0	4.2
SMIg49 L 59	5/16/2012	700.2	292.1	5.239	0.42	977.028	22.5973	7.725	0.04146	9.475	0.00679	5.486	0.58	147.183	5.486	0.04425	7.725	0	-97	190	41	4	43.7	2.4
SMIg49 L 41	5/16/2012	1711.9	682.7	11.42	0.40	547.567	20.8539	4.798	0.04399	7.494	0.00665	5.757	0.77	150.299	5.757	0.04795	4.798	1.28638E-16	97	114	44	3	42.7	2.5
SMIg49 L 42	5/16/2012	1591.7	576.5	10.52	0.36	533.037	19.0867	4.16	0.04737	7.667	0.00656	6.44	0.84	152.512	6.44	0.05239	4.16	0	303	95	47	4	42.1	2.7
SMIg49 L 43	5/16/2012	1392.6	482.5	7.962	0.35	174.646	14.524	10.06	0.06213	11.42	0.00654	5.418	0.47	152.802	5.418	0.06885	10.06	2.60833E-16	894	208	61	7	42.1	2.3
SMIg49 L 58	5/16/2012	668.52	365.1	3.394	0.55	164.153	21.2037	9.308	0.04144	10.67	0.00637	5.22	0.49	156.913	5.22	0.04716	9.308	0	57	222	41	4	**41.0**	**2.1**
SMIg49 L 60	5/16/2012	1645.9	663	11.47	0.40	828.191	21.3209	6.882	0.0412	12.13	0.00637	9.987	0.82	156.963	9.987	0.0469	6.882	-2.0674E-16	44	165	41	5	**40.9**	**4.1**
SMIg49 L 65	5/16/2012	820.24	218.6	5.867	0.27	2653.71	22.5808	6.999	0.03888	8.288	0.00637	4.439	0.54	157.034	4.439	0.04429	6.999	-2.2871E-16	-95	172	39	3	**40.9**	**1.8**
SMIg49 L 64	5/16/2012	2570	928.4	17.81	0.36	896.47	21.4329	3.934	0.04073	5.848	0.00633	4.326	0.74	157.935	4.326	0.04666	3.934	2.08723E-16	32	94	41	2	**40.7**	**1.8**
SMIg49 L 46	5/16/2012	3013.3	911.2	20.45	0.30	2522.93	21.7367	4.252	0.04015	6.943	0.00633	5.489	0.79	157.972	5.489	0.04601	4.252	-1.5223E-16	-2	103	40	3	**40.7**	**2.2**
SMIg49 L 44	5/16/2012	1011.3	520.9	6.919	0.52	2775.02	20.6136	6.899	0.0423	9.36	0.00632	6.326	0.68	158.134	6.326	0.04851	6.899	0	124	162	42	4	**40.6**	**2.6**
SMIg49 L 53	5/16/2012	3530.1	1133	24.56	0.32	1974.74	21.042	4.983	0.04138	8.147	0.00631	6.445	0.79	158.367	6.445	0.04752	4.983	-4.4251E-16	76	118	41	3	**40.6**	**2.6**
SMIg49 L 56	5/16/2012	3278.4	1225	23.86	0.37	13910.4	20.9326	3.703	0.04156	6.311	0.00631	5.11	0.81	158.506	5.11	0.04777	3.703	-1.8775E-16	88	88	41	3	**40.5**	**2.1**
SMIg49 L 47	5/16/2012	2016.5	810.4	12.59	0.40	432.991	21.21	4.882	0.04085	7.487	0.00628	5.677	0.76	159.139	5.677	0.04715	4.882	1.28194E-16	57	116	41	3	**40.4**	**2.3**
SMIg49 L 35	5/16/2012	443.27	186.1	2.432	0.42	561.307	16.5652	21.02	0.05217	23.43	0.00627	10.35	0.44	159.548	10.35	0.06037	21.02	-2.6144E-16	617	454	52	12	**40.3**	**4.2**
SMIg49 L 55	5/16/2012	4051.8	1425	28.58	0.35	3840.57	21.2969	4.197	0.04052	7.287	0.00626	5.957	0.82	159.797	5.957	0.04696	4.197	1.42093E-16	47	100	40	3	**40.2**	**2.4**
SMIg49 L 49	5/16/2012	4040	1579	27.72	0.39	3739.65	22.3032	5.591	0.03866	8.592	0.00625	6.525	0.76	159.913	6.525	0.04484	5.591	3.89578E-16	-65	136	39	3	**40.2**	**2.6**
SMIg49 L 51	5/16/2012	3717.7	1472	26.11	0.40	5176.92	20.8297	4.501	0.0412	6.283	0.00622	4.383	0.7	160.677	4.383	0.04801	4.501	0.0000E+00	100	106	41	3	**40.0**	**1.7**
SMIg49 L 62	5/16/2012	3463	1606	25.07	0.46	1875.4	20.956	5.606	0.04057	9.898	0.00617	8.157	0.82	162.176	8.157	0.04772	5.606	-3.1077E-16	85	133	40	4	**39.6**	**3.2**
SMIg49 L 52	5/16/2012	3904.7	1803	26.33	0.46	1021.87	20.3813	3.833	0.04148	7.157	0.00613	6.044	0.84	163.087	6.044	0.04906	3.833	0.0000E+00	151	90	41	3	**39.4**	**2.4**
SMIg49 L 45	5/16/2012	2931.1	919.7	18.75	0.31	1060.38	20.6835	4.472	0.0407	6.75	0.00611	5.056	0.75	163.769	5.056	0.04835	4.472	1.5712E-16	116	105	41	3	**39.2**	**2.0**
SMIg49 L 38	5/16/2012	1718.4	829.6	10.39	0.48	966.872	21.4754	3.951	0.03881	6.006	0.00604	4.524	0.75	165.445	4.524	0.04656	3.951	-1.9879E-16	27	95	39	2	**38.8**	**1.8**
SMIg49 L 37	5/16/2012	1353.5	363.5	7.993	0.27	369.676	21.0219	5.399	0.03958	8.095	0.00603	6.031	0.75	165.726	6.031	0.04757	5.399	-2.1822E-16	78	128	39	3	**38.8**	**2.3**
SMIg49 L 40	5/16/2012	1250.3	773.8	7.692	0.62	2347.63	20.1134	6.352	0.04117	7.821	0.00601	4.562	0.58	166.506	4.562	0.04972	6.352	0.0000E+00	182	148	41	3	**38.6**	**1.8**
SMIg49 L 66	5/16/2012	1458.8	377.2	9.45	0.26	996.417	20.027	6.977	0.0413	8.343	0.006	4.574	0.55	166.69	4.574	0.04993	6.977	4.4528E-16	192	162	41	3	**38.6**	**1.8**
SMIg49 L 61	5/16/2012	3816.3	1566	25.73	0.41	1053.7	21.393	5.988	0.03859	9.281	0.00599	7.091	0.76	167.035	7.091	0.04674	5.988	3.3467E-16	36	143	38	4	**38.5**	**2.7**
SMIg49 L 50	5/16/2012	1155.1	866.6	7.87	0.75	2191.26	20.4505	6.559	0.0399	7.922	0.00592	4.443	0.56	168.982	4.443	0.0489	6.559	-2.4382E-16	143	154	40	3	**38.0**	**1.7**
SMIg49 L 63	5/16/2012	3514	1541	24.26	0.44	1979.51	20.6668	4.536	0.03906	9.832	0.00585	8.724	0.89	170.8	8.724	0.04839	4.536	-3.5914E-16	118	107	39	4	**37.6**	**3.3**
SMIg49 L 57	5/16/2012	2545.2	1170	16.57	0.46	1344.47	21.0461	5.313	0.03758	7.908	0.00574	5.857	0.74	174.34	5.857	0.04751	5.313	0.0000E+00	75	126	37	3	**36.9**	**2.2**
SMIg49 L 36	5/16/2012	590.43	441.7	2.976	0.75	229.984	23.6807	10.52	0.0333	11.96	0.00572	5.688	0.48	174.872	5.688	0.04223	10.52	-2.3754E-16	-213	264	33	4	**36.8**	**2.1**
SMIg49 L 39	5/16/2012	407.22	213	1.349	0.52	52.3168	17.9447	12.46	0.04391	13.35	0.00571	4.807	0.36	175.002	4.807	0.05573	12.46	-2.3731E-16	441	277	44	6	**36.7**	**1.8**
SMIg49 L 48	5/16/2012	996	1185	6.561	1.19	1125.35	20.8967	5.645	0.03752	7.052	0.00569	4.227	0.6	175.872	4.227	0.04785	5.645	2.9781E-16	92	134	37	3	**36.6**	**1.5**

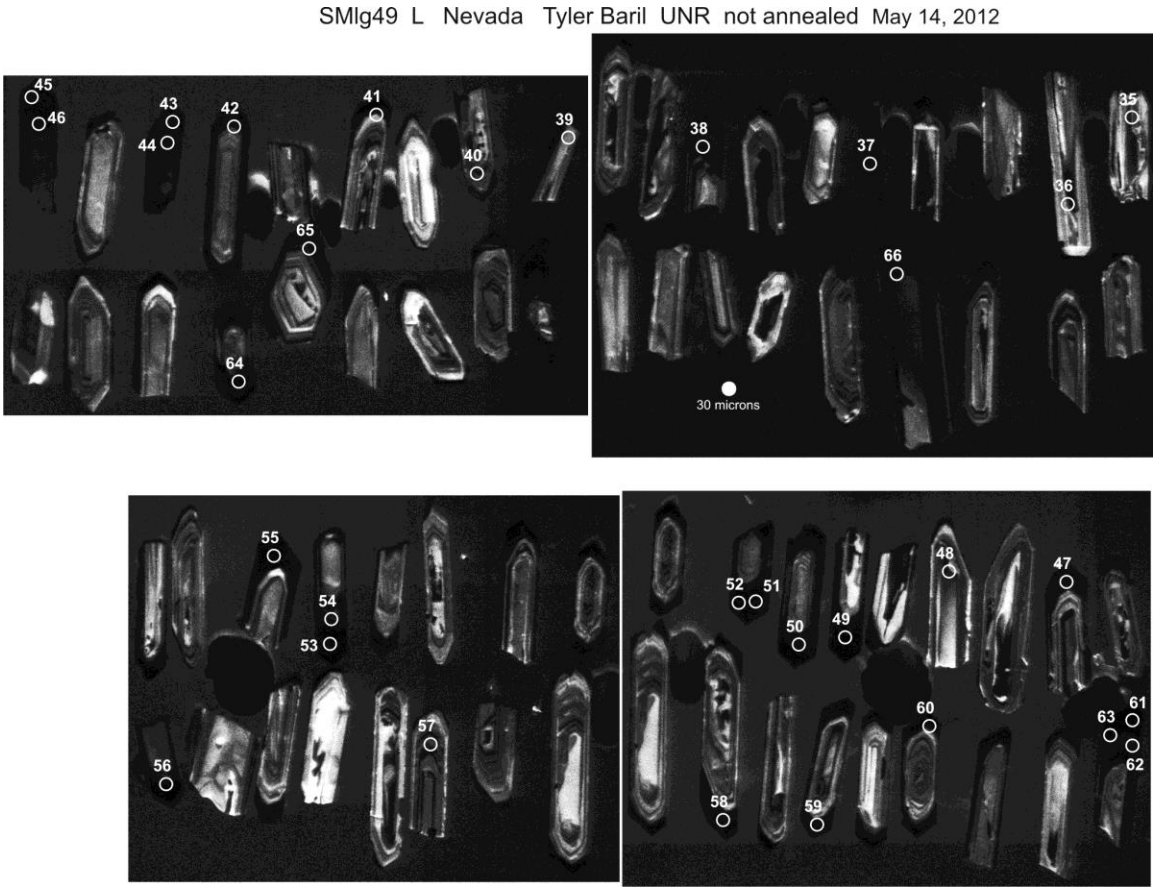

Figure B-9. Cathodeluminescence images of zircons from SMIg49.

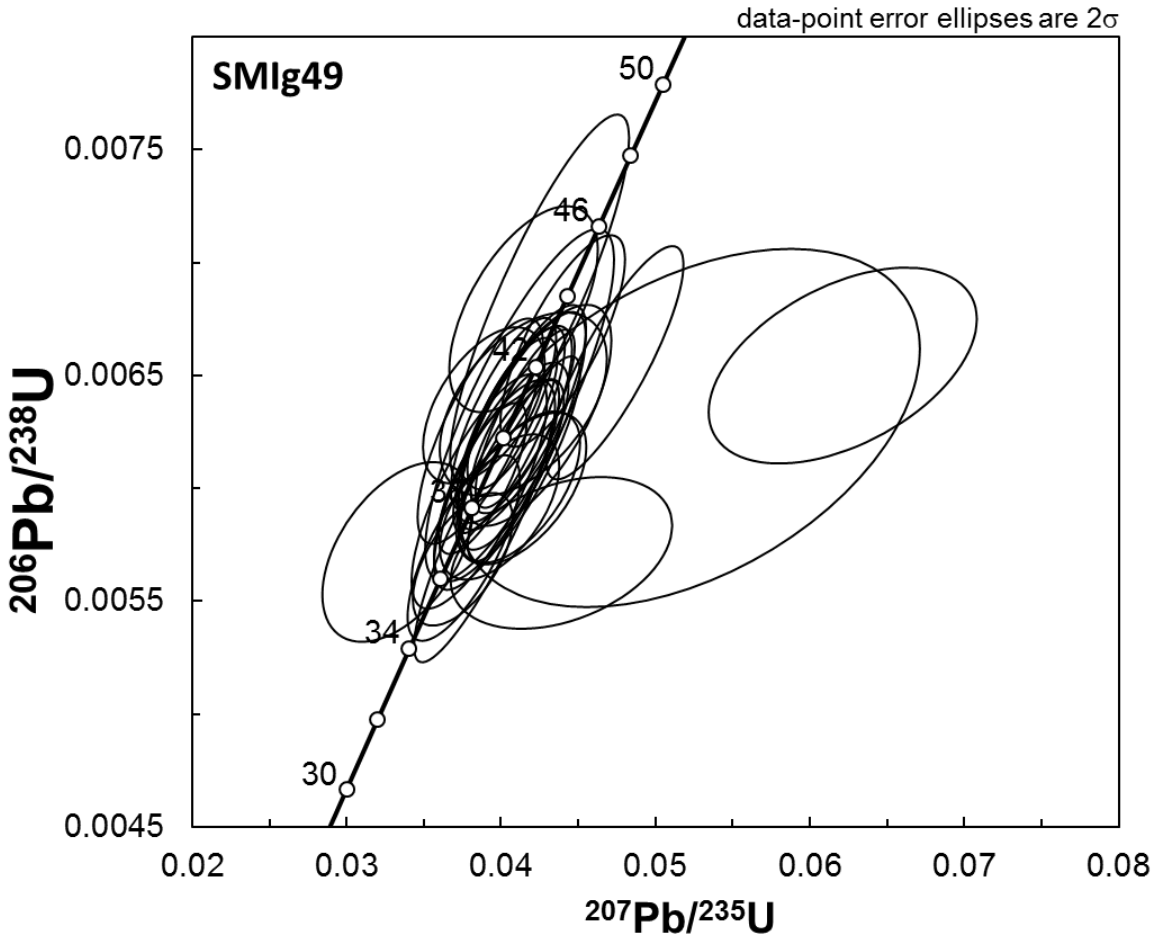

Figure B-10. Concordia plot of zircon ages from SMIg49.

Table B-6. LA-ICP-MS data from sample SMIg51.

Analysis	U ppm	Th ppm	Pb* ppm	Th/U	206Pb 204Pb	206Pb* 207Pb*	±2σ (%)	207Pb* 235U*	±2σ (%)	206Pb* 238U	±2σ (%)	error corr.	238U 206Pb*	±2σ (%)	207Pb* 206Pb*	±2σ (%)	error corr.	207Pb* 206Pb*	±2σ (Ma)	207Pb* 235U	±2σ (Ma)	206Pb* 238U*	±2σ (Ma)
SMIg51																							
SMIg51 M 157 5/16/20	1022.6	971.3	6.112	0.95	147.628	17.7363	11.47	0.05288	13.03	0.0068	6.179	0.47	147.023	6.179	0.05638	11.47	2.0055E-16	467	254	52	7	43.7	2.7
SMIg51 M 145 5/16/20	2115	466.6	14.17	0.22	330.277	20.1222	5.92	0.04641	7.6	0.00677	4.766	0.63	147.648	4.766	0.0497	5.92	2.5182E-16	181	138	46	3	43.5	2.1
SMIg51 L 25 5/16/2012	1578	700.8	9.357	0.44	707.214	21.0468	7.285	0.04159	7.909	0.00635	3.078	0.39	157.533	3.078	0.04751	7.285	0.0000E+00	75	173	41	3	40.8	1.3
SMIg51 M 150 5/16/20	970.67	305.9	5.844	0.32	470.317	21.4725	6.763	0.03899	8.22	0.00607	4.672	0.57	164.699	4.672	0.04657	6.763	2.2488E-16	27	162	39	3	**39.0**	**1.8**
SMIg51 M 154 5/16/20	832.91	222.3	3.503	0.27	123.759	22.552	6.865	0.0371	7.932	0.00607	3.972	0.5	164.815	3.972	0.04434	6.865	1.3028E-16	-92	168	37	3	**39.0**	**1.5**
SMIg51 M 163 5/16/20	12995	3475	82.4	0.27	392.68	15.4625	18.09	0.05382	18.97	0.00604	5.698	0.3	165.683	5.698	0.06467	18.09	0.0000E+00	764	381	53	10	**38.8**	**2.2**
SMIg51 L 29 5/16/2012	11133	2613	66.58	0.23	1658.33	16.6426	3.06	0.04989	4.758	0.00602	3.644	0.77	166.054	3.644	0.06009	3.06	-1.5930E-16	607	66	49	2	**38.7**	**1.4**
SMIg51 L 31 5/16/2012	13183	4348	78.52	0.33	4538.02	21.0538	1.929	0.03908	4.406	0.00597	3.961	0.9	167.588	3.961	0.0475	1.929	4.6483E-16	74	46	39	2	**38.4**	**1.5**
SMIg51 M 167 5/16/20	11347	2674	84.43	0.24	7911.3	21.0822	1.964	0.039	4.651	0.00596	4.216	0.91	167.681	4.216	0.04743	1.964	-2.1458E-16	71	47	39	2	**38.3**	**1.6**
SMIg51 M 153 5/16/20	871.07	423.7	4.648	0.49	222.923	20.7708	6.484	0.03955	8.405	0.00596	5.349	0.64	167.86	5.349	0.04814	6.484	2.0489E-16	106	153	39	3	**38.3**	**2.0**
SMIg51 M 161 5/16/20	950.45	739.5	7.231	0.78	826.514	20.6842	7.3	0.03965	8.159	0.00595	3.645	0.45	168.11	3.645	0.04835	7.3	2.6704E-16	116	172	39	3	**38.2**	**1.4**
SMIg51 M 156 5/16/20	708.08	173.3	2.474	0.24	113.268	21.2232	7.927	0.0385	8.77	0.00593	3.753	0.43	168.732	3.753	0.04712	7.927	-2.3885E-16	55	189	38	3	**38.1**	**1.4**
SMIg51 M 147 5/16/20	9707.1	2318	57.68	0.24	1302.17	19.5374	4.045	0.04144	6.054	0.00587	4.505	0.74	170.289	4.505	0.05118	4.045	0.0000E+00	249	93	41	2	**37.7**	**1.7**
SMIg51 L 27 5/16/2012	11941	2769	69.73	0.23	4277.59	20.1298	2.008	0.04015	3.529	0.00586	2.902	0.82	170.617	2.902	0.04968	2.008	0.0000E+00	180	47	40	1	**37.7**	**1.1**
SMIg51 M 158 5/16/20	11629	2906	77.9	0.25	6622.62	19.0793	7.019	0.04227	7.882	0.00585	3.586	0.45	170.96	3.586	0.05241	7.019	-1.4114E-16	303	160	42	3	**37.6**	**1.3**
SMIg51 M 149 5/16/20	9339.7	2253	55.78	0.24	624.559	15.7183	10.65	0.05112	11.72	0.00583	4.888	0.42	171.611	4.888	0.06362	10.65	0.0000E+00	729	226	51	6	**37.5**	**1.8**
SMIg51 M 155 5/16/20	10166	2061	64.36	0.20	4553.53	21.3645	2.991	0.03749	6.496	0.00581	5.767	0.89	172.143	5.767	0.04681	2.991	0.0000E+00	39	72	37	2	**37.3**	**2.1**
SMIg51 L 32 5/16/2012	10733	3056	62.93	0.28	3252.56	21.3772	2.389	0.0374	4.029	0.0058	3.244	0.81	172.467	3.244	0.04678	2.389	-4.5840E-16	38	57	37	1	**37.3**	**1.2**
SMIg51 M 151 5/16/20	10297	2928	64.13	0.28	57585.8	21.1376	2.701	0.03782	4.044	0.0058	3.009	0.74	172.494	3.009	0.04731	2.701	0.0000E+00	65	64	38	1	**37.3**	**1.1**
SMIg51 L 24 5/16/2012	10354	3189	57.75	0.31	5803.39	20.884	2.961	0.03826	4.51	0.0058	3.401	0.75	172.541	3.401	0.04788	2.961	0.0000E+00	93	70	38	2	**37.3**	**1.3**
SMIg51 M 159 5/16/20	12142	3151	80.12	0.26	2412.22	19.6796	3.684	0.04043	5.251	0.00577	3.741	0.71	173.284	3.741	0.05081	3.684	1.2888E-16	232	85	40	2	**37.1**	**1.4**
SMIg51 M 162 5/16/20	7507.6	2213	48.76	0.29	935.332	20.6172	2.455	0.03851	3.451	0.00576	2.425	0.7	173.652	2.425	0.0485	2.455	1.4917E-16	124	58	38	1	**37.0**	**0.9**
SMIg51 L 28 5/16/2012	12896	4271	71.24	0.33	2430.75	19.4333	4.147	0.0405	6.466	0.00571	4.961	0.77	175.195	4.961	0.05146	4.147	1.7268E-16	261	95	40	3	**36.7**	**1.8**
SMIg51 M 164 5/16/20	13068	4011	88.65	0.31	1047.27	19.6524	4.324	0.04001	5.414	0.0057	3.258	0.6	175.358	3.258	0.05088	4.324	-1.2610E-16	236	100	40	2	**36.7**	**1.2**
SMIg51 L 30 5/16/2012	11406	2663	64.49	0.23	2194.87	20.3947	2.624	0.03799	4.717	0.00562	3.92	0.83	177.973	3.92	0.04903	2.624	1.7271E-16	149	61	38	2	**36.1**	**1.4**
SMIg51 M 166 5/16/20	12151	2668	82.7	0.22	2493.58	19.7546	2.888	0.03913	3.972	0.00561	2.727	0.69	178.356	2.727	0.05062	2.888	1.1279E-16	224	67	39	2	**36.0**	**1.0**

Figure B-11. Cathodeluminescence images of zircons from SMIg51.

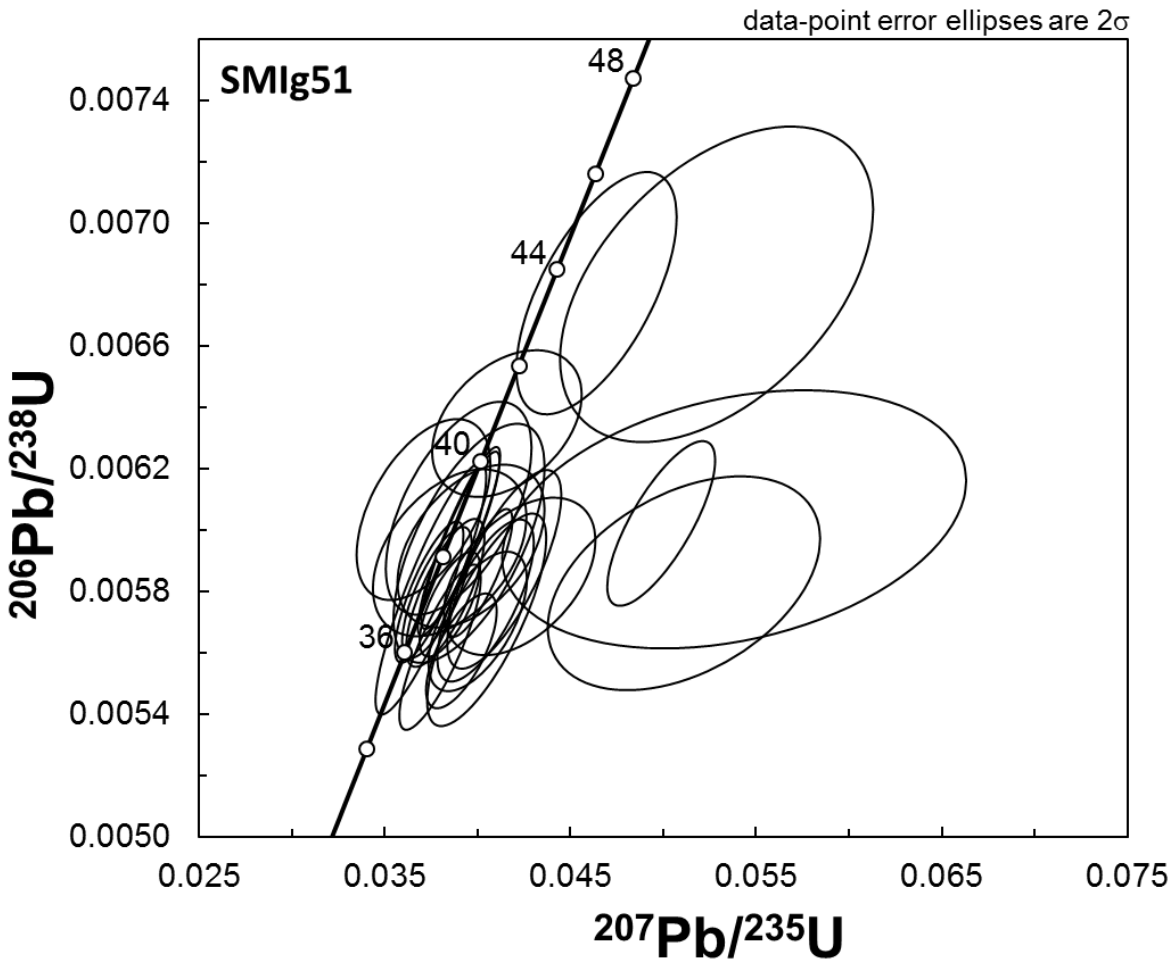

Figure B-12. Concordia plot of zircon ages from SMIg51.

Appendix C – Re-Os Dating Methodology and Data

Approximately 50mg of molybdenite were dissolved and homogenized using the Carius tube technique. Osmium was separated using CCl_4 solvent extraction and rhenium through standard anion exchange columns. Molybdenite samples were analyzed by ID-NTIMS (Isotope Dilution Negative Thermal Ionization Mass Spectrometry) using a VG Sector 54 at the University of Arizona. Ages were calculated using the equation $[^{187}Os]_{today} = [^{187}Re]_{today} (e^{\lambda t}-1)$ with a decay constant (λ) of $1.666 \times 10^{-11} a^{-1}$.

Table C-1. Re-Os data from SMIg49

Sample	Total Re (ppm)	^{187}Re (ppm)	Radiogenic Os (^{187}Os, ppb)	Age (Ma)	Error ±0.5% (Ma)
SMIg49	8.61	5.41	3.73	41.34	0.21

Appendix D – Petrographic Descriptions

SMIg41

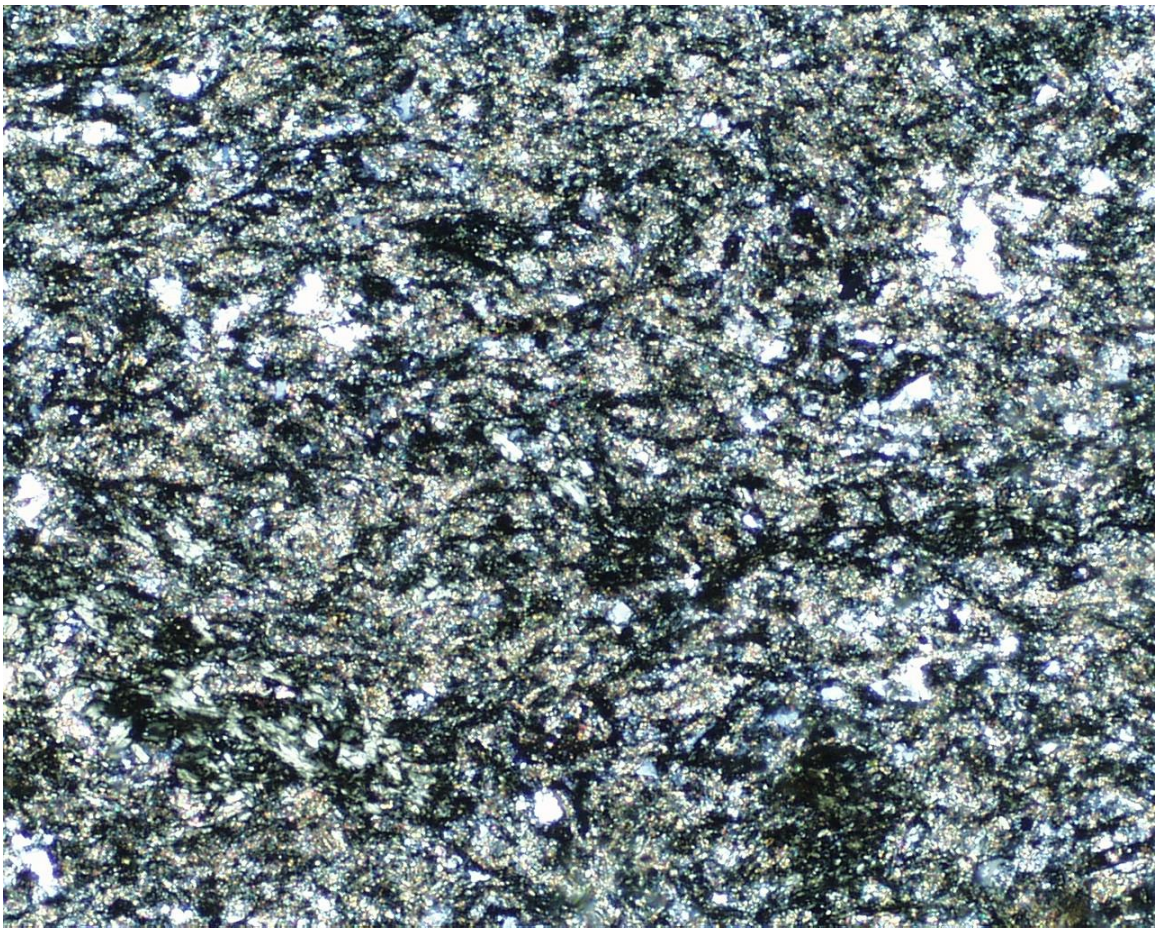

Figure D-1. Fine-grained andesite dike showing complete alteration of primary mineralogy to chlorite and calcite. Cross-polarized light, field of view = 1.7 mm.

SMIg42

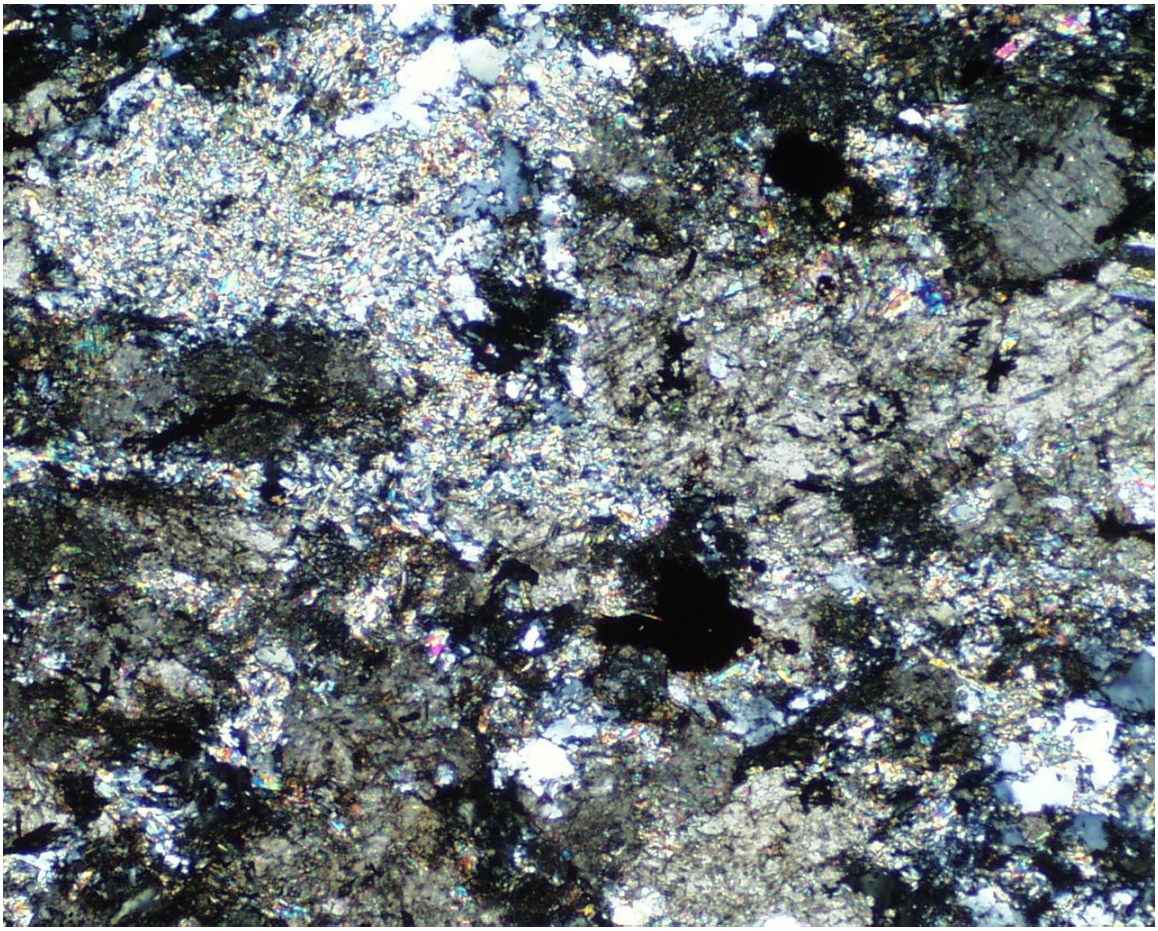

Figure D-2. Fine-grained andesite dike with intense calcite, sericite, and pyrite replacement of primary mineralogy. Cross-polarized light, field of view = 1.7 mm.

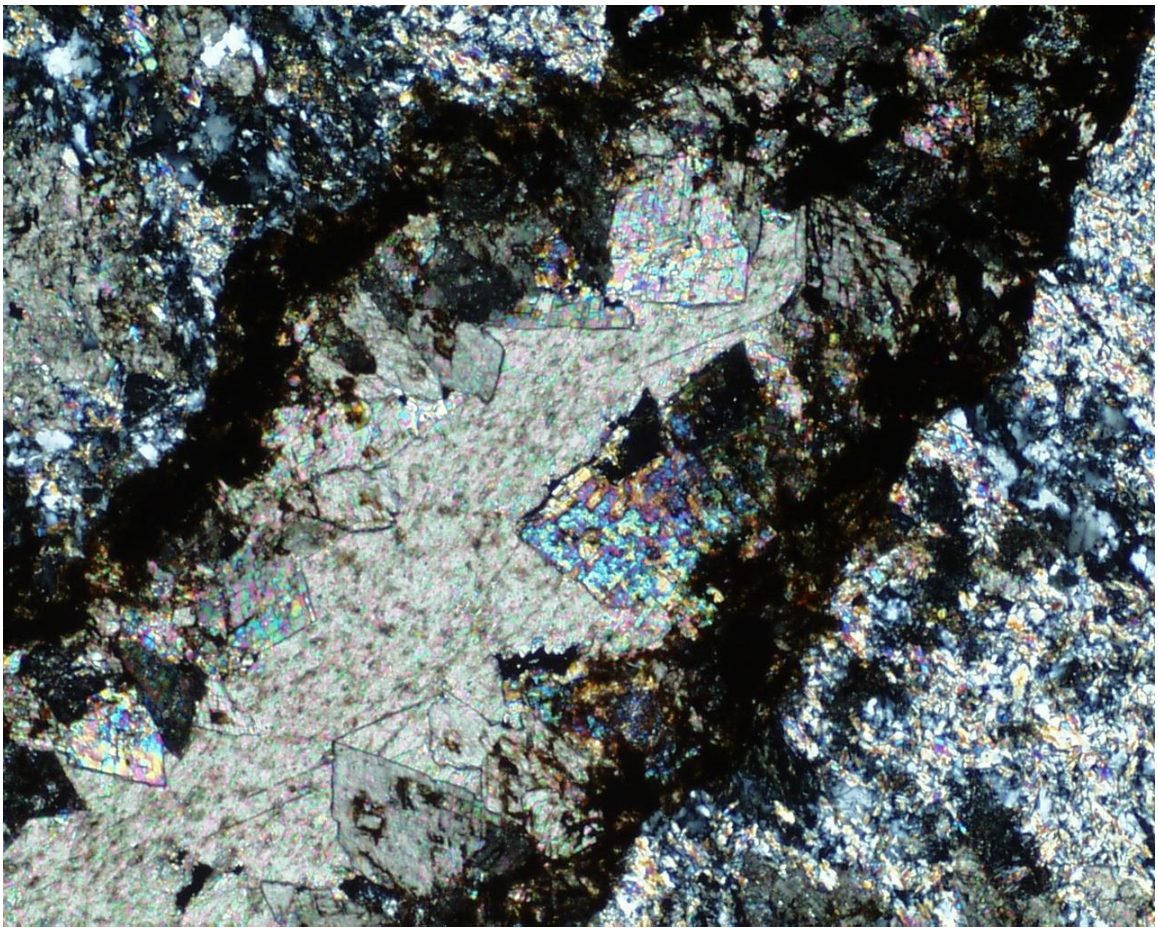

Figure D-3. 1 mm wide calcite vein with iron oxide selvage. Calcite and sericite alteration visible outboard of vein. Cross-polarized light, field of view = 1.7 mm.

SMIg43

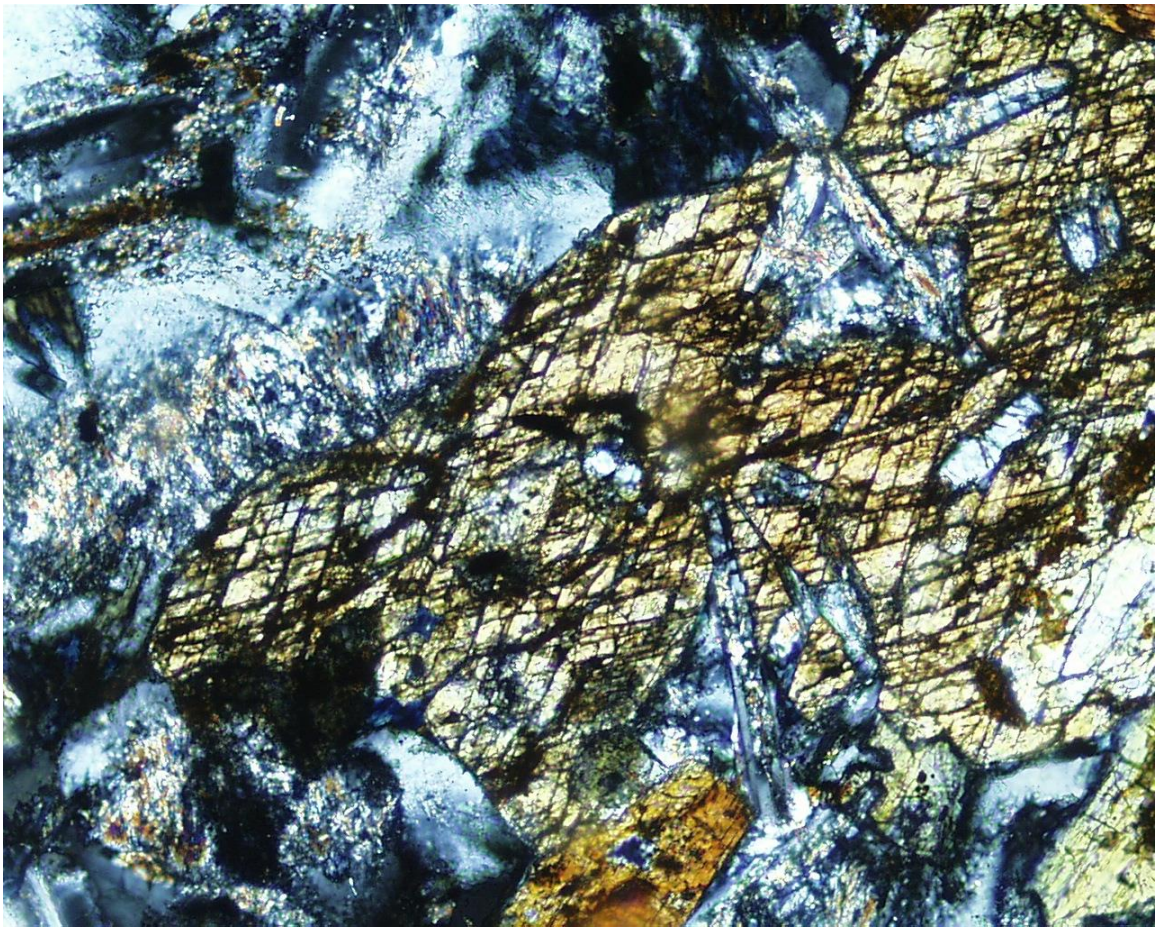

Figure D-4. Fine-grained andesite dike composed of amphibole and plagioclase. Amphibole is fresh to weakly altered by chlorite while plagioclase is weakly altered by sericite. Cross-polarized light, field of view = 0.85 mm.

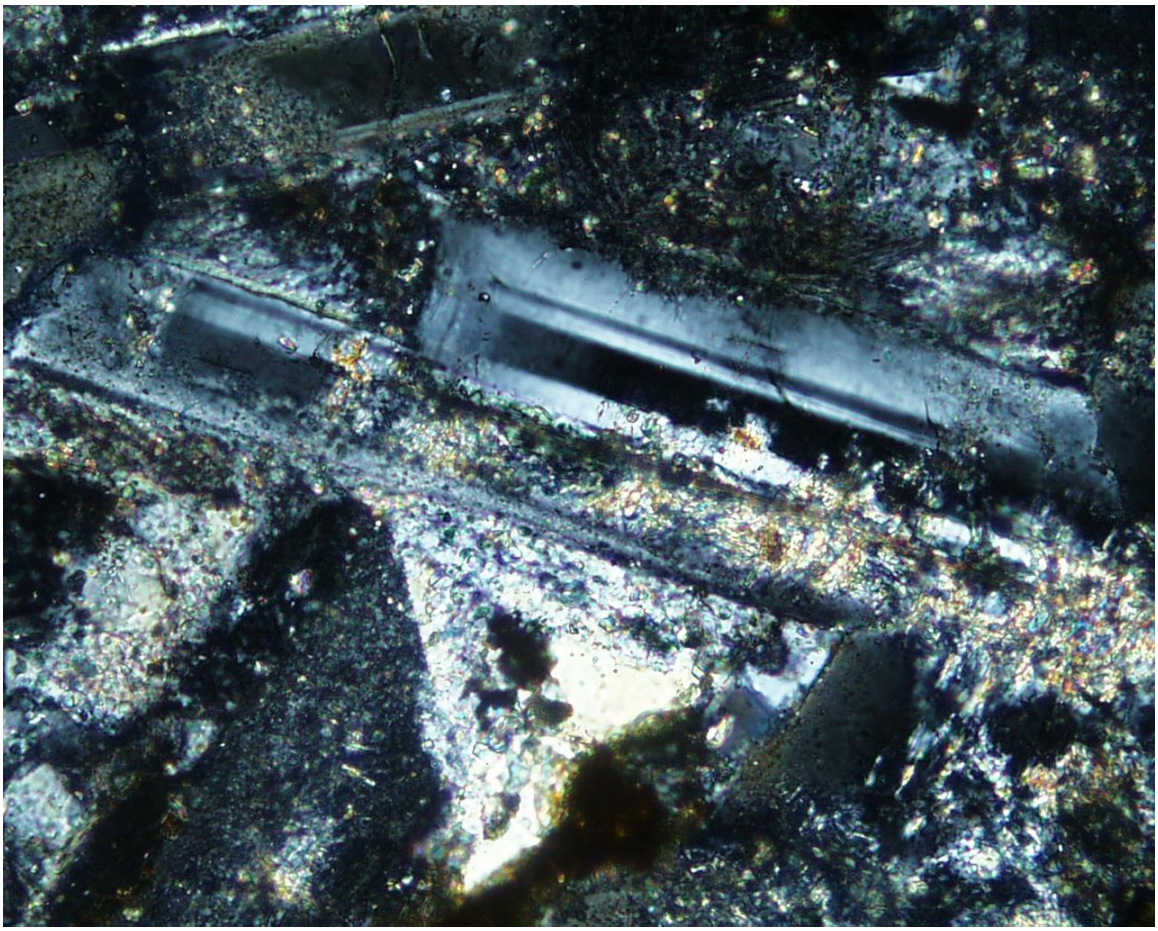

Figure D-5. Plagioclase grains with weak sericite alteration in fine-grained andesite dike. Cross-polarized light, field of view = 0.85 mm.

SMIg44

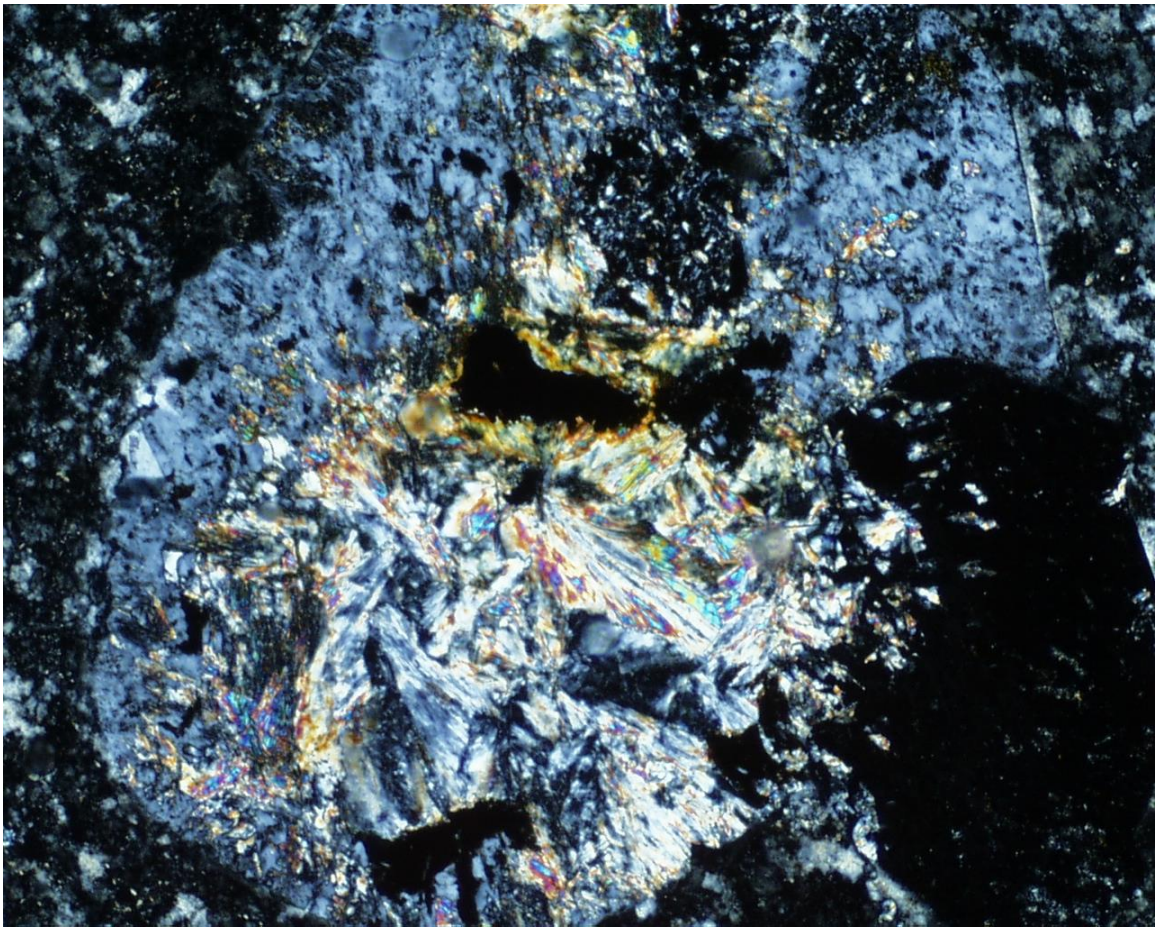

Figure D-6. Potassium feldspar grain with partial replacement by sericite in banded rhyolite dike. Cross-polarized light, field of view = 1.7 mm.

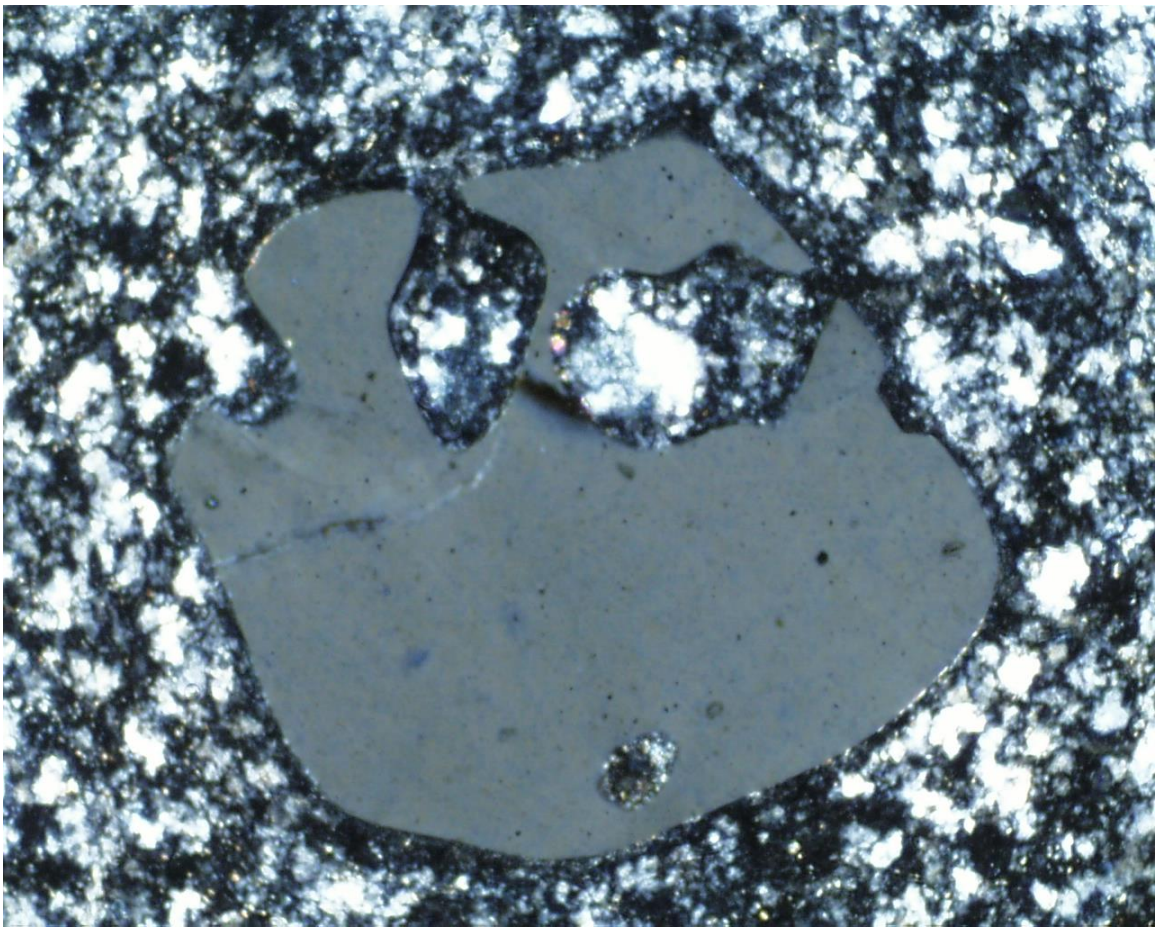

Figure D-7. Resorbed quartz grain in fine-grained matrix of quartz and feldspar. Cross-polarized light, field of view = 1.7 mm.

SMIg45

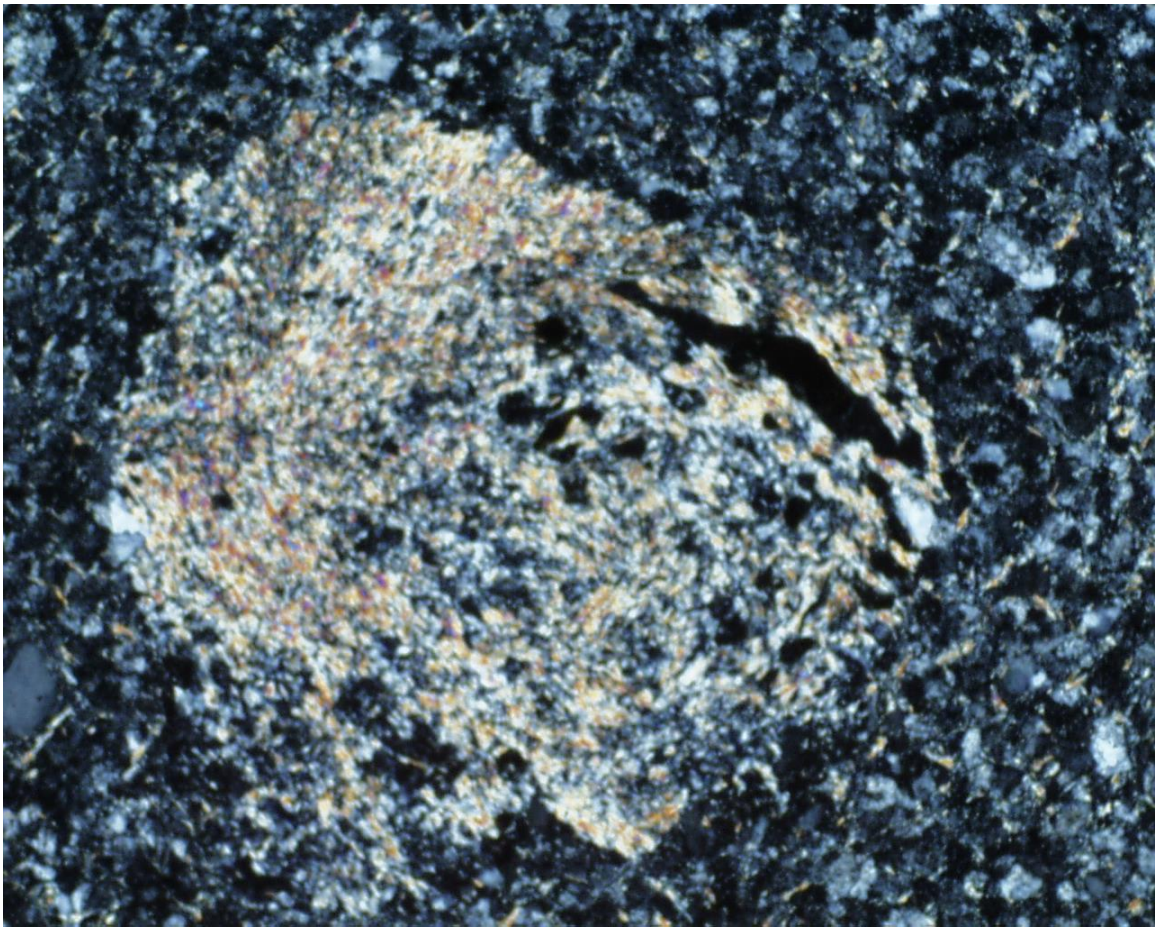

Figure D-8. Sprucemont porphyry with primary feldspar completely replaced by smectite and kaolinite. Groundmass is quartz and feldspar. Cross-polarized light, field of view = 1.7 mm.

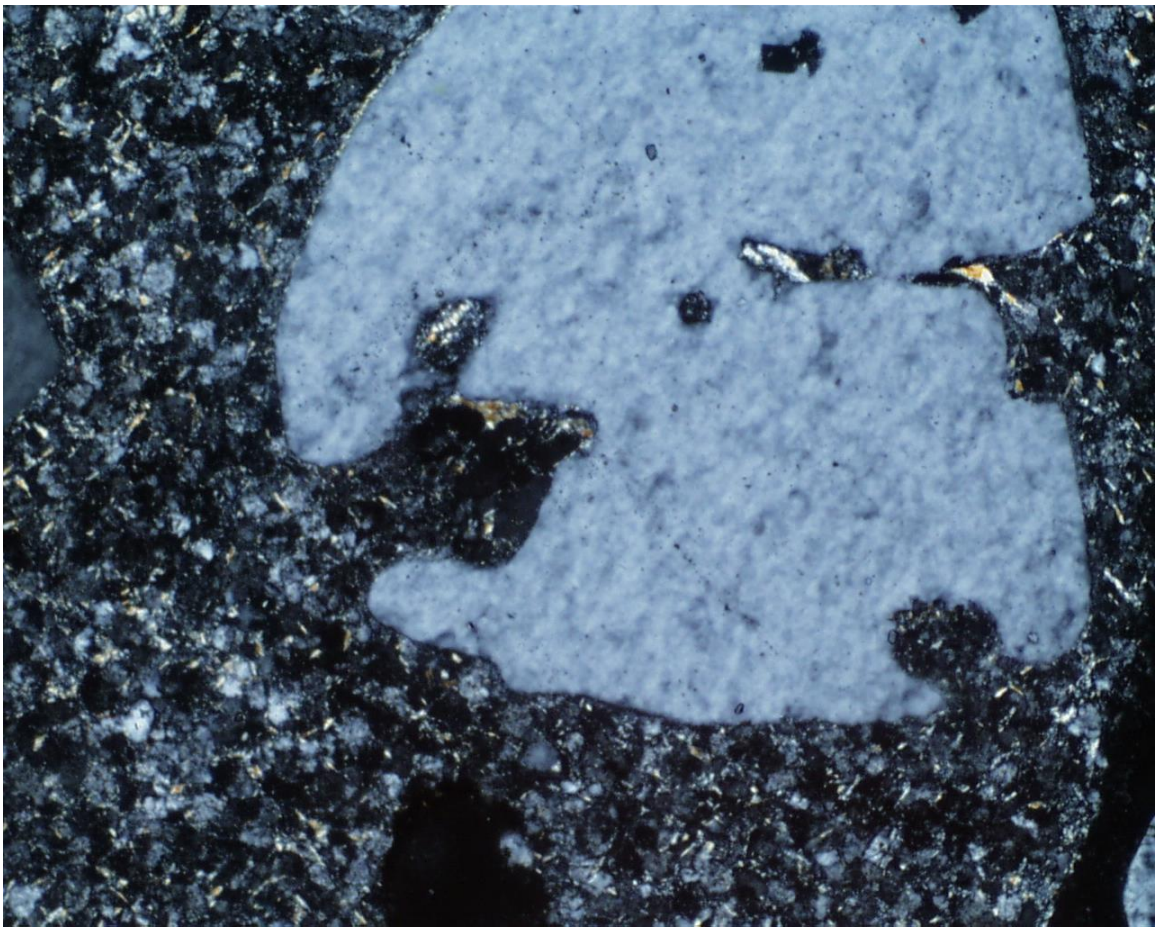

Figure D-9. Partially resorbed quartz grain in rhyolite porphyry intrusion. Resorption of quartz indicates changing temperature and/or pressure conditions in the melt after precipitation of quartz. This resorbed quartz could be related to the silicified breccias found nearby that record venting of volatiles. Cross-polarized light, field of view = 1.7 mm.

SMIg46

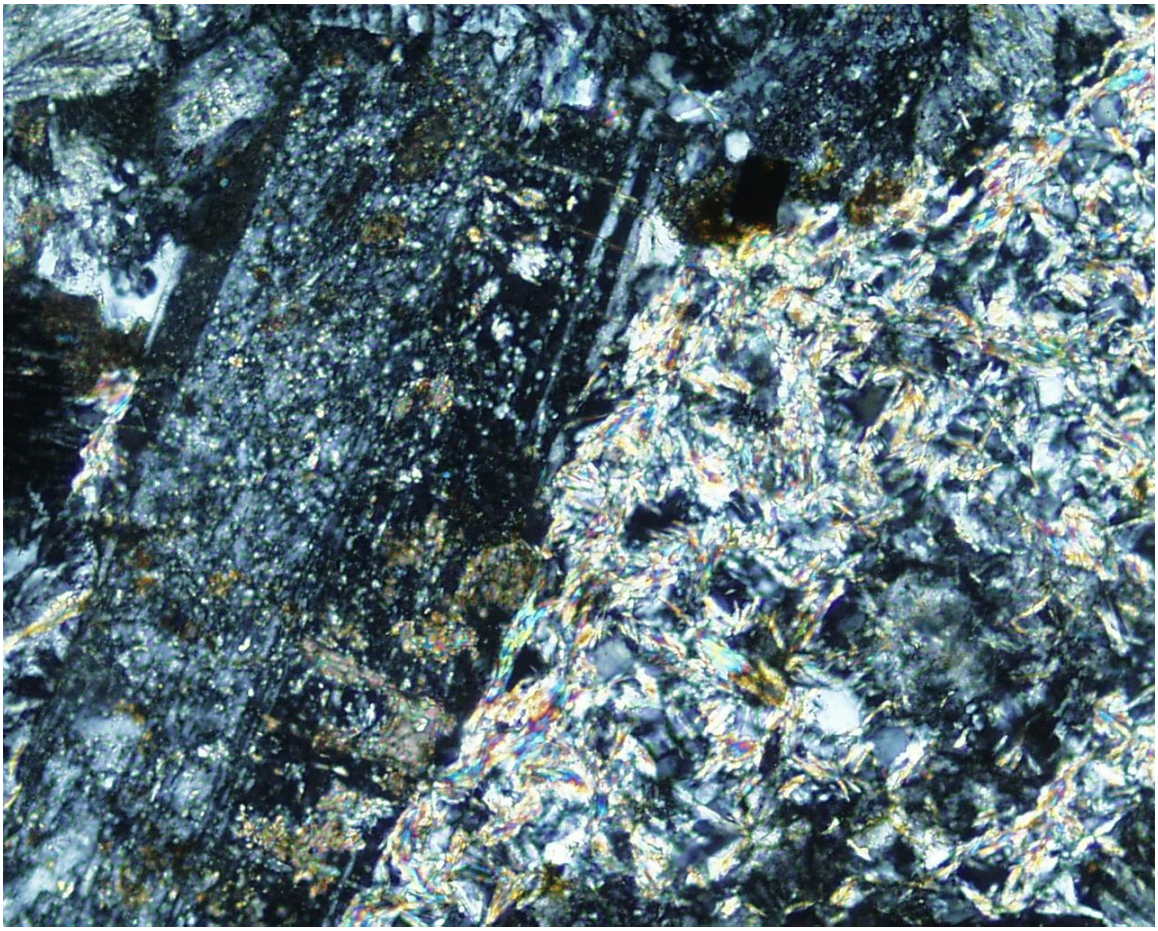

Figure D-10. Medium-grained rhyolite with plagioclase grains altered by sericite and calcite. Cross-polarized light, field of view = 0.85 mm.

SMIg47

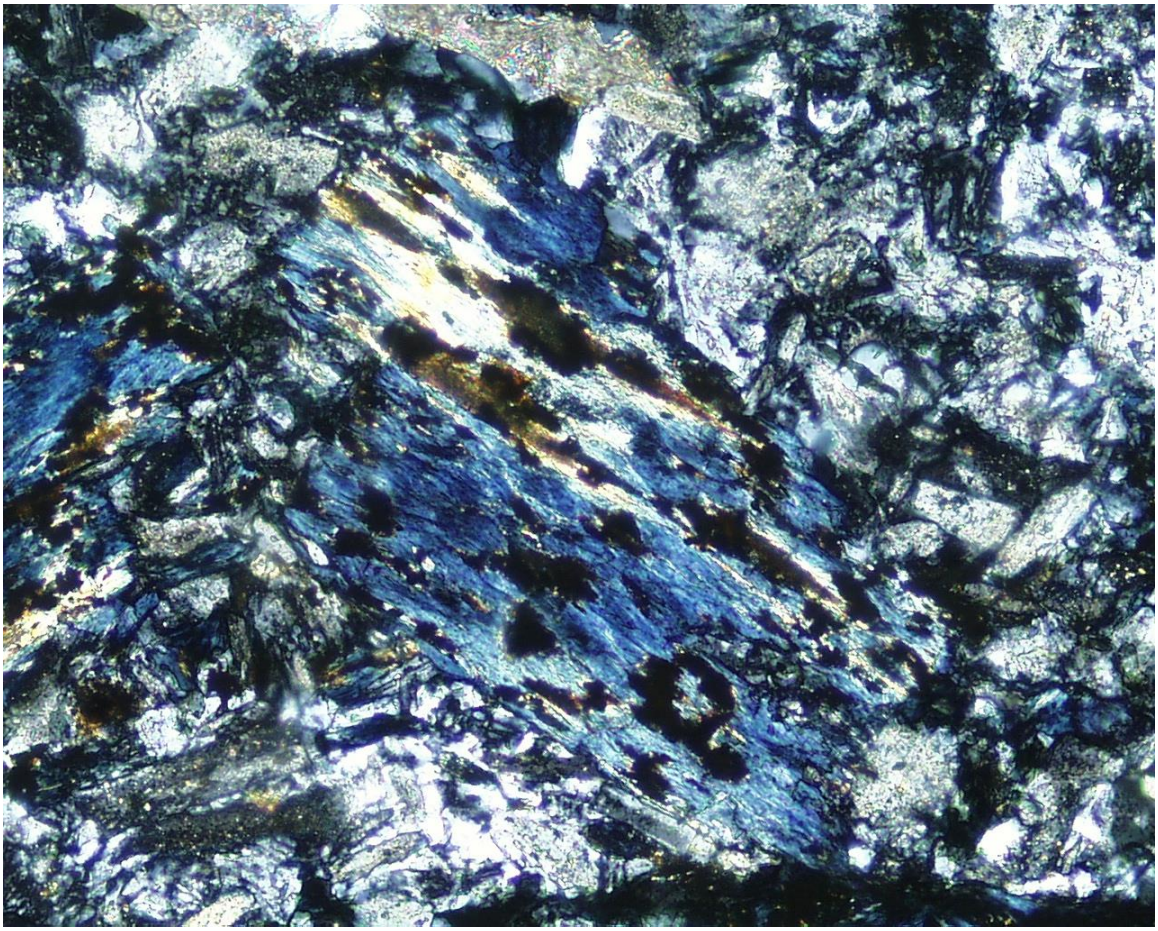

Figure D-11. Chlorite replacing biotite phenocryst in dacite porphyry. Cross-polarized light, field of view = 0.85 mm.

Figure D-12. Plagioclase phenocryst with weak calcite replacement. Cross-polarized light, field of view = 1.7 mm.

SMIg48

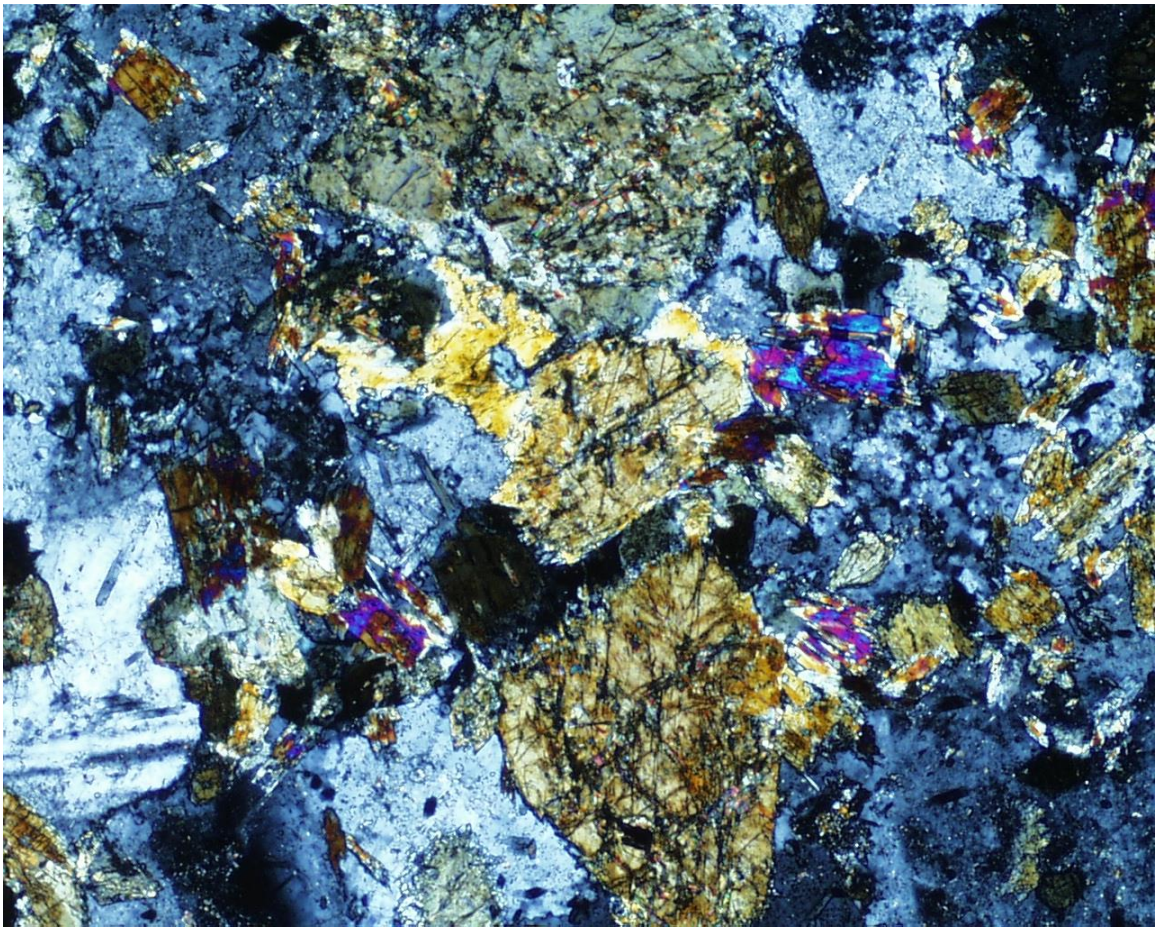

Figure D-13. Fine grained andesite dike composed of plagioclase and amphibole grains. Alteration effects are minimal. Cross-polarized light, field of view = 1.7 mm.

SMIg49

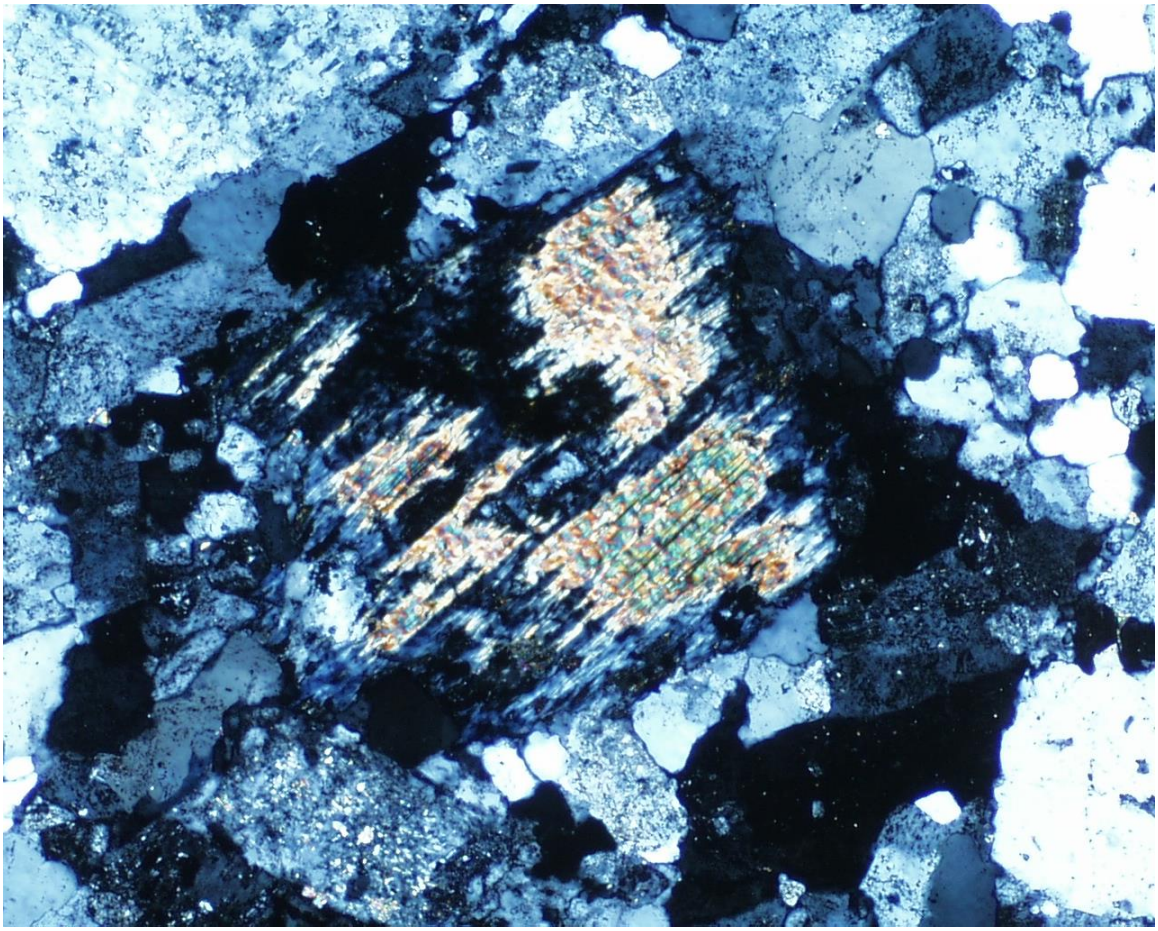

Figure D-14. Biotite phenocryst in granite porphyry with chlorite alteration. Cross-polarized light, field of view = 1.7 mm.

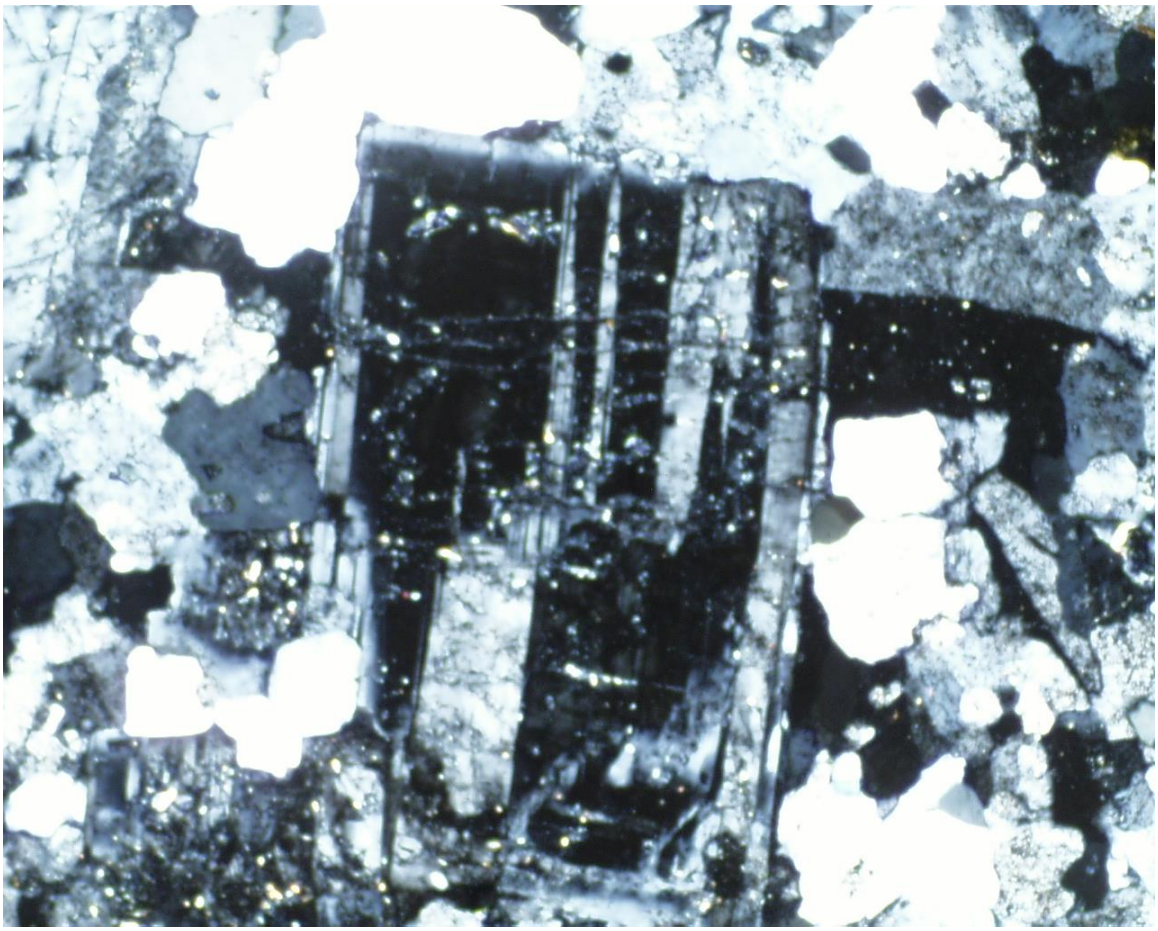

Figure D-15. Plagioclase phenocryst in matrix of quartz and feldspar. Plagioclase composition is oligoclase. Cross-polarized light, field of view = 1.7 mm.

Figure D-16. Disseminated pyrite grain showing replacement by chalcopyrite. Reflected light, field of view = 0.85 mm.

SMIg50

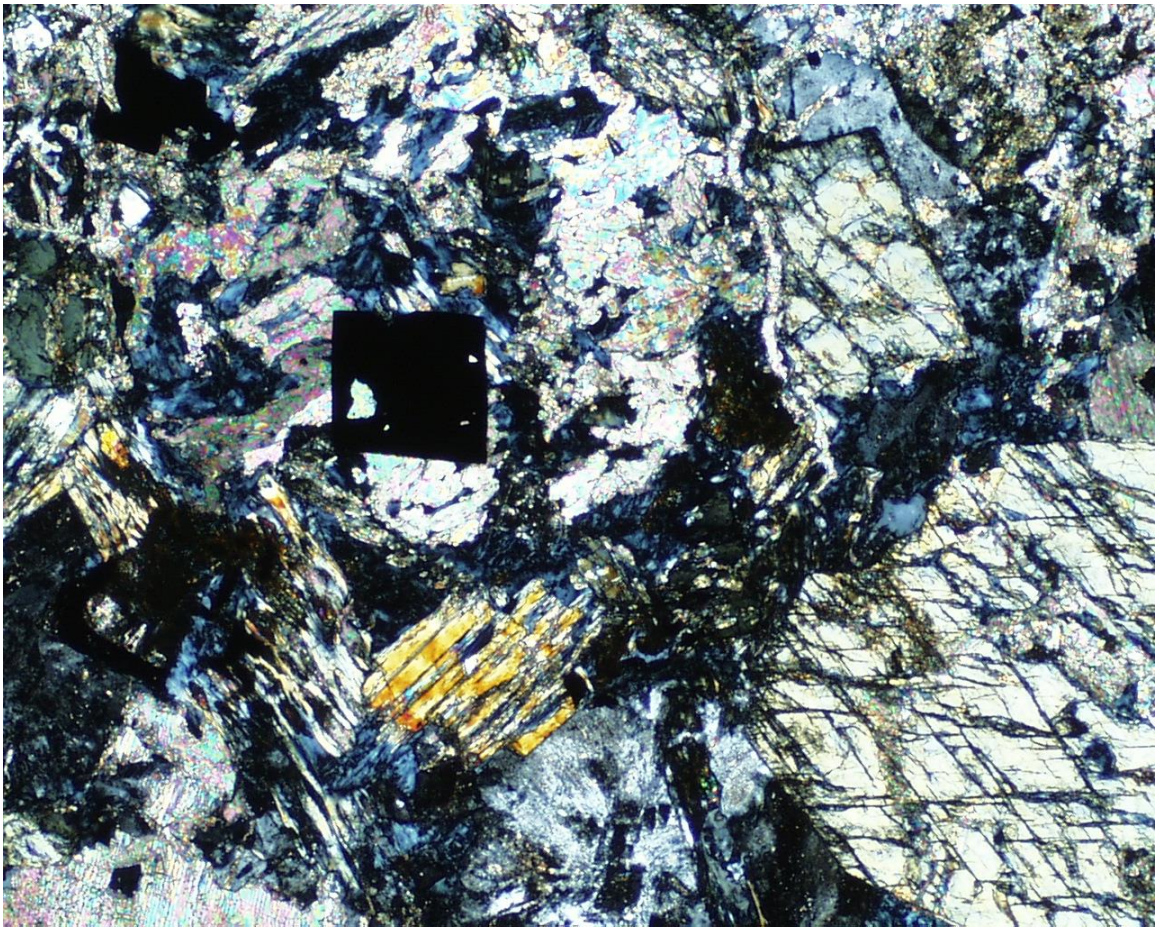

Figure D-17. Medium-grained trachyandesite dike composed of amphibole and plagioclase. Moderate alteration with chlorite, calcite, and pyrite replacing primary minerals. Cross-polarized light, field of view = 1.7 mm.

SMIg51

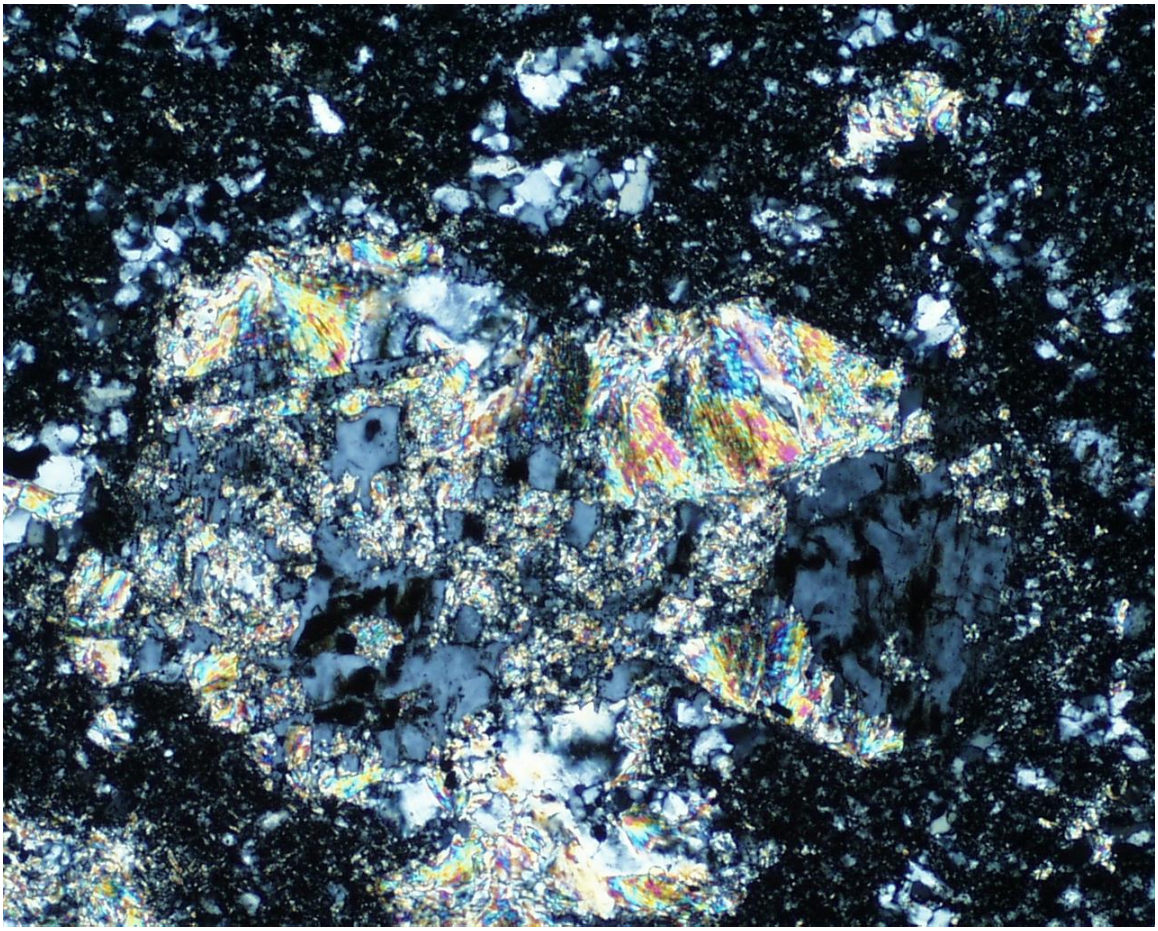

Figure D-18. Potassium feldspar grain with partial replacement by sericite in rhyolite porphyry. Groundmass is fine-grained quartz and feldspars. Cross-polarized light, field of view = 1.7 mm.

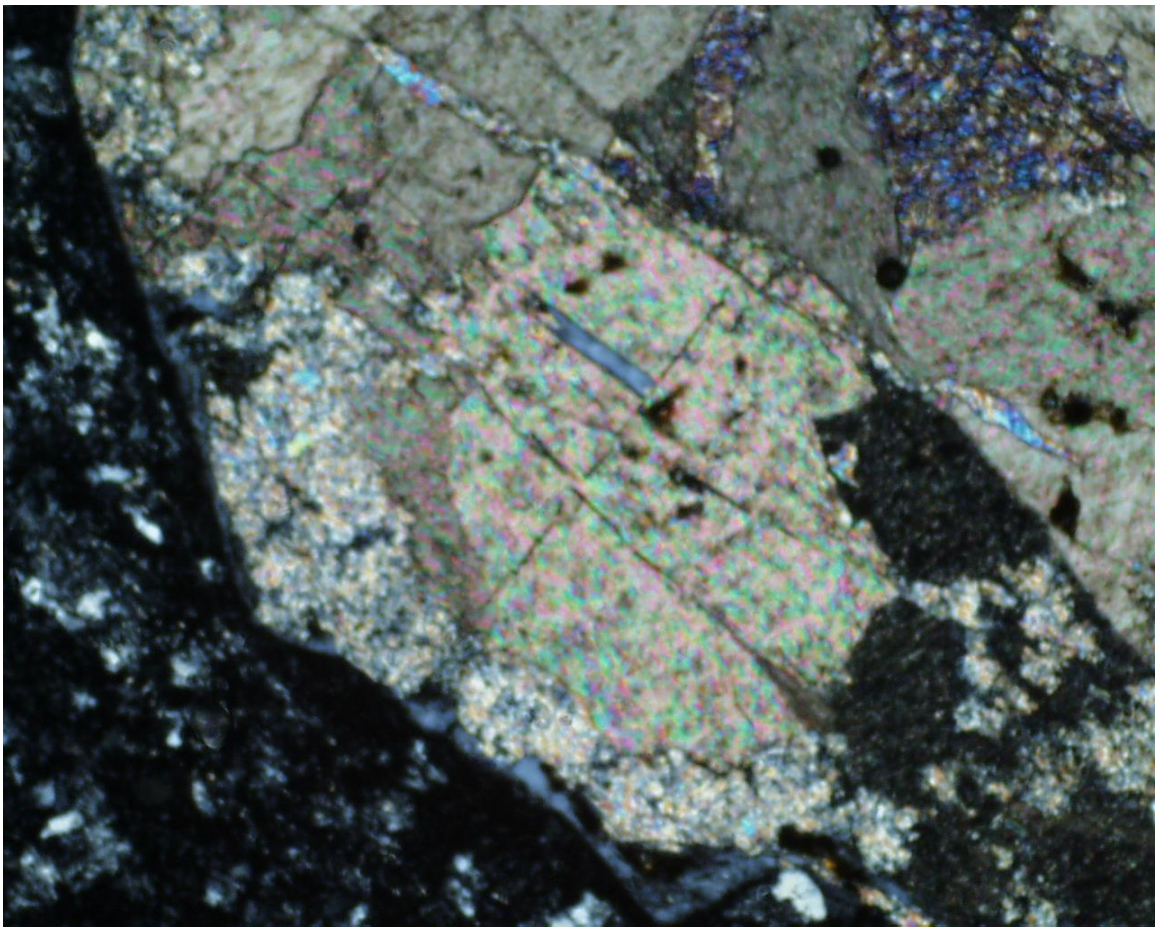

Figure D-19. Complete replacement of feldspar by calcite. Cross-polarized light, field of view = 1.7 mm.

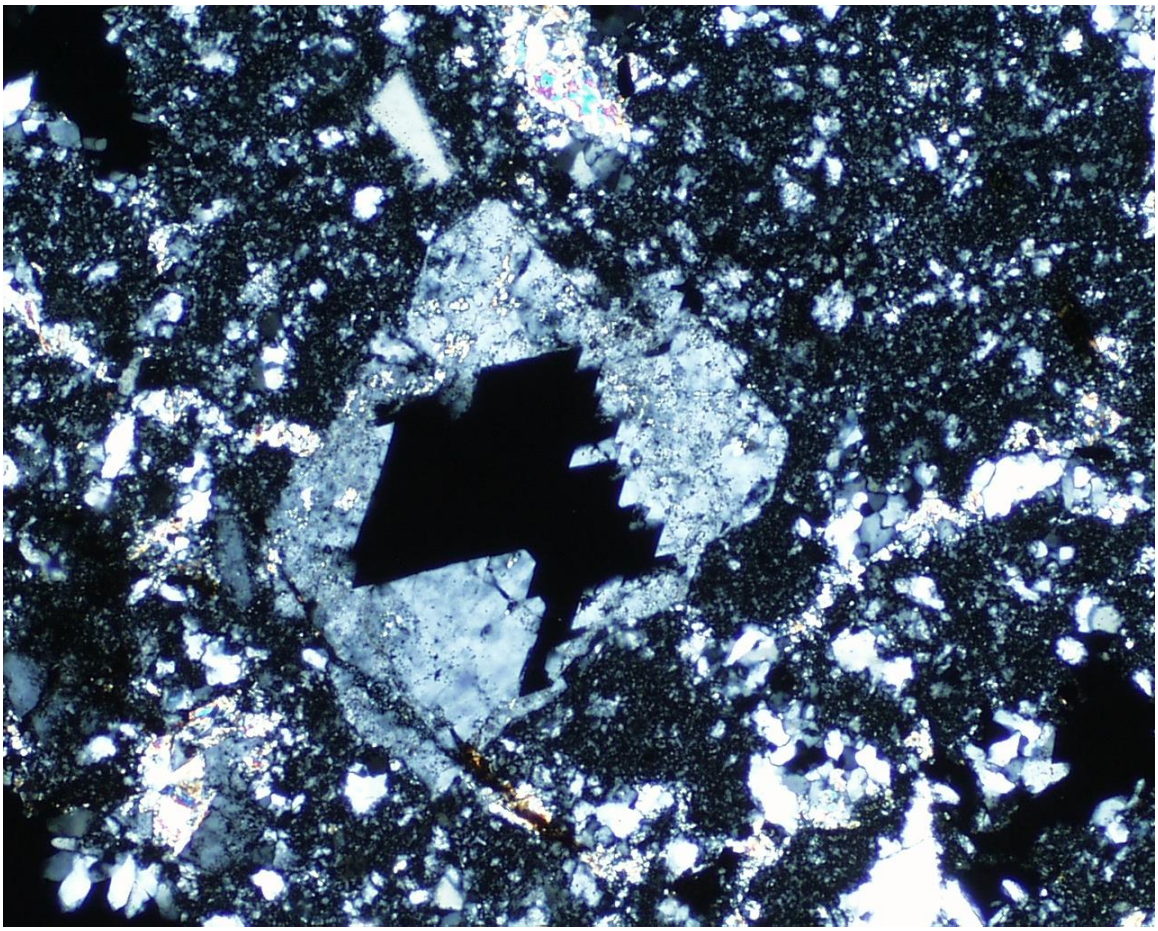

Figure D-20. Feldspar grain replaced by fluorite. Cross-polarized light, field of view = 1.7 mm.